WASM: Minerals, Energy and Chemical Engineering

ESTIMATION OF FORMATION ROCK WETTABILITY FROM ELASTIC WAVE MEASUREMENT

Xuekai Li
(Jimmy)
0000-0002-5825-0673

This thesis is presented for the Degree of

Doctor of Philosophy

of

Curtin University

September 2021

Declaration

To the best of my knowledge and belief, this thesis contains no material previously published by any other person, except where due acknowledgment has been made.

This thesis contains no material which has been accepted for the award of any other degrees or diplomas in any university.

Signature: Xuekai Li

Date: 19 May 2021

Abstract

Wettability is the ability of a liquid to maintain contact with a solid surface, and it is controlled by the balance between the intermolecular interactions of the adhesive type (liquid to the surface) and cohesive type (liquid to liquid). As an interfacial phenomenon, wettability has been identified as one of the most critical factors that affect reservoir performance. Conventionally, the wettability is determined on rock core samples by measuring contact angle, imbibition (Amott method), or capillary pressure against saturation during centrifugal imbibition and drainage (USBM method). However, these methods can only provide the wettability of the core sample rather than in-situ formation wettability. Therefore, some limited indirect methods to estimate the in-situ wettability, such as using NMR and electrical logging data, have been developed. The use of elastic wave, which is sensitive to the elastic properties of the media, has been widely applied in geophysical exploration and oil field development. Previous studies have demonstrated that the lithology, type of pore fluids, and petrophysical parameters, such as porosity and permeability, significantly influence elastic wave dispersion and attenuation. However, the effect of wettability on the elastic wave has been little studied.

The porous and permeable sedimentary rock provides space for geo-fluid (water and hydrocarbon) accumulation in the underground reservoirs. The vast interface area of the pore network and its wettability properties have enormous impacts on the fluid-flow hydrodynamics and spatial distribution of the pore-filling fluids, in which the slip boundary condition (SBC) prevails. In this thesis, the wettability effect on wave propagation is characterized as slippage in the wave-induced-fluid-flow (WIFF), where two different models (virtually enlarged model and apparent slip model) are created to bring the slip length as a wettability indicator to study the wettability effect on the wave propagation in the fluid-saturated porous media. The results show that increasing hydrophobicity yields a higher phase velocity and attenuation peak in the intermediate to high-frequency range. Significantly, the velocity predicted by the theoretical models in the hydrophobic porous media saturated by the non-wetting fluid is more sensitive to the frequency change than the case of hydrophilic porous media. Based on the discovery of the wettability effect on wave propagation, I achieve the primary objective of this research and develop a practical method to estimate the wettability by measuring the dispersion of the wave velocities, which has been validated by experimental tests.

In addition, the dynamic permeability, wave velocities, and attenuation are studied by incorporating the vorticity diffusion (slow S-wave) and slip boundary condition into the pore-

scale oscillatory forced flow model concerning the broadband pore size distribution. In the pore size distribution plot, there are often several peaks recognized as the characteristic pore sizes, which correspond to the sub-characteristic frequencies in the dynamic permeability. The wettability effect has also been studied experimentally in granular porous media, where the results can be interpreted by the wettability-dependent fluid spatial distribution. Only if the pore-filling fluid (e.g. water) wets to the solid grains or pore walls can it occupy the relatively small size pore such as grain contacts or cracks. The wetting fluid inside the small pores increases the stiffness of the media and enlarges the characteristic length of the force chains, therefore the wave velocities and scattering are influenced by the wettability.

Acknowledgments

It has been an exciting but challenging journey to pursue a Ph.D. degree after leaving school and working in the industry for ten years. I appreciate the unique experience, thank many people for their help, support, and encourage me to complete the research tasks.

I want to express my most sincere gratefulness to my supervisor Prof. Reza Rezaee. Thank you for guiding me into the mysterious scientific world by providing me with precious research opportunities and supporting every step of the research work at Curtin University. I appreciate the philosophies, the independence, and the trust you provided me throughout the journey of knowledge exploration. I cherish the analytical and critical thinking developed under your guidance that constitutes who I would like to be as an independent scientific explorer from the long-term perspective. I also want to thank my co-supervisor, Geophysicist Dr. Tobias Müller for the guidance and generous sharing of knowledge of wave propagation and rock physics theory and the method and attitude of rigorous scholarship research. I express great appreciation to my co-supervisor, the senior lecturer Dr. Mohammad Sarmadivaleh for the enormous support and discussion on the execution of experiments in the Geomechanics laboratory. I extend many thanks to the support I have received from the friends and fellows in the discipline of Petroleum Engineering, Western Australian School of Mines (WASM) at Curtin University.

Special thanks to my friends from Unconventional Gas Research Group (UGRG): Dr. Hongcai Wang, Dr. Jie Zou, Dr. Yujie Yuan, Dr. Nadia Testamanti, Dr. Hongyan Yu, Dr. Pooya Hadian, Dr. Lukman Johnson, and Dr. Jamiu Ekundayo. Thank you, Hongcai, for your supports, encouragement, and the introduction of the Petroleum Engineering Department of Curtin University. I thank Jie for the friendship and encouragement on the research. I appreciate Yujie, Nadia and Hongyan, for the training of NMR equipment in the UGRG lab. Thank you for giving me the patient trainings on the NMR facility and supporting me with inspiring suggestions and discussions. Thanks to Pooya for the training on using the lab injection pumps. I thank Lukman and Jamiu for discussing data science and application on the subsequent Ph.D. research topics. Gratitude also goes to my current fellows from our Petroleum Engineering discipline: Runhua Feng, Zhiqi Zhong (Justin), Lingping Zeng, Liming Qin (Leon), Faaiz Al-Shajalee, Gonzalo Ceron Lopez, Partha Pratim Mandal, and Miftah Hidayat, for spending your time to help me in the lab time to time, discussing and sharing your research knowledge and experience. Thanks to Dr. Nilesh Kumar Jha and Dr. Cut Aja Fauziah for using the IFT and

contact angle measurement. I thank the technical lab officers Mr. Robert Webb (Bob), Dr. Nathan Tarom, and Dr. Mohsen Ghasemiziarani, for their laboratory support and the sharing of lab safety knowledge. Special gratitude goes to Dr. Eghan Arjomand and Dr. Nasser Saleh 'Amur Al Maskari to share their experience and knowledge of writing the thesis.

Much gratitude goes to Associate Prof. Mofazzal Hossain; thank you for supporting me in my scholarship application and sharing your valuable life philosophies. Thank you, Dr. Christopher Lagat, for supporting the SEM training. Thank you, Associate Prof. Ali Saeedi and Senior Lecturer Dr. Sam Xie, for sharing the helpful scientific writing books and your experiences in teaching and research.

I also want to thank the researchers in CSIRO, Mr. Michael Verrall for generous discussion and providing the furnace to build the synthetic core sample, Dr. Matt Josh for great introduction of the combined acoustic and dielectric measurement facility, Dr. Lionel Esteban for the training of Oxford NMR instrument, Dr. Claudio Delle Piane for the discussion of the research method of rock physics. Special thanks for the discussion of my research topic with the researchers in the Exploration Geophysics department. To Prof. Boris Gurevich, thank you for the insightful talks and advice regarding the wave propagation models. Thanks to Prof. Maxim Lebedev for the discussion of experimental methods of ultrasonic measurement on the geological specimen.

I also extend my acknowledge to the other friends who work and study in the Australian Resources Research Centre (ARRC) facility for sharing the wonderful time during my Ph.D. study in no particular order: Emad Al-Khdheeawi, Duraid Al-Bayati, Xingguang Xu (CSIRO), Shuo Liu, Hongyi Sun, Jiang, Jia, Pei Li, Yadong Zhang, Yihuai Zhang, Yongqiang Chen, Ruby Lo, Zheng Law, Surudee Bunpitakgate, Nichole Sik, Moustafa Elzeftawy, Faranak Parvinpour, Junfang Zhang (CSIRO), Yunfeng Chen (CSIRO), Yunqing Chen (CSIRO), Si-Yu Hu (CSIRO), Matt Mayes (CSIRO), Tolu Olu-Ojo, Omar Al-Fatlawi, Dhifaf Sadeq, Reza Rudd, Mohammad Almobarak, Kumar Roy, Ahmed Sari, Yuan Mei (CSIRO), Peng Guo (CSIRO), Tsing Bohu (CSIRO), Yongyang Sun, Chris Qin, Rupeng Ma, Wenhui Tan, Jiabin Liang, Bo-Ye Fu, Nazanin Nourifard, Abdurahim Ali F Elkaseh.

Much gratitude is expressed to the groups and organizations providing financial supports, facility assistance, and tested samples. Thanks to the Unconventional Gas Research Group (UGRG), the discipline of Petroleum Engineering in Western Australian School of Mines (WASM) at Curtin University, the Commonwealth Scientific and Industrial Research

Organisation (CSIRO) for their facility assistances, and the IMCD Australia Limited for their Quilon-C chemical sponsorship. Special and sincere acknowledgments to Australia Government Research Training Program (RTP) Stipend Scholarship for their financial support to the whole project.

Nothing could express how most profound appreciation and gratefulness I hold to my family for your consistent support and encouragement during the journey of Ph.D. study. I am deeply grateful to my mum and dad for always encouraging me to pursue my educational endeavors. There are no words to convey how truly grateful I am to my wife, Emily Liu, for your love and support. This work would not have been possible without you. My great thanks to my son Leo Li. I am always amazed and inspired by your out-of-box ideas and beautiful drawings. I always wonder, isn't it the thinking outside the square that a true researcher should have to create the new science and build a better world?!

Table of Contents

Declaration 1

Abstract 2

Acknowledgments 4

List of Figures 10

List of Tables 14

Chapter 1. Introduction 15

1.1. Overview of the Research 15

1.2. Objectives 17

1.3. Thesis Structure 17

1.4. Publication Outlines 20

Chapter 2. Literature Review – Wettability Measurement and Wave Propagation in Porous Media 22

2.1. Method of Wettability Measurement 22

2.1.1. Laboratory Method of Wettability Measurement 22

2.1.2. Well Logging Approaches to Probe the Reservoir Wettability 25

2.2. Theory of Wave Propagation in Saturated Porous Medium 27

2.2.1. Gassmann Equations of the Application in the Multiple Fluids Saturated Rock 28

2.2.2. Biot Theory of Poroelasticity 33

2.2.3. Squirt Flow Models 38

2.2.4. Mesoscopic Flow Models 42

Chapter 3. Wettability Effect on Wave Propagation in Saturated Porous Medium 45

3.1. Introduction 45

3.2. Virtually Enlarged Pore (VEP) Model 48

3.2.1. The Velocity of the Oscillatory Forced Flow with Slip BC 48

3.2.2. Viscosity Correction Factor in VEP Model 51

3.3. Dynamic Permeability and Tortuosity of the VEP Model 52

3.3.1. Relationship Between the Viscosity Correction Factor and the Dynamic Permeability and Tortuosity 52

3.3.2. Properties of the Dynamic Permeability and Tortuosity in the VEP Model 53

3.4. Implementation of VEP Model 55

3.4.1. Phase Velocities and Attenuation 56

3.4.2. Amplitude Ratio and Phase Difference of Fluid and Solid Phases 57

3.5. Discussion 61

3.6. Conclusion 62

Chapter 4. Elastic Waves in Porous Media Saturated with Non-wetting Fluid 63

4.1. Introduction 63
4.2. Theory of Apparent Slippage and Effective Viscosity 66
4.3. Apparent Slip Effect on Dynamic Permeability and Tortuosity 69
4.4. Phase Velocity and Attenuation 73
4.5. Discussion 78
4.6. Conclusion 79
Chapter 5. Pore Size Distribution Controls Dynamic Permeability 80
5.1. Introduction 80
5.2. Theory 81
5.3.1. Hydrodynamics of Oscillating Flow at Pore-scale 81
5.3.2. Interaction of Propagating and Diffusive Waves at Macro-Scale 82
5.3.3. Dynamic Permeability Based on Pore Size Distribution 83
5.3.4. Dynamic Permeability for Different Wettability Conditions 84
5.3. Implications 85
5.3.1. Dynamic Permeability for Bimodal PSD 85
5.3.2. Dynamic Permeability for Measured PSD 87
5.3.3. Characteristic Frequencies 88
5.4. Discussion and Conclusions 89
Chapter 6. Vorticity Dissipation and Slip Boundary Condition on Biot Mechanism in the Porous Media with Broadband Pore Size Distribution 91
6.1. Introduction 91
6.2. Pore-scale Vorticity Diffusion in Porous Media 94
6.2.1. Vorticity Diffusion and the Frictional Dissipation 94
6.2.2. The Critical Frequency and The Critical Pore Size 96
6.2.3. Numerical Examples of The Pore-scale Vorticity and Flow Velocity Field 97
6.3. Effective Viscosity for the Porous Media with Broadband Pore Size Distribution and Slip Boundary Condition 101
6.3.1. Viscosity Correction Based on Pore Size Distribution Data 101
6.3.2. Effective Viscosity with Slip Boundary Condition 103
6.4. The Solution of Velocity Dispersion and Attenuation in the Porous Media 104
6.5. Results and Application 105
6.5.1. Pore Size Distribution Data 105
6.5.2. Wave Attenuation and Velocity Dispersion 106
6.5.3. Experimental Validation of Natural Sedimentary Rock 109
6.6. Discussion 111
6.7. Conclusion 113

Chapter 7. Wettability-dependent Wave Velocities and1Attenuation in Granular Porous Media 114
7.1. Introduction 115
7.2. Experimental Setup 117
7.3. Experimental Results 120
7.3.1. Water-wetting Case 120
7.3.2. Gas-wetting Case 120
7.4. Wettability Impact on the Velocity and Attenuation 121
7.5.1. Water-wetting case 122
7.5.2. Gas-wetting case 126
7.5.3. The Role of Wettability in P-wave Transmission 127
7.5. Discussion 128
7.5.1. Path Effect on the Acoustics of Porous Granular Media 128
7.5.2. Effect of Micro-slip Between Grains 129
7.5.3. Comparison with Literature 130
7.6. Conclusion 131
Chapter 8. Conclusions and Outlook for Future Research 132
8.1. Conclusions 132
8.2. Outlook for Future Research 133
Appendix A Plane Wave Solution 135
Appendix B Gassmann-Wood and Gassmann-Hill Limits for Partially Saturated Sample 136
Appendix C Attenuation Estimation by Spectral-Ratio Method 138
Appendix D Copy Right Consent 140
Appendix E: Attribution of Authorship 143
Reference 147

List of Figures

Figure 2. 1 Wettability system of water, oil, and rock system (Raza et al., 1968).....23
Figure 2. 2 Capillary pressure curves for oil-water displacement in the rock core sample (Anderson, 1986d).....25
Figure 2. 3 Multiple scale heterogeneity related to the elastic wave attenuation (Müller et al., 2010).....28
Figure 2. 4 The BISQ model. (a) Biot flow and squirt flow in a rock due to seismic excitation; (b) A cylindrical representative volume of a rock.....39
Figure 2. 5 Sketch of the model configuration (Murphy III et al., 1986). Soft pore forms a disc-shaped gap between two grains, and its edge opens into a toroidal stiff pore.....41
Figure 2. 6 The inclusion and patch geometry in the White model for partially saturated rock.....43

Figure 3. 1 The slip boundary condition (BC) with slip length b for oscillatory forced flow in a duct pore with radius r = a. The tangential velocity profile vanishes at the wall of a virtually enlarged pore (VEP) with radius r = a + b.....45
Figure 3. 2 The dimensionless slip length increases significantly during the transition of the flow surface from hydrophilic $\theta_c < 90°$ to hydrophobic $\theta_c > 90°$.....47
Figure 3. 3 Normalized velocity profile of flow in a capillary duct pore with 10 μm radius in VEP model at a frequency range of: (a) 1k Hz – 3M Hz, and (b)100k Hz.....50
Figure 3. 4 The ratio of the average velocities and ratio of the friction force (real part) for VEP model and HF Biot model in the frequency domain for a 10 μm duct pore saturated by water.....52
Figure 3. 5 Comparison of dynamic permeability (a) and tortuosity (b) (real parts) of HF Biot and VEP (b = a/20) models for a porous medium with 10 μm average pore radius.....54
Figure 3. 6 Fast P wave phase velocity (a) and attenuation (b), and Slow P wave phase velocity (c) and attenuation (d) under different wettability conditions. The arrow indicates the Biot characteristic frequency $fc = \omega B 2\pi$.....57
Figure 3. 7 Amplitude ratio of fluid and solid phases under different wettability conditions for (a) fast P wave, (b) slow P wave in the frequency domain. The arrow indicates the Biot characteristic frequency $fc = \omega B 2\pi$.....59
Figure 3. 8 Phase difference between fluid and solid phases under different wettability conditions for (a) fast P wave, and (b) slow P wave frequency domain. The arrow indicates the Biot characteristic frequency $fc = \omega B 2\pi$.....60

Figure 4. 1 (a) No-slip BC; (b) slip BC with slip velocity vs and slip length b in a virtually enlarged pore wall; (c) slip BC with slip length b and smaller apparent viscosity $\mu fslip$ inside the viscous skin depth δ than the viscosity of the bulk fluid μf.....64
Figure 4. 2 The molecular density distribution in a nanochannel by MD simulation. Courtesy of Cao et al. (2006).....65
Figure 4. 3 The normalised effective viscosity under different slip lengths for brine in frequency spectral. Three slip lengths are a fraction of a typical pore size of sandstone r = 10 μm. Parameters in Table 4.1 are used.....67
Figure 4. 4 Normalised effective viscosity of four different fluids in frequency spectral. The slip length b = 0.1r is a fraction of a typical pore size of sandstone r = 10 μm. Parameters in Table 4.1 are used.....67
Figure 4. 5 The dynamic permeability normalised by the static permeability for tube-shape and slab-shape pores saturated by brine under various slip conditions.....71

Figure 4. 6 The phase of the dynamic permeability for tube-shape and slab shape pores saturated by brine under various slip conditions. 71
Figure 4. 7 The dynamic tortuosity normalised by the static tortuosity for tube shape and slab shape pores saturated by brine under various slip conditions. 72
Figure 4. 8 The fast P-wave velocity of fully saturated sandstone. Four types of fluids are used: (a) oil, (b) brine, (c) light oil and (d) supercritical CO2. Parameters in Table 4. 1are used. 75
Figure 4. 9 The slow P-wave velocity of fully saturated sandstone. Four types of fluids are used: (a) oil, (b) brine, (c) light oil and (d) supercriticalCO2. Parameters in Table 4.1 are used. 76
Figure 4. 10 The attenuation (fast P wave) of fully saturated sandstone. Four types of fluids are used: (a) oil, (b) brine, (c) light oil and (d) supercritical CO2. Parameters in Table 4.1 are used. 77
Figure 4. 11 The attenuation (slow P wave) of fully saturated sandstone. Four types of fluids are used: (a) oil, (b) brine, (c) light oil and (d) supercritical CO2. Parameters in Table 4.1 are used. 78

Figure 5. 1 (a) Accumulative and (b) incremental porosity of two bimodal pore size distributions; (c) real and (d) imaginary part of the dynamic permeability and approximation in the slip boundary (hydrophobic) condition. The horizontal dash lines indicate the zero values. The vertical dotted line marks the Biot frequency $fB = \omega B/2\pi$. 86
Figure 5. 2 The pore sizes and the distribution of (a) accumulative and (b) incremental porosity for Bentheimer sandstone obtained from NMR T2 data (53 measurement points) calibrated by the pore throat radii distribution of MICP; SEM image in the insets demonstrates the Bentheimer sandstone has well-sorted grain framework but complicated pore network structure (light red shading in (b)). A comparison of the (c) real parts and (d) imaginary parts of the dynamic permeability normalized by dc permeability for the Bentheimer sandstone by three different pore shape models. The Biot frequency fB is marked by the red dashed line. The characteristic frequencies $fc1$, $fc2$, $fc3$ are associated with the characteristic pore sizes. MICP, mercury injection capillary pressure; NMR, nuclear magnetic resonance; SEM, scanning electron microscopy. 87
Figure 5. 3 Imaginary part of the length scale $Li\omega; r = r\phi iv$ as a function of frequency and pore size where the solid black line ($\lambda \approx 4r$) based on Equation (5.12) corresponds to the pore-scale dissipation peaks and the high- frequency linear asymptotic approximation based on Equation (5.13) is plotted as a dashed line. 89

Figure 6. 1 (a) Schematic of the vortices in porous medium induced by the elastic waves; (b) vorticity direction determined by the right-hand rule. 92
Figure 6. 2 Schematics of the profiles of the viscous fluid velocity v and the corresponding vorticity Ω. 93
Figure 6. 3 Real part and (b) imaginary part of the normalized magnitude of interface vortices $\Omega i\omega, r$ are function of frequency and pore size, which are plotted at log-log scale. The pore-scale critical frequency fc defined by Equation (6.17) is plotted as a white solid line and its linear asymptotic value defined by Equation (6.18) are plotted as a white dash line. The Biot frequency $fB = \omega B/2\pi$. and the critical pore radius rB defined by Equation (6.19) are plotted in red and black dash lines, respectively. 98
Figure 6. 4 The pore-scale profiles of normalized **v** in (a) cylindrical tube and (b) porous medium; and pore-scale profiles of the corresponding normalized $\Omega\delta$ in (c) cylindrical tube and (d) porous medium at frequency domain. The viscous skin depths are marked as black dashed lines. The crossover frequency $fB = \omega B/2\pi$ are marked as white dashed lines. The pore radius $r = \delta p0$. 99
Figure 6. 5 (a) the pore-scale profiles of normalized v in a porous medium at 6 different frequencies and (b) the corresponding 3D plot; (c) the pore-scale profiles of normalized $\Omega\delta$ in porous medium at 6

different frequencies and (d) the corresponding 3D plot; The viscous skin depths are marked as light red shadings. The pore radius $r = \delta p0$. 100
Figure 6. 6 The pore-scale profiles of normalized v in (a) cylindrical tube and (b) porous medium; and pore-scale profiles of the corresponding normalized $\Omega\delta$ in (c) cylindrical tube and (d) porous medium at frequency domain. The viscous skin depths are marked as black dashed lines. The crossover frequency $fB = \omega B/2\pi$ are marked as white dashed lines. The pore radius $r = 5\kappa 0\phi$... 100
Figure 6. 7 (a) the pore-scale profiles of normalized v in sandstone at 6 different frequencies and (b) the corresponding 3D plot; (c) the pore-scale profiles of normalized $\Omega\delta$ in porous medium at 6 different frequencies and (b) the corresponding 3D plot; The pore radius $r = 5\kappa 0\phi$ 101
Figure 6. 8 (a) Cumulative porosity and (b) incremental porosity. 105
Figure 6. 9 The effective viscosity in the porous media with two kinds of pore size distributions (PSD) and different slip boundary condition. 106
Figure 6. 10 The velocities (V) and the attenuation (1/Q) of P-wave (p+) and S-wave (s-) are compared in the porous medium with different PSD and wettability conditions. 108
Figure 6. 11 The velocities and the attenuation (1/Q) of slow P-wave (p-) in the porous medium with different PSD and wettability conditions. 108
Figure 6. 12 The velocity dispersion is an indicator of different slip boundary conditions (wettability). The hydrophobicity promotes a higher dispersion than it in the hydrophilic condition. 109
Figure 6. 13 The crossplot of the dispersions of compressional wave moduli and shear moduli for (a) Bentheimer sandstone, (b) Berea sandstone and (c) Indiana carbonate. The red and blue data points are from porous media saturated by non-wetting fluid and wetting-fluid, respectively. 111
Figure 6. 14 Comparison of the viscous skin depth in the infinite long cylindrical tubes (T=1 and 3) and the sandstone (no-slip and slip boundary). The slip length $b = \kappa 0\phi$ is arbitrarily selected for the slip boundary condition. 112
Figure 6. 15 Diffusivity of the vorticity diffusion in the infinite long cylindrical tube $D0$ and the porous medium Dp. 113

Figure 7. 1 (a) Real and (b) schematic experimental set-up for conducting acoustic measurement during the water-air core flooding in the glass bead pack under axial pressure P. T and R denote the piezoelectric transmitter and receiver, respectively. 118
Figure 7. 2 (a) Original glass bead sample (top) appearing in shiny white color and the Quilon-C treated glass bead sample (bottom) in dark green color; (b) microscopy images of the original glass beads and treated beads; (c) the corresponding contact angle of water droplet on the original glass surface (top) is 7.64° and on the processed glass surface after Quilon chemical treatment (bottom) is 105.5°. 119
Figure 7. 3 Recorded waveforms of (a) P-wave and (b) S-wave after incremental injection for water-wetting glass bead packing. The small peak at the t=0 is the cross-talk signal during the pulse generation. 120
Figure 7. 4 Recorded waveforms with incremental water injection for gas-wetting glass bead packing: (a) P-wave; (b) S-wave transmission experiments. 121
Figure 7. 5 The measured velocity-saturation relation in water-wetting glass bead packing is compared with Gassmann-Wood and Gassmann-Hill theoretical predictions for (a) P-Wave and (b) S-Wave. As a reference, Biot theory is used for the calculation of the velocities of the sample under full water saturation. The inset cartoons illustrate the network of force chains (black solid line) in low and fully saturated samples. 122
Figure 7. 6 Velocity-saturation relations in gas-wetting glass bead packing vs Gassmann-Wood and Gassmann-Hill predictions for (a) P-Wave and (b) S-Wave. The last three measurements in high water saturation are obtained after increasing 300% injection pressure P_i. The inset cartoons demonstrate the network of force chain (black solid line) in dry and high to near fully saturated samples. 123

Figure 7. 7 Attenuation-saturation relations of (a) P-wave and (b) S-wave for both water-wetting and gas-wetting samples. 126
Figure 7. 8 (a) The waveforms through the reference sample (aluminium dummy core) and water-wetting sample with 100% water saturation where the time windows of the first period of waveforms are selected (shading highlight) for calculating the amplitude spectrum in each sample; (b) the corresponding spectra by Fourier transform where two peaks are produced in the spectrum of signals in fully saturated water-wetting sample. 126
Figure 7.9 Attenuation-saturation relations of (a) P-wave and (b) S-wave for both water-wetting and gas-wetting samples. 127
Figure 7. 10 (a) Different ray paths are produced during the injection of liquid into the short sample (L=2.8cm). (b) This schematic shows the path effect on the receiving signals with broadband frequencies where the short wavelength (high-frequency) wave tends to follow the fastest ray path. 129
Figure 7.11 Recorded P-waveforms with incremental decane (oil) injection for shorter glassbead packings (L=2.8cm). Two types of signals with different frequencies are recorded in the same wave trains at intermediate saturations (i.e. S_o = 58% and S_o = 64%). 130

List of Tables

Table 3. 1 Parameters of water-saturated sandstone. 55

Table 4. 1 Parameters of sandstone and four different fluids commonly found in the oil reservoir 68

Table 5. 1 Parameters for water-saturated Bentheimer sandstone..... 86

Table 6. 1 Parameters of brine-saturated sandstone. 105

Table 6. 2 Saturation condition in the natural sedimentary rocks with different wettability. 110

Table 7. 1 Parameters of glassbead packing and the injected water..... 123

Chapter 1. Introduction

1.1. Overview of the Research

The wettability refers to the phenomenon that one fluid spread on and adhere to the solid surface in the presence of immiscible other fluid(s). The wettability of reservoir rock has been well studied in the enhancement of oil recovery and reservoir engineering, which is mainly referring to the phenomena associated with water flooding, chemical sweep efficiency, fluid spreading on the solid in the environment of another immiscible fluid, or the capillary effect in the pore network in a porous medium.

The elastic wave as a non-intrusive method is used in sonic well-logging, exploration geophysics, seismology, and rock physics experiments of the oil and gas industry. However, it has not reached its full potential in detecting some of the petrophysical parameters, such as wettability. The wettability and the elastic wave have been individually developing in their regime for a long time. Although some researchers have noticed that the wettability may affect the elastic wave velocity and attenuation (Shakouri et al., 2019; Wang et al., 2015), a thorough study on the mechanism is still insufficient. This research attempts to study the wettability effect on elastic wave measurements. The technique may also be used as a monitor method for dynamic water flooding and wettability alteration processes. Moreover, this study will explore the insight into the mechanism of how wettability influences acoustics measurements, which has not been extensively studied before.

The interested frequency of the elastic wave for most geophysicists is the seismic frequency (10-1000Hz). In contrast, the wettability effect on elastic wave propagation in most fluid-saturated reservoir rocks is only on sonic or ultrasonic frequency (>100kHz) based on this study. Thus, ignoring the impact of the wettability may only raise a minor error on the geophysical interpretations of seismic data such as AVO (Amplitude Variations with Offset) and FWI (Full-Waveform Inversion). A reservoir rock containing the solid matrix frame and the pore-filling fluid is a damper for the elastic wave where most of the attenuation is from the viscous dissipation (Mavko et al., 2009) in which the wettability of the rock plays a role. The elastic wave causes the wave-induced-flow in both micro-scale and macro-scale, wherein the former is known as local flow, and the latter is known as global flow. In some heterogeneous reservoirs (i.e., dual-porosity and dual-permeability), the wave-induced-flow can also occur in the mesoscopic scale (Ba et al., 2011; Pride et al., 2004). In the fluid-saturated porous medium, the

vast pore-fluid interface has an essential impact on the wave-induced-flow in all aspects. So, as long as there is relative movement between the fluids and the solid frame, the hydrodynamics of the pore-filling fluid is under the influence of wettability. The frequency is a crucial factor to determine the extent of the wettability impact by controlling the fluid relaxation and the time of the pressure equilibrium.

The impact of the wettability on the elastic wave in fluid-saturated rock is on two significant aspects. The fluid slippage controlled by wettability may occur on the hydrophobic pore wall during the wave-induced-flow. The slippage is proportional to the degree of hydrophobicity of the solid matrix, marked by the contact angle, Amott index, or USBM index. Meanwhile, the impact of slippage varies on rocks with different inhomogeneous features at micro-scale, such as pore size distribution. Another mechanism is that the fluid locations and spatial distribution determined by wettability can also affect the elastic wave behavior. The wetting fluid always tends to occupy the small pores such as grain contact, slit, aperture, cracks, or a small corner of the irregular shape pore where such pore space recognized as compliant pore has a dominant contribution on the wave dispersion and attenuation through wave-induced-local-flow comparing to the equant pore such as relative bigger size intergranular pore (Mavko and Jizba, 1994). The wave dispersion here refers to the phenomenon that its velocity varies on different frequency ranges. Nevertheless, in such relatively small size pores (often $< 10^8$ m), the wave-induced-flow, if there is any, should still obey the law of Poiseuille flow with no-slip boundary condition (Murphy III et al., 1986). Under the high overburden and confining pressure reservoir condition, the compliant pores are significantly compressed and even closed, the local flow effect may become minimal (Gurevich et al., 2010; Mavko and Jizba, 1994).

Our study finds that the wettability could be identified by two indicators for Bentheimer sandstone and Indiana limestone.

- ✓ The S wave velocity (or shear modulus) of non-wetting fluid saturated rock is higher than that of wetting fluid saturated rock.
- ✓ The P wave velocity dispersion (V_p (high-frequency)- V_p (low-frequency)) of non-wetting fluid saturated rock is higher than that in the wetting fluid saturated rock.

However, there are more fundamental controlling factors for wave dispersion and attenuation over the wettability in reservoir rocks such as the clay content which brings in the viscoelastic effect and distort the wettability effect. For instance, the two indicators fail on Berea sandstones to distinguish their wettability. Moreover, the two indicators are insensitive to complicated

wettability conditions such as fractional wettability wherein the wettability is unevenly distributed inside the porous media.

1.2. Objectives

Understanding the mechanism of the interaction between the wettability and the elastic wave, which is fundamental to develop the engineering technique of probing the reservoir wettability by the elastic wave method. This study serves the goal to explore the feasibility of prediction of the reservoir wettability by the elastic wave, including laboratory experiments and theoretical modeling. The primary objectives of this thesis are:

- Find out the connection between the velocities (including dispersion) and attenuation of P- wave and S- wave in saturated rocks and their wettability in the laboratory measurements.
- Explore the mechanism of micro-fluid slippage in pore-scale under the wave excitation.
- Develop the rock physics model to capture the wettability effect on the wave velocities dispersion and attenuation.
- Provide a feasible methodology to predict the wettability by using the elastic wave measurement.

1.3. Thesis Structure

This thesis includes eight (8) chapters to address the objectives described above. **Chapter 1** gives the introduction of the research project, research objectives, and publication outlines. **Chapter 2** includes the literature review of the relevant research. **Chapter 3** to **Chapter 7** exhibits the theoretical models and experimental results with the corresponding discussion based on published papers. **Chapter 8** concludes and summarises the entire Ph.D. research project.

A summary of **Chapter 3** to **Chapter 7** is provided in the following.

Chapter 3. Wettability Effect on Wave Propagation in Saturated Porous Medium

Chapter 3 investigates the wettability effect on wave propagation in saturated porous media. Micro-fluid mechanics studies have revealed that fluid slip on the boundary of a flow channel is a pretty common phenomenon. In the context of a fluid-saturated porous medium, this

implies that the fluid slippage is proportional to the hydrophobicity, which is the non-wetting degree. Previous studies find that the wettability of the pore surface is strongly related to the slippage, which is characterized by slip length. To accurately predict the elastic properties of a fluid-saturated porous medium for different wettability conditions, the slippage of the wave-induced flow has to be considered. **Chapter 3** introduces the slip length as a proxy for wettability to calculate the viscous correction factor, dynamic permeability, and dynamic tortuosity of Biot theory for elastic waves in a porous medium. It demonstrates that, under different wettability conditions, elastic waves in a saturated porous medium have different phase velocities and attenuations. Specifically, it finds that increasing hydrophobicity yields a higher phase velocity and attenuation peak in a high-frequency range.

Chapter 4. Elastic Waves in Porous Media Saturated with Non-Wetting Fluid

For waves in porous media, it is popular to use Biot theory, which incorporates the wave-induced global flow, accounting for frictional attenuation. The Biot theory assumes that the fluid is wetting to the solid matrix. However, the fluid is not always wetting the rock in real reservoirs. It was previously revealed that a non-wetting fluid parcel tends to slip on the solid wall pore boundary where the intermolecular potential between the fluid and solid wall is weaker than in wetting fluid conditions(Huang et al., 2008). This particular slippage feature means that the coupling relationship between the fluid and solid frame and frictional dissipation is likely to be very different between non-wetting and wetting fluid situations. In **Chapter 4**, this wave-induced slippage is characterized by using an apparent viscosity for the non-wetting fluid within the thin viscous boundary layer. This apparent viscosity is smaller than the viscosity of the bulk fluid. It demonstrates that the slip correction affects the dynamic permeability and dynamic tortuosity and results in slippage/wettability dependent on phase velocities and attenuation of the fully fluid-saturated rock.

Chapter 5. Pore Size Distribution Controls Dynamic Permeability

The dynamic permeability plays a key role in the wave-induced global flow, which is also under the influence of the pore size distribution and wettability. In **Chapter 5**, a dynamic permeability model depending on the pore size distribution and wettability is developed. Existing theoretical models for dynamic permeability assume that the frequency dependence is primarily controlled by a single characteristic length scale of the pore space. However, the fact that in most natural porous media, there exists a distinct range of pore sizes is ignored. To overcome this limitation, a dynamic permeability model is developed that explicitly

incorporates the pore size distribution and wettability effect. It shows that the pore size distribution has a first-order impact on the dynamic permeability. Since the pore size distribution can be deduced from techniques such as nuclear magnetic resonance, our results indicate the possibility to jointly use remote-sensing technologies for improved permeability determination and cross-fertilization of laboratory and in-field techniques.

Chapter 6. Vorticity Dissipation and Slip Boundary Condition on Biot Mechanism in the Porous Media with Broadband Pore Size Distribution

Chapter 6 explores the vorticity dissipation and slip boundary (wettability) effect on the viscous friction flow velocity due to the wave propagation, by which the vorticity diffusion and wettability impact on the Biot Mechanism (wave velocity and attenuation) in the saturated porous media with broadband pore size distribution. The viscous friction is proportional to the interface magnitude of vortices at the pore wall and is affected by the slip boundary condition of the micro-fluid flow, which is related to the wettability of the porous media. The pore size distribution data measured by nuclear magnetic resonance or mercury injection experiments are combined with vorticity diffusion and slip boundary effect to calculate the average friction force and the flow velocity from which an effective viscosity is obtained to account for the combined effect of the vorticity dissipation and the slip boundary. It works similarly to the viscosity correction factor that Biot (1956b) adopts for the high-frequency poroelasticity dynamics but reveals crucial insight on the impact of the vorticity diffusion, slip boundary, and pore size distribution on the wave dispersion and attenuation. The result shows that the vorticity diffusion increases both velocity and attenuation in the high frequencies when the vortices prevail; however, the slip boundary assists counteraction to decrease the attenuation through the friction reduction. The velocity and attention in intermediated frequencies are higher in the rock with more large pores compared to the result of the rock with more small size pores. The model prediction qualitatively agrees with the experimental results in which the dispersions of P- wave and S- wave velocity for non-wetting fluid saturated sandstones are higher than the exact measurements of wetting fluid saturated ones.

Chapter 7. Wettability-dependent Wave Velocities and Attenuation in Granular Porous Media

The presence of more than one fluid phase and different wettability conditions present additional complexities. While it is well known that wave propagation in dry granular porous media is dominated by the presence of force chains (Owens and Daniels, 2011), the influence

of the force chain network in (partially) saturated granular porous media with different wettability conditions remains largely unexplored. In **Chapter 7** the laboratory experiments are designed by combining core flooding and ultrasonic measurement in glass bead packings that were chemically treated to alternate the wettability. The P- and S- wave velocity-saturation-relation and attenuation-saturation-relation are obtained from the waveforms for both water-wetting and gas-wetting cases. The results show that there is a transition from a stable P-wave pulse at low and moderate saturations to a set of incoherently scattered waves at high saturation. The incoherent scattering in the gas-wetting case is negligibly small, whereas it is more pronounced in the water-wetting case. This transition is qualitatively interpreted through a wettability-dependent alteration of the force chains during the injection of the water. It concludes that only if water wets the grains can the liquid enter the grain contacts. These liquid bridges are thought to locally reinforce the force chains and increase their characteristic length scale. This leads to an increase in P-wave velocity and promotes incoherent scattering since the ratio of dominant wavelength to characteristic length scale decreases. In the gas wetting case, however, the presence of gas prevents the water from direct contact with the glass beads and therefore stops the formation and growth of the liquid bridges within the force chain network.

1.4. Publication Outlines

The thesis is hybrid organized based on the outcome of 3 peer-reviewed journal publications, 1 submitted journal paper, and two conference papers listed below, which accordingly correspond to separate chapters. Also, one chapter (Chapter 6) includes non-published content.

Chapter 3.

Li, J. X., Rezaee, R., & Müller, T. M. (2020). Wettability effect on wave propagation in saturated porous medium. The Journal of the Acoustical Society of America, 147(2), 911-920.

Chapter 4.

Li, J. X., Rezaee, R., Müller, T. M., & Sarmadivaleh, M. (2020). Elastic waves in porous media saturated with non-wetting fluid. The APPEA Journal, 60(1), 315-325.

Chapter 5.

Li, J. X., Rezaee, R., Müller, T. M., & Sarmadivaleh, M. (2020). Pore Size Distribution Controls Dynamic Permeability. Geophysical Research Letters, e2020GL090558.

Chapter 7.

Li, J. X., Rezaee, R., Müller, T. M., Madadi, M., Ma, R., & Sarmadivaleh, M. (2021). Wettability-dependent Wave Velocities and Attenuation in Granular Porous Media. Submitted to *Geophysics.*

Li, J. X., Rezaee, R., Müller, T. M., Madadi, M., & Sarmadivaleh, M. (2020). Wettability dependent P-wave scattering and velocity saturation relation in granular medium. SEG Technical Program Expanded Abstracts 2020.

Li, J. X., Rezaee, R., Müller, T. M., Madadi, M., Ma, R., & Sarmadivaleh, M. (2021). Path dispersion of elastic waves in granular matter. Paper presented at the SEG/SPWLA 2020 Workshop: 7th Workshop on Porous Media: Structure, Flow and Dynamics, Virtual, 2–3 December 2020.

Chapter 2. Literature Review – Wettability Measurement and Wave Propagation in Porous Media

Wettability as an interfacial phenomenon has a significant influence on the water flooding performance; therefore, it has raised significant research interesting in petroleum engineering, especially the enhanced oil recovery and reservoir engineering. Multiple wettability measurement methods have been developed in the past decades. On the other hand, the study of wave propagation in porous media has been a key element of rock physics and geophysics research. There have been excellent research outcomes in each domain; however, minor research studies how the wettability of the rock impacts the wave propagation. This chapter provides a literature review of wettability measurement and wave propagation in porous media with related experimental works and proposed theoretical models.

2.1. Method of Wettability Measurement

2.1.1. Laboratory Method of Wettability Measurement

The wettability of the porous media has a significant influence on the fluid distribution, capillary pressure, water flooding, residual saturation, etc. A complete literature review about wettability has been given by Anderson (Anderson, 1986a; Anderson, 1986b; Anderson, 1986c; Anderson, 1986d; Anderson, 1986e; Anderson, 1986f).

The most common laboratory techniques to measure the wettability are:

- Contact Angle Method
- Amott Method
- USBM Method

Contact Angle Method

When a droplet of fluid adheres to the solid surface in the environment of another immiscible fluid, the contact angle is defined as the angle between the solid surface and the tangential line of the fluids interface, which varies depending on the wettability. For instance, in a water, oil and rock system, as illustrated in **Figure 2.** ***1*** Wettability system of water, oil, and rock system (Raza et al., 1968).Figure 2. 1 (Raza et al., 1968), if the water wets the rock, the contact angle is below 90°; however, if the water does not wet the rock, the contact angle is higher than 90°.

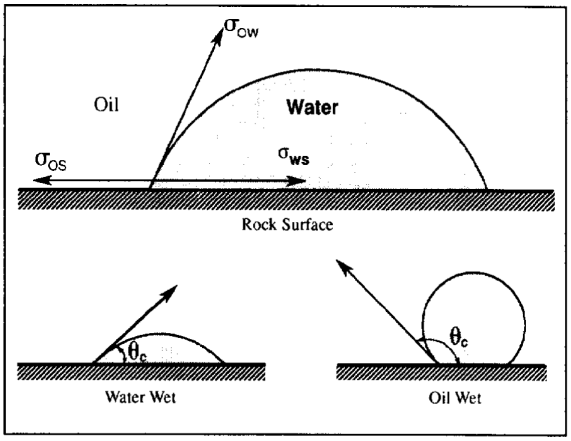

Figure 2.1

Figure 2. 1 Wettability system of water, oil, and rock system (Raza et al., 1968).

The interfacial tension balance along the contact line is well described by Young's equation (Chow, 1998).

$$\sigma_{os} - \sigma_{ws} - \sigma_{ow} cos\theta_c = 0 \tag{2.1}$$

where

σ_{os} = interfacial tension between oil and solid

σ_{ws} = interfacial tension between water and solid

σ_{ow} = interfacial tension between oil and water

θ_c = contact angle.

The contact angle method is accurate and often gives a quantitative value. However, the contact angle is usually affected by the roughness and limited to the small surface area where the testing fluid adheres, making the result unrepresented for the entire porous media.

Amott Method

Different from the contact angle method to measure the wettability of the surface, the Amott method involves the spontaneous and forced imbibition/displacement process, which is more suitable for the porous media wettability determination (Amott, 1959).

Four quantities are required for the Amott method to calculate the wettability index:

V_{ws} = volume of water spontaneously imbibed

V_{wf} = volume of water forcibly imbibed

V_{os} = volume of oil spontaneously imbibed

V_{of} = volume of oil forcibly imbibed.

The modification of the Amott method often used is Amott-Harvey wettability index (WI) for better accuracy.

$$\text{WI(Amott)} = \frac{V_{ws}}{V_{ws}+V_{wf}} - \frac{V_{os}}{V_{os}+V_{of}} \tag{2.2}$$

The positive value of WI indicates the water-wet condition, while the negative value of WI indicates the oil-wet condition.

USBM Method

The USBM method uses the areas under the capillary-saturation plots for the wettability measurement. Typically the capillary pressure curve of the rock core sample is obtained by the centrifuging operation (Figure 2. 2).

The USBM wettability index is calculated by (Donaldson et al., 1969),

$$\text{WI(USBM)} = log\frac{A_1}{A_2} \tag{2.3}$$

where

A_1 = area under the capillary pressure curve for oil displacing water

A_2 = area under the capillary pressure curve for water displacing oil

When $A_1 > A_2$, the rock is water wet, otherwise the rock is oil wet. In the case of $A_1 = A_2$, the rock is neutrally wet sample.

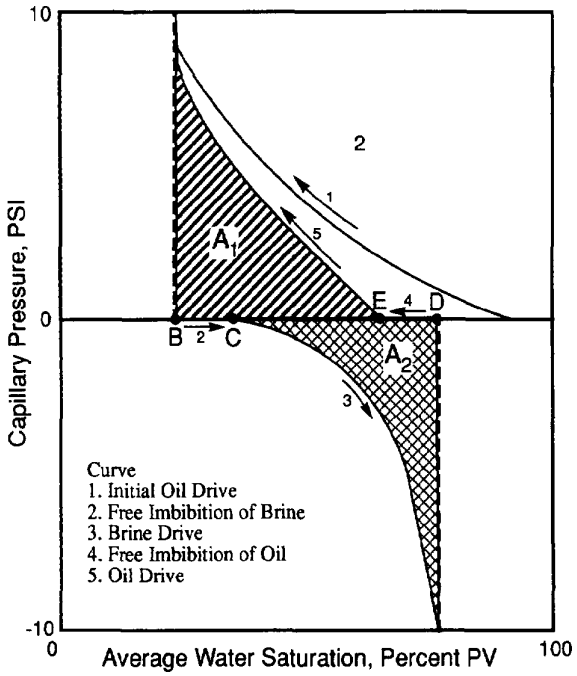

Figure 2. 2 Capillary pressure curves for oil-water displacement in the rock core sample (Anderson, 1986d).

More other approaches include the displacement technique, relative permeability method, capillary rise method, and various modified Amott and USBM methods (Causin and Bona, 1994; Dixit et al., 1998; Ghedan and Canbaz, 2014; Owens and Archer, 1971; Ramakrishnan and Cappiello, 1991; Sharma and Wunderlich, 1987).

2.1.2. Well Logging Approaches to Probe the Reservoir Wettability

Besides the classic methods to obtain quantitative wettability, there have been other approaches introduced by several researchers during the past half-century.

Well logging has been a widely used method to evaluate the geologic formation in the borehole. Various logging techniques, either wireline logging or logging while drilling, have been developd (Zinszner and Pellerin, 2007). Several candidates of well logging approaches could be used to evaluate reservoir wettability, such as nuclear magnetic resonance (NMR), electrical and dielectric logging.

The first attempt to measure the fractional wettability by nuclear magnetic resonance method was developed in the 1950s (Brown and Fatt, 1956) in which the relaxation rate of oil wetting samples as discovered was lower than that of water wetting samples. Graham (1958) used the differential resistivity of original and surfactant injected formation to evaluate rock wettability.

Pirson and Fraser (1960) developed an oil-wet theory from the quantitative interpretation of electric logs (Pirson and Fraser, 1960). Also, Spinler (1996) and Spinler (1997) developed the concepts of Spontaneous Imbibition Index (SII) and apparent wettability based on which he proposed a method to evaluate carbonate reservoir wettability using neural networks. However, Howard (1998) suggested that wettability is related to surface relaxivity, which quantifies the ability of the grain surface to enhance relaxation. He employed the standard Amott method to test the wettability of core samples and the nuclear magnetic resonance method to predict wettability:

$$T_n = C * S_w^b, \tag{2.4}$$

where T_n is the normalized relaxation time between partially and fully water-saturated reservoirs; S_w is the water saturation; b is an indicator correlated with wettability; C is the constant.

Guan et al. (2002) analyzed the Amott-Harvey index with the differences and ratios in the relaxation time distributions (for both longitudinal magnetizations build up time T_1 and transverse magnetization decay time T_2). Relaxation time differences were defined as ΔT_1 = (T_1at S_{or}) - (T_1 at S_{wi}), ΔT_2 = (T_2 at S_{or}) - T_2 at S_{wi}). And relaxation time ratio was defined as (T_1 at S_{wi})/(T_1 at S_{or}), (T_2 at S_{wi})/(T_2 at S_{or}), where S_{wi} is irreducible water saturation, and S_{or} is residual oil saturation. They found the relaxation time differences and ratio had a good linear relationship with the Amott-Harvey wettability index. The relaxation time difference decreases linearly as the samples are more water-wet and the relaxation time ratio increases linearly when the samples are more water-wet.

Looyestijn and Hofman (2006) also studied several core samples under nuclear magnetic resonance experiments and found the wettability was a function of total wetting and non-wetting surface. Cheng et al. (2016) synthesized two capillary pressure curves from both typical logging data and nuclear magnetic resonance data. They established a forecasting model based on the correlation between the wettability and the ratio of median pore radius derived from the two capillary pressure curves.

Overall, the previous researches described above have extended the knowledge of the relationship between NMR well logging data and wettability. However, the relationship between wettability as a whole with sonic logging data (elastic wave) has not yet been studied. This thesis will examine both theoretical and practical methods to obtain a reliable wettability estimation correlation quantitatively by the elastic wave measurement.

2.2. Theory of Wave Propagation in Saturated Porous Medium

The propagation of the elastic wave in the fluid saturated porous medium, especially its velocity dispersion and attenuation, has drawn significant attention from scientists and engineers. In the domain of the exploration geophysics, it is very common to observe the wave dispersion and attenuation where the dispersion refers to the phenomenon that wave velocities vary with different frequencies in the same rock, and the attenuation means the wave energy loss during the wave transmission. These two features are the most commonly applied in the interpretation of seismic and sonic logging data to obtain geological and geophysical signatures and reservoir properties.

In the past decades, there have been various researches on geophysics and rock physics (Mavko et al., 2009); especially, the studies on the dispersion and attenuation due to the wave-induced flow of pore-filling fluid during the wave propagation have developed several theoretical models (Biot, 1956a; Biot, 1962; Johnson et al., 1987; Mavko and Nur, 1979; Müller et al., 2010) and multiple experimental methodologies (Bacri and Salin, 1986; Cadoret et al., 1995; Cadoret et al., 1998; Gregory, 1976; Lebedev and Lopes, 2013; Lebedev et al., 2009; Murphy III, 1984; Wyllie et al., 1956). The viscous frictional attenuation because of the wave-induced-fluid-flow (WIFF) is related to the multiple scale (pore-scale, mesoscopic and macroscopic) heterogeneities (Figure 2. 3). Seismic transmission has been a key element for these studies where the elastic properties of the rock composite and even the fluid properties can be predicted by the arrival time and the amplitude of receiving waves.

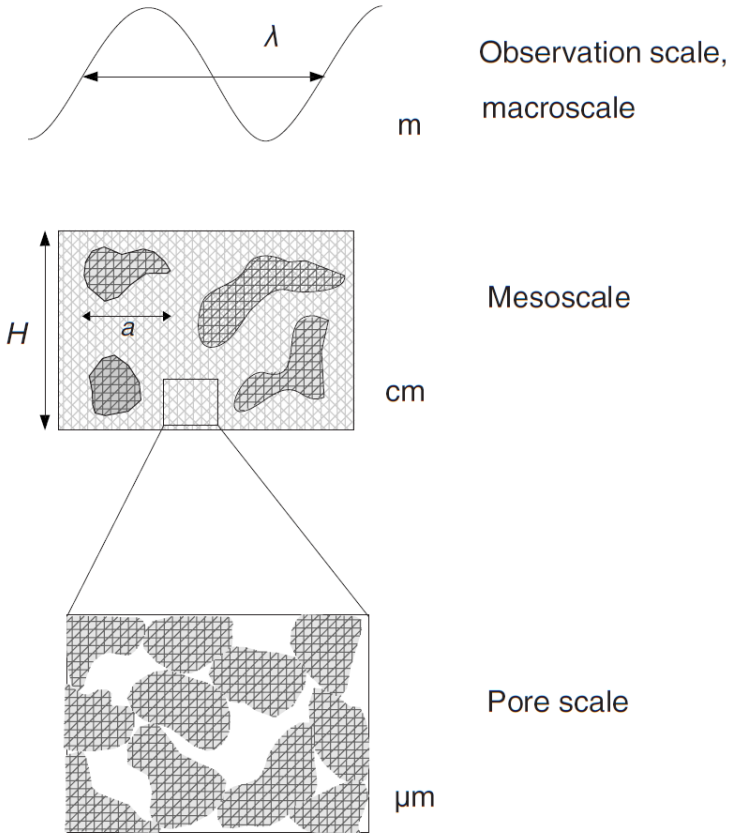

Figure 2. 3 Multiple scale heterogeneity related to the elastic wave attenuation (Müller et al., 2010).

2.2.1. Gassmann Equations of the Application in the Multiple Fluids Saturated Rock

The early study on the wave propagation problem in the porous medium began in the 1940s (Beranek, 1947; Biot, 1941). Gassmann (1951) developed a theory of fluid substitution, which is the so-called Gassmann equations bringing in the porosity effect. Gassmann equations are the fundamental theoretical basis established for the inversion of wave velocities and the elastic moduli. In the application of the seismic wave in the oil reservoir surveillance, one of the important questions is how to predict the velocity of one fluid saturated rock by a given velocity of the same rock but saturated by another fluid. It is actually required to establish a relationship between the wave velocity of dry rock (solid frame) and the velocity of the saturated rock, which is known as the fluid substitution problem. The essential part of the fluid substitution is to predict the wave velocity from the reservoir condition petrophysical parameters such as temperature, pressure, porosity, mineralogy of the rock, etc. The velocities can be calculated by the density, bulk and shear modulus, or any two of the major elastic moduli: compressional wave modulus, Young's modulus, Poison's ratio, and Lame's parameter.

For an isotropic reservoir rock, the bulk modulus of the saturated rock K_G calculated by the Gassmann equation is (Mavko et al., 2009):

$$K_G = K_d + \frac{\left(1-\frac{K_d}{K_s}\right)^2}{\frac{\phi}{K_f}+\frac{1-\phi}{K_s}-\frac{K_d}{K_s^2}}. \tag{2.5}$$

The shear modulus of the saturated rock μ_G in Gassmanna's equations is assumed the same as the dry rock based on the assumption that the shear modulus of the fluid is zero.

$$\mu_G = \mu_d. \tag{2.6}$$

K_d and μ_d are the bulk and shear modulus of the dry frame, respectively; K_s is the bulk modulus of the solid matrix; K_f is the bulk modulus of the pore-filling fluid; ϕ is the porosity (volume ratio of the pore void).

The K_d and μ_d can be determined by the measurements of the P and S wave velocities on the dry rock.

$$K_d = \rho_d \left(V_{p\_dry}^2 - \frac{4}{3}V_{s\_dry}^2\right), \tag{2.7}$$

$$\mu_d = \rho_d V_{s\_dry}^2. \tag{2.8}$$

The density of the dry rock can be simplified as $\rho_d = (1-\phi)\rho_s$ because the density of the pore filling air is negligible small comparing to the density of the mineral solid ρ_s.

More than often in the natural reservoir rock, the solid matrix is a composite consisting of several minerals; in this case, the bulk modulus of solid K_s can be obtained by the Voigt-Reuss-Hill (VRH) average method (Berryman and Thigpen, 1985; Domenico, 1976; Zuo et al., 1992). It is a combined algorithm of Voigt average and Reuss average of the *n* type minerals' bulk moduli K_{si}, where the volume ratio of each ingredient is F_i $(i = 1,2,\dots n)$:

$$K_{Reuss} = \frac{F_1}{K_{s1}} + \frac{F_2}{K_{s2}} + \cdots + \frac{F_n}{K_{sn}}, \tag{2.9}$$

$$K_{Voigt} = K_{s1}F_1 + K_{s2}F_2 + \cdots + K_{sn}F_n, \tag{2.10}$$

$$K_s = \frac{1}{2}\left(K_{Reuss} + K_{Voigt}\right). \tag{2.11}$$

The density of the saturated rock is,

$$\rho_{sat} = \rho_s(1-\phi) + \rho_f\phi. \tag{2.12}$$

Once the bulk and shear moduli are obtained according to equation (2.5) and (2.6), the velocities of P and S wave can be precited as,

$$V_p = \sqrt{\frac{K_G + \frac{4}{3}\mu_G}{\rho_{sat}}}, \tag{2.13}$$

$$V_s = \sqrt{\frac{\mu_G}{\rho_{sat}}}. \tag{2.14}$$

In summary, the velocities can be predicted by Gassmann equations for the given fluid saturated reservoir rock with a known solid frame and fluid parameters. On the other hand, the Gassmann equations can be used for fluid substitution. If the velocities of saturated rock are known, the bulk and shear moduli of the solid frame can also be calculated. Then, one can also predict the velocities of the rock saturated with another fluid. For example, the bulk modulus of reservoir rock saturated by the 2nd fluid K_{sat2} can be calculated if the bulk moduli of the rock saturated by the original fluid K_{sat1} (Mavko et al., 2009):

$$K_{sat2} = K_s \frac{\frac{K_{sat1}}{K_s - K_{sat1}} - \frac{K_{f1}}{\phi(K_s - K_{f1})} + \frac{K_{f2}}{\phi(K_s - K_{f2})}}{1 + \frac{K_{sat1}}{K_s - K_{sat1}} - \frac{K_{f1}}{\phi(K_s - K_{f1})} + \frac{K_{f2}}{\phi(K_s - K_{f2})}}. \tag{2.15}$$

K_{f1} and K_{f2} are the bulk moduli of the original and the 2nd fluids, respectively.

In the verification of the Gassmann equations for fluid substitution, it is found that the measured bulk modulus of the dry rock (i.e., vacuum oven-dried) is higher than the predictions (Mavko et al., 2009). A tiny portion of the fluid/moisture is required to be added to the dry frame to make the measurement and theory prediction match each other. It means that the "dry frame" in the Gassmann equations for fluid substitution is actually a slightly humid solid frame. One of the assumptions of Gassmann equations is that the fluid has no chemical interaction with the solid frame. However, this assumption may be invalid for some natural sedimentary rocks as the pore-filling fluid inevitably interacts with the solid interface so as to change the strain of interfaces. For example, the bulk modulus and shear modulus of the solid frame for heavy oil saturated unconsolidated rock is higher than the prediction (Guo and Han, 2016). The moduli of the water-saturated laminated sandstone is softened due to the clay swelling effect after water absorption (Nie et al., 2008). In addition, the bulk modulus of the "dry frame" in the Gassmann equations is not the same as that of the gas saturated porous medium but a parameter associated with volume change under the external stress in the condition of constant pore pressure. It may be approximated by the bulk modulus of the air saturated rock in the standard

temperature and pressure. However, in the high-pressure-high-temperature (HPHT) reservoir condition, the moduli of the gas in the pores cannot be ignored and such gas-saturated rock should not be treated as a "dry frame".

Other assumptions of Gassmann equations include 1. The bulk modulus of the solid K_s maintains the same everywhere, which requires the composite of the minerals are homogenously mixed; 2. The pore space is statistically isotropic which means that the wavelength should be much larger than the individual pore or grain size. Although the frequency of the transiting signals and the condition of most rock specimen meet the requirements of these assumptions in the laboratory, the Gassmann equations simplifies the pore geometry and ignores the tortuous feature of the pore network, which make the theory hardly being used to study fluid dynamics on the micro-scale and corresponding energy dissipation thereby.

For a typical reservoir rock with a heterogeneous pore network (therefore uneven fluid distribution) and saturated by multiple fluids, it can be softened or stiffened depending on the signal frequencies (Cadoret et al., 1995; Carcione et al., 2003; Ruiz and Azizov, 2011). In the low-frequency range, the equivalent bulk modulus of the fluid can be calculated by the Wood equation, which is the Reuss average value for the fluids' bulk moduli (Smith et al., 2003):

$$K_{\mathrm{f}} = \left(\frac{S_1}{K_{\mathrm{f1}}} + \frac{S_2}{K_{\mathrm{f2}}} + \cdots + \frac{S_n}{K_{\mathrm{fn}}}\right)^{-1}, \tag{2.16}$$

S_i and $K_{\mathrm{f}i}(i = 1,2,\ldots n)$ are the saturation and the bulk modulus of the individual saturating fluid, respectively.

Substitute it into the Gassmann equations, and one can calculate the bulk modulus of the rock saturated by multiple fluids, and the shear modulus remains unchanged. Together, it is called Biot-Gassmann-Wood (BGW) model (Toms et al., 2007), which requires

1. all pores are interconnected;

2. pore pressure maintains equilibrium at all the time and

3. the mix-fluids spatial distribution is homogenous.

Therefore, BGW model describes the condition of extreme relaxation between the fluids and the saturated rock as "soften"; the bulk modulus of a rock saturated by multiple fluids in BGM model is the lowest limit in the whole frequency range.

In fact, in the real reservoir, such relaxation conditions between different fluid phases almost never happen due to the capillary effect. The wetting fluid always covers the solid surface and occupies the small pores, which can be considered as a background fluid phase. In contrast, the non-wetting fluid conceived as embedded phase (i.e., patchy-saturation) is forced to stay in the relatively large pores and might be snapped off in discrete segments by the wetting fluids. For a neutral and fractional wettability condition, the distribution of the different immiscible fluids could be even more complicated. When a high-frequency incoming wave passes through rock with mix-saturation, the non-wetting and wetting fluids cannot balance the pressure differential in such a short expansion-retraction wave-cycle; therefore, the pressure equilibrium is broken, rendering the entire rock in a "stiffen" status. Müller and Gurevich (2004) and Toms et al. (2006) find that the high limit of the bulk modulus of such "stiffen" saturated rock could be predicted by the Biot-Gassmann-Hill (BGH) model, which incorporates the Hill average (Hill, 1963) into the Gassmann equations. The bulk modulus of the mix-saturated rock K_{sat} calculated by BGH model is,

$$\frac{1}{K_{sat}+\frac{4}{3}\mu_G} = \frac{S_1}{K_{sat1}+\frac{4}{3}\mu_G} + \frac{S_2}{K_{sat2}+\frac{4}{3}\mu_G} + \cdots \frac{S_n}{K_{satn}+\frac{4}{3}\mu_G} \tag{2.17}$$

$K_{sati}(i = 1,2, \dots n)$ is the bulk modulus of the rock saturated by individual single fluid calculated by the Gassmann equations.

The equivalent fluid density ρ_{f} is calculated by the volume average method from the individual fluid density ρ_{fi},

$$\rho_{\mathrm{f}} = \rho_{\mathrm{f1}} S_1 + \rho_{\mathrm{f1}} S_2 + \cdots + \rho_{\mathrm{f1}} S_n. \tag{2.18}$$

Thus, by using the BGW and BGH model combined with equation (2.16-2.18), one can calculate the velocities of the rock saturated by multiple fluids in either the low frequency or the high-frequency range.

Toms et al. (2006) recognize the P wave velocity calculated by BGH model represents the highest limit of the elastic wave in the high-frequency limit. In such a case, the local flow is unlikely to happen, and the rock is in the "hardest" status. However, the principle of Hill average is based on the static mechanics of solid mixture/compound. Therefore, one hidden assumption of equation (2.17) is that the wetting and non-wetting fluids are required to have a tight bond with the solid, and the pressure differential between fluids is only equilibrated by the solid, which is almost impossible for the non-wetting fluid.

Domenico (1976) and Nie et al. (2012) use Voigt average to calculate the equivalent bulk modulus of the mix-fluids,

$$K_{\mathrm{f}} = S_1 K_{\mathrm{f1}} + S_2 K_{\mathrm{f2}} + \cdots + S_n K_{\mathrm{fn}}. \tag{2.19}$$

Substitute equation (2.19) into the Gassmann equations, one obtains the Biot-Gassmann-Voigt (BGV) model, which describes the condition of the inhomogeneous mix of the immiscible fluids where in the low-moderate permeability formation there exists the patchy saturation of non-wetting fluid (Mavko and Nolen-Hoeksema, 1994). The strain of each fluid phase is assumed to be the same, but the pressure is imbalanced so that the mix-fluids are in the most unrelaxed condition and the equivalent bulk modulus reaches the highest value. In sum, there is relation $K_{sat}(BGV) > K_{sat}(BGH) > K_{sat}(BGW)$.

2.2.2. Biot Theory of Poroelasticity

Following Gassmann's work, Wyllie et al. (1956) further create a model to assume the solid and fluid interlayered structure to calculate the velocity. Although the Gassmann equation and Wyllie model are simple and efficient in the calculation but it is far from enough to cover the complicated acoustic signatures for the fluid effect in the porous medium. It has been widely known now that wave dispersion and attenuation are mainly raised by the flow of the pore-filling fluids. When a wave passes through the saturated porous medium, the relative fluid flow with respect to the solid occurs due to the pressure gradient generated by the out-of-phase motion between the solid and fluid phases and the microscopic inhomogeneity of fluid distribution. Such the wave-induced-flow further results in frictional dissipation until the pressure equilibrium is restored. According to the characteristic size of the pressure gradience causing the fluid flow, the wave-induced-flow is categorized into three types: macroscopic flow, microscopic flow, and mesoscopic flow.

The macroscopic flow, also called global flow, is the fundamental form of wave-induced-flow. When the frequency is high, the fluid pressure gradient is created by the peak and trough of the wave; therefore, the relative motion of fluid with respect to the solid occurs; at this time, the assumption of Gassmann's theory is no longer valid. To tackle this problem, Biot (1956a) constructs the dynamic poroelasticity theory for isotropic porous medium saturated by fluid based on Darcy law and the Poiseuille flow model. Carcione (2015) and Qi (2015) have respectively made a detailed description of the derivation process of the equations of motion

for Biot theory by the Lagrangian principal and provided the solutions for velocities and attenuation of P and S waves. The equations of motion (Biot, 1956a; Biot, 1956b) are:

$$N\nabla^2 u + (A+N)\nabla(\nabla\cdot u) + Q\nabla(\nabla\cdot U) = \rho_{11}\ddot{u} + \rho_{12}\ddot{U} - \frac{F\mu_{\mathrm{f}}\emptyset^2}{\kappa_0}\left(\dot{U}-\dot{u}\right), \tag{2.20a}$$

$$Q\nabla(\nabla\cdot u) + R\nabla(\nabla\cdot U) = \rho_{12}\ddot{u} + \rho_{22}\ddot{U} + \frac{F\mu_{\mathrm{f}}\emptyset^2}{\kappa_0}\left(\dot{U}-\dot{u}\right). \tag{2.20b}$$

u and $U$are the average displacements of the solid and fluid, respectively; the single dot and the double dot above them represent first-order and second-order time derivatives, respectively; ∇ is the Laplace operator; μ_{f} is the shear viscosity of the pore-filling fluid; F is the viscosity correction factor, which equals to 1 ($F=1$) in the low-frequency Biot theory; κ_0 is the permeability of the porous medium.

The elastic parameters are,

$$N = \mu_d, \tag{2.21a}$$

$$A = \frac{(1-\phi)\left(1-\phi-\frac{K_d}{K_s}\right)K_s + \phi\left(\frac{K_s}{K_{\mathrm{f}}}\right)K_d}{1-\phi-\frac{K_d}{K_s}+\phi\left(\frac{K_s}{K_{\mathrm{f}}}\right)} - \frac{2}{3}N, \tag{2.21b}$$

$$Q = \frac{\left(1-\phi-\frac{K_d}{K_s}\right)\phi K_s}{1-\phi-\frac{K_d}{K_s}+\phi\frac{K_s}{K_{\mathrm{f}}}}, \tag{2.21c}$$

$$R = \frac{\phi^2 K_s}{1-\phi-\frac{K_d}{K_s}+\phi\frac{K_s}{K_{\mathrm{f}}}}, \tag{2.21d}$$

and the density parameters are,

$$\rho_{11} = (1-\phi)\rho_s + [T-1]\phi\rho_{\mathrm{f}}, \tag{2.21e}$$

$$\rho_{12} = [1-T]\phi\rho_{\mathrm{f}}, \tag{2.21f}$$

$$\rho_{22} = \phi\rho_{\mathrm{f}} + [T-1]\phi\rho_{\mathrm{f}}. \tag{2.21g}$$

The parameter T is the tortuosity.

A pair of equivalent equations of motion for Biot theory is also derived by Biot (1962). These two sets of equations are fully equivalent to each other. The highlight is that, in the later ones, the relative displacement of fluid $w = \phi(U-u)$ is used instead of the absolute fluid displacement u.

The predictions of the Vp and Vs by the Biot theory agree with Gassmann's theory in the low frequency but appear as a step shape and reach higher velocities in the high frequencies. The characteristic frequency $\omega_B = \frac{\mu_f \phi}{T \kappa_0 \rho_f}$, also called Biot frequency represents the highest attenuation peak and separates the viscous-dominated low-frequency range and the inertia-dominated high-frequency range.

Biot theory assumes, during the wave excitation, the pore-filling fluid conducts Poiseuille laminated flow inside the pore network. When the frequency is beyond the crossover frequency, the Poiseuille flow is no longer valid so that Biot (1956b) further works out a correction model for the high-frequency range based on the analysis of the average velocity and the viscous friction force on the simple cylindrical and slit shape pores. The result is using a corrected viscosity $F\mu_f$ to replace the original viscosity μ_f in equation (2.20-2.21) so that the equations of motion are suitable for the whole frequency range. The viscosity correction factor F is an indicator of the deviation of the global flow from the Poiseuille flow.

In the original paper, (Biot, 1956b) use Fourier convention $\exp(i\omega t)$. Here, the viscosity correction factor F for two types of pores under $\exp(-i\omega t)$ are written as,

$$F(k) = -\frac{1}{4}\frac{krJ_1(kr)}{J_2(kr)}, \text{ Cylindrical shape pore} \tag{2.22a}$$

$$F_1(k) = \frac{1}{3}\frac{ikr_1 tanh(ikr_1)}{1-\frac{1}{ikr_1}tanh(ikr_1)}, \text{ Slit shape pore} \tag{2.22b}$$

where r is the radius of the cylindrical pore and r_1 is half of the opening of the slit pore; i is the unit of the imaginary part of complex values; $J_n(n = 0,1)$ is Bessel function of n order.

The oscillating viscous flow in the pores is a process of viscous diffusive wave generated on the solid boundary and propagate towards the interior bulk fluid (Li et al., 2020a). The parameter $k = \sqrt{\frac{i\omega}{D_v}}$ is the wavenumber of the viscous diffusive wave with its diffusivity $D_v = \mu_f/\rho_f$.

By the analysis of the asymptotic values of F and F_1, Biot (1956b) find that $F(k) \cong F_1(k)$ when

$$\frac{r_1}{3} = \frac{r}{4}. \tag{2.23}$$

Alternatively,

$$F(k) \cong F_1\left(\frac{3}{4}k\right), \tag{2.24a}$$

$$F_1(k) \cong F(\frac{4}{3}k). \tag{2.24b}$$

Therefore, the viscous corrector factor can be unified to be one model by using a "structure factor" ξ. For example,

$$F(\omega) = \frac{1}{3}\frac{ikrtanh(ikr)}{1-\frac{1}{ikr}tanh(ikr)}, \tag{2.25a}$$

$$k = -i\xi\sqrt{\frac{i\omega\mu_{\mathrm{f}}}{\rho_{\mathrm{f}}}}. \tag{2.25b}$$

When $\xi = 1$ corresponds to slit pore shape model; $\xi = \frac{3}{4}$ corresponds to the cylindrical model and $\frac{3}{4} < \xi < 1$ represents a combined pore shape model.

By the analysis of the potential flow and the boundary layer viscous flow under the oscillating pressure gradient, Johnson et al. (1987) develop the theory of dynamic permeability and tortuosity for porous medium. When the Biot model is corrected by the viscosity correction factor, a similar dynamic permeability model can also be derived.

The low-frequency kinetic equation for the fluid in Biot theory can be written as (Biot, 1962; Carcione, 2007),

$$-\nabla p_{\mathrm{f}} = \rho_{\mathrm{f}}\ddot{u} + m\ddot{w} + \frac{\mu_{\mathrm{f}}}{\kappa_0}\dot{w}, \tag{2.26}$$

where p_{f} is the fluid pressure; $m = \rho_{\mathrm{f}}T/\phi$.

By considering the high-frequency correction on viscosity, equation (2.26) changes to,

$$-\nabla p_{\mathrm{f}} = \rho_{\mathrm{f}}\ddot{u} + m\ddot{w} + \frac{F\mu_{\mathrm{f}}}{\kappa_0}\dot{w}. \tag{2.27}$$

If we consider a plane-wave solution in the x-axis direction, varying as harmonic excitation $e^{\mathrm{i}\omega t}$, we can re-write the equation (2.27) in the frequency domain as,

$$-\nabla p_{\mathrm{f}} = -\omega^2\rho_{\mathrm{f}}u - \omega^2 mw + i\omega w\frac{F\mu_{\mathrm{f}}}{\kappa_0}. \tag{2.28}$$

It can be further recast as,

$$\mathrm{i}\omega w = \frac{k_0}{F+\frac{im\kappa_0\omega}{\mu_{\mathrm{f}}}}\left(-\nabla p_f + \rho_{\mathrm{f}}\omega^2 u\right)\frac{1}{\mu_{\mathrm{f}}}. \tag{2.29}$$

Therefore, the term $\frac{\kappa_0}{F_B+\frac{\mathrm{i}m\kappa_0\omega}{\mu_\mathrm{f}}}$ in this equation acts as dynamic permeability,

$$\kappa_B(\omega) = \frac{\kappa_0}{F_B+\frac{\mathrm{i}\omega T\kappa_0\rho_\mathrm{f}}{\mu_\mathrm{f}\emptyset}}. \tag{2.30}$$

We should notice that equation (2.30) is different from the definition of Biot estimation of dynamic permeability in the reference (equation (85) in (Pride et al., 1993)) which is based on drag force analysis.

Equation (2.30) is the relation of the frequency depend on tortuosity and permeability under harmonic excitement $e^{i\omega t}$ by analogy with the case using the opposite convention for the sign of Fourier transform in reference (Johnson et al., 1987).

$$T_B(\omega) = -\frac{i\mu_\mathrm{f}\phi}{\kappa_B(\omega)\omega\rho_\mathrm{f}}. \tag{2.31}$$

Substituting equation (2.30) into equation (2.31), one obtains the dynamic tortuosity of high-frequency Biot theory version as,

$$T_B(\omega) = \mathrm{T} - \frac{i\mu_\mathrm{f}\phi F}{\omega\kappa_0\rho_\mathrm{f}}. \tag{2.32}$$

One of the prominent features of Biot theory is that it predicts there is a slow P- wave in the fluid saturated porous medium, which is a pressure diffusion process (citation). Slow P- wave is experimentally detected by Plona (1980). Berryman (1980) applies the Biot theory to the experimental result of Plona (1980) successfully, which proves the feasibility of the theory. Later on, the slow P wave is also detected in the water-saturated sandstone in the ultrasonic frequency range (Kelder and Smeulders, 1997).

Moreover, the partial differential equations in the Biot theory enable the numerical simulation of the elastic wavefield in the porous medium. For the past decades, researchers have developed several numerical methods for the wavefield, including finite difference method (FDM) (Wenzlau and Müller, 2009), pseudo-spectral method (PSM) (Furumura et al., 1998), finite element method (FEM) (Ichimura et al., 2007), spectral element method (SEM) (Komatitsch and Tromp, 1999), and etc.

Although Biot theory has been widely used in the study of wave dispersion and attenuation in the saturated porous medium, it is still challenging to explain the actual observation data especially in the low-frequency (i.e., seismic) range (Buckingham, 2000; Gist, 1994; Johnston et al., 1979; Jones, 1986; Winkler, 1985). For the majority of the natural reservoir rock with

complicated pore networks and low permeability, the dispersion and attenuation mechanism may be mainly caused by the micro-scale fluid frictional dissipation.

2.2.3. Squirt Flow Models

The global flow described by the Biot theory is a macroscopic wave-induced-fluid-flow where the direction of the flow is mainly along with the wave propagation. However, the micro-fluid flow field in the small dimension geometry in the pore network has been ignored, which may cause the underestimation of the energy dissipation and the corresponding wave dispersion and attention.

Mavko and Nur (1975) proposed the first version of the squirt flow model, which identifies a squirt flow mechanism for the fluid flow in the tiny fracture-like pores occurring in the direction perpendicular to the wave propagation. The squirt flow only occurs in the local area with a much smaller characteristic length than the macroscopic global flow, which is an important part of the wave energy dissipation. The prediction of the attenuation of the squirt flow model significantly exceeds that of Biot theory (Mavko and Nur, 1979). Meanwhile, the experiments show, if there are fracture-like pores in the pore network, the attenuation in the partially saturated (water and air) rock will increase significantly even if a very small portion of water is added into the pores, which may be explained by the squirt flow model (Mavko and Nur, 1979).

The squirt flow model accounting for the local flow mechanism has been widely used to explain the “non-Biot” dissipation (Mavko and Nur, 1979; O'Connell and Budiansky, 1974; O'Connell and Budiansky, 1977; Winkler, 1985; Winkler, 1986). The local flow account for the “non-Biot” dissipation occurs in the pore-scale have been further studied theoretically (Gurevich et al., 2010; Mavko and Jizba, 1991; Mavko and Nur, 1979; O'Connell and Budiansky, 1974; O'Connell and Budiansky, 1977) and experimentally (Han et al., 2018; Mavko and Jizba, 1994; Murphy III, 1984; Wang and Nur, 1988; Wulff and Burkhardt, 1997).

One of the assumptions for squirt flow is that the pores are categorized into two kinds: the compliant (soft) pores with a small aspect ratio (height/length), and equant (stiff) pores with a large aspect ratio. The process of the squirt flow is that during the excitation of the external acoustic perturbation, the pore-filling fluid inside the compliant pore squirt into the neighboring equant pore in the local area while squirt flow in the macro-scale is still statistically zero; however, the energy dissipation thereby is nontrivial.

Dvorkin and Nur (1993) apply the squirt flow model into the Biot theory and create a new model called the BISQ model. In the BISQ model, the reprehensive equivalent volume (REV) is considered as a cylindrical sponge within which squirt flow, and global flow occur at the same time during wave propagation (Figure 2. 4).

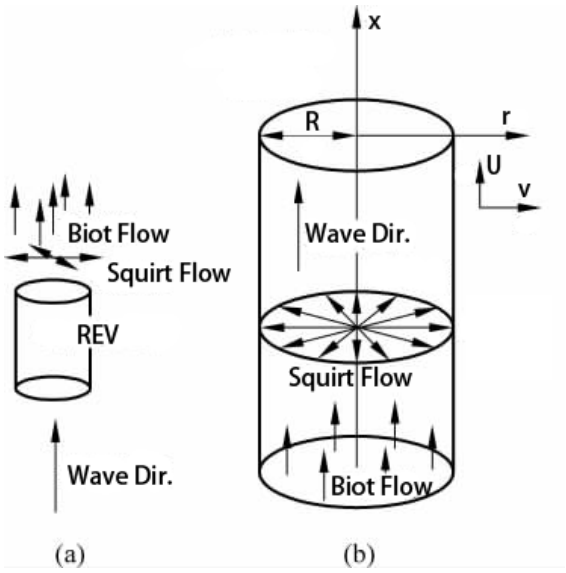

Figure 2. 4 The BISQ model. (a) Biot flow and squirt flow in a rock due to seismic excitation; (b) A cylindrical representative volume of a rock.

In the original Biot Theory (Biot, 1956a), the dynamical equations for the fluid saturated porous medium are,

$$(1-\phi)\rho_s\ddot{u} + \phi\rho_{\mathrm{f}}\ddot{U} = M\frac{\partial^2 u}{\partial x^2} - \alpha\frac{\partial P}{\partial x}, \tag{2.33a}$$

$$-\phi\frac{\partial P}{\partial x} = \phi\rho_{\mathrm{f}}\ddot{U} - m\left(\ddot{u}-\ddot{U}\right) - \frac{\mu_{\mathrm{f}}\phi^2}{\kappa_0}\left(\dot{u}-\dot{U}\right). \tag{2.33b}$$

The pressure rate is,

$$\frac{\partial P}{\partial t} = -F_{sq}\left(\frac{\partial \dot{U}}{\partial x} + \frac{\alpha-\phi}{\phi}\frac{\partial \dot{u}}{\partial x}\right), \tag{2.34a}$$

$$F_{sq} = \left(\frac{1}{\rho_f c_0^2} + \frac{1}{\phi Q}\right)^{-1}. \tag{2.34b}$$

where the elastic parameters are,

$$\alpha = 1 - \frac{K_d}{K_s}, \tag{2.35a}$$

$$M = \left(\frac{\alpha-\phi}{K_s} + \frac{\phi}{K_\mathrm{f}}\right)^{-1}. \tag{2.35b}$$

c_0 is the velocity of elastic wave in the fluid, and the elastic parameter Q can be determined by equation (2.21c).

In fact, equation (2.33) describes one-dimension (x-direction) movement where u and U represent the displacement of solid and fluid on the x-direction. For the same reason, equation (2.34) can also only describes one-dimension deformation. However, the fluid inside the cylinder REV may conduct the flow in the radial direction, which is normal to the wave propagation direction. Dvorkin and Nur (1993) add the fluid flow term in the radical direction for equation (2.30), and the new formula is,

$$\frac{\partial P}{\partial t} = -F_{sq}\left(\frac{\partial \dot{U}}{\partial x} + \frac{\alpha-\phi}{\phi}\frac{\partial \dot{u}}{\partial x} + \frac{\partial \dot{\mathrm{v}}}{\partial x} + \frac{1}{r}\dot{\mathrm{v}}\right), \tag{2.36}$$

v is the displacement of fluid in the radial direction. This equation is a constitute equation for the fluid strain and stress in a 3D cylinder space. At the same time, the kinetic equation for the radical fluid flow following equation (2.33b) is,

$$-\phi\frac{\partial P}{\partial r} = (\phi\rho_\mathrm{f} + m)\ddot{\mathrm{v}} + \frac{\mu_\mathrm{f}\phi^2}{\kappa_0}\dot{\mathrm{v}}. \tag{2.37}$$

By solving the partial differential equation (2.36-2.37) and introducing the squirt characteristic length R (radius of the cylinder REV), the new pressure rate is obtained,

$$\frac{\partial P}{\partial t} = -F_{sq1}\left(\frac{\partial \dot{U}}{\partial x} + \frac{\alpha-\phi}{\phi}\frac{\partial \dot{u}}{\partial x}\right), \tag{2.38a}$$

The new coefficient for squirt flow $F_{sq1}$is,

$$F_{sq1} = F_{sq}\left[1 - \frac{2J_1(\lambda R)}{\lambda R J_0(\lambda R)}\right], \tag{2.38b}$$

$$\lambda = \left[\frac{\rho_\mathrm{f}\omega^2}{F}\left(\frac{\phi + m/\rho_\mathrm{f}}{\phi} + i\frac{\mu_\mathrm{f}\phi}{\kappa_0\rho_\mathrm{f}\omega}\right)\right]^{\frac{1}{2}}. \tag{2.38c}$$

The BISQ model is a unified model incorporating the squirt flow into the Biot mechanism, which is big progress for people to understand the wave energy dissipation at the microscopic level. However, the geometry model is still too simple to represent the complicated pore morphology. The new parameter R as the characteristic length is also an unclear concept in rock physics. From the perspective of fluid mechanics, the weakness of BISQ is in equation (2.37) in which the wave propagation in the x-direction results in the fluid flow in the radial

direction. However, the wave-induced-flow should mainly occur in the direction of the pressure gradient, x-direction, rather than other directions. Therefore, the pressure in equation (2.37) promotes the Biot flow and radical squirt flow at the same time, whereby the pressure might be overused.

In addition to the BISQ model, Mavko and Jizba (1991) provide a solution for the grain-scale local flow effect on the velocity dispersion and attenuation in the high frequency. It assumes the frame of fluid saturated rock is actually an unrelaxed wet frame whose compressibility is approximated by that of the dry frame in high confining pressure. A concept of a modified frame is created where only compliant/soft pores are saturated by fluid to describe the unrelaxed solid frame. The bulk and shear moduli of the pressure-dependent modified frame are,

$$\frac{1}{K_{uf(P)}} \approx \frac{1}{K_h} + \left(\frac{1}{K_f} - \frac{1}{K_s}\right)\phi_c(P), \tag{2.39a}$$

$$\frac{1}{\mu_{uf(P)}} \approx \frac{1}{\mu_{dry(P)}} - \frac{4}{15}\left(\frac{1}{K_{dry(P)}} - \frac{1}{K_{uf(P)}}\right). \tag{2.39b}$$

$K_h$is the bulk modulus of the dry frame under very high pressure when most of the compliant pores are closed. ϕ_c is the porosity of the compliant pores, which occupy 0.1% or even less of the rock volume.

By substituting these moduli of the modified frame into the Gassmann equations (equation 2.5-2.6), one can obtain the moduli of the fluid saturated rock.

Following the Mavko-Jizba squirt theory, Gurevich et al. (2010) developed a simple squirt flow modal for the sandstone in the ultrasonic frequency in which the geometry of compliant-stiff pore model proposed by Murphy III et al. (1986) is considered (Figure 2. 5).

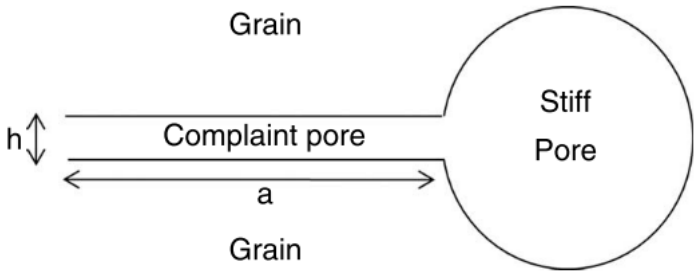

Figure 2. 5 Sketch of the model configuration (Murphy III et al., 1986). Soft pore forms a disc-shaped gap between two grains, and its edge opens into a toroidal stiff pore.

In this simple squirt flow model, the shear modulus keeps constant as it in the Mavko-Jizba squirt flow model, but the bulk modulus of the modified frame is,

$$\frac{1}{K_{uf}} = \frac{1}{K_h} + \left[\left(\frac{1}{K_{dry}} - \frac{1}{K_h}\right)^{-1} + \left(\frac{1}{K_f^*} - \frac{1}{K_s}\right)^{-1} \phi_c^{-1}\right]^{-1}, \tag{2.40}$$

The key factor in this model is the effective bulk modulus of the fluid-filled inside the compliant pores:

$$K_f^* = i\omega\eta^*, \tag{2.41a}$$

$$\eta^* = \frac{3}{2}\left(\frac{a}{h}\right)^2 \eta, \tag{2.41b}$$

where a and h are the radius and thickness of the compliant pore, respectively, the aspect ratio is $h/a \ll 1$.

We can see that the simple squirt flow model is based on the same promise of the binary pore structure as other squirt flow models: compliant pores and stiff pore as other squirt flow models where the former is responsible for the squirt flow related poroelastic dynamic moduli due to pressure change. Carcione and Gurevich (2011) incorporate the simple squirt flow model into the Biot theory to construct a hybrid Biot-Squirt flow modal based on which he performs the wavefield simulation. One limit of this model is that the fluid inside the compliant pore must be liquid; otherwise, the squirt flow model is no longer valid.

2.2.4. Mesoscopic Flow Models

The Biot-Gassmann and squirt flow models are mainly used for the single fluid saturated condition. For the multiple fluids saturated condition, the equivalent medium theories extended from Gassmann equations (i.e. BGW, BGH, and BGV) are commonly used. However, the multiple immiscible fluids inside the consolidated or low permeable porous rock are often in a patchy-saturation condition which may cause mesoscopic flow during the wave propagation (Ba et al., 2011; Cadoret et al., 1998; Carcione et al., 2003; Dutta and Odé, 1979; Gist, 1994; Johnson, 2001; Murphy III, 1984; Pride et al., 2004; Qi et al., 2014; Sun et al., 2015; Toms et al., 2006; White, 1975). The characteristic length of the mesoscopic flow is far larger than the typical pore size but still much smaller than the wavelength.

Compared to the single fluid saturation, the multiple fluid saturation has a much higher wave-induced pressure gradient across the fluids because of the compressibility difference between

the fluids. White (1975) first brings in the mesoscopic flow concept to solve the dispersion and attenuation problem in a water-air mix saturated sandstone. It considers a spherical air bubble in a periodically spatial arrangement to simulate the heterogeneous distribution of the fluids.

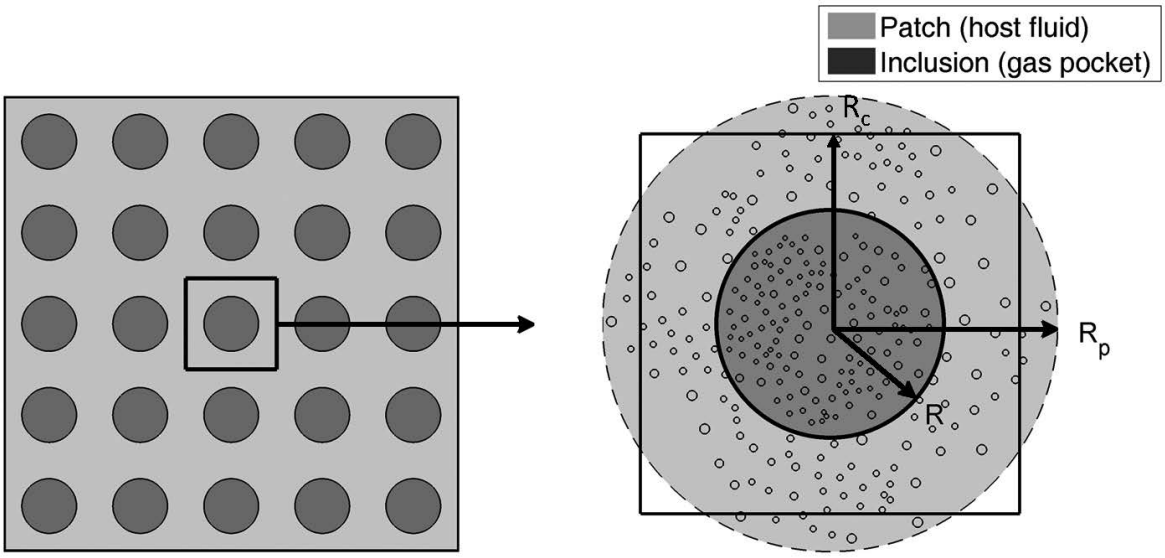

Figure 2. 6 The inclusion and patch geometry in the White model for partially saturated rock.

The original White model defines the pore space consists of a partial saturation cubic unit with a length of the side R_c and each such unit contains a spherical gas bubble with a radius R (Figure 2. 6). For the convenience of calculation, the cubic unit is simplified to concentric sphere structure with outer radius is R_p which represents the patch radius. It means that each cubic unit in the medium contains a sphere inclusion in the center. The cubic unit is treated as an outer sphere with the same volume. The ratio of $(R/R_p)^3$ gives saturation. It is noticeable that the max radius of the gas pocket/bubble is R_c which means the max gas saturation is $\pi/6$.

The bulk modulus of a mixture of the water-gas saturated rock in the White model is calculated by the pressure P^* and the corresponding volume changed V^*:

$$K^* = \frac{P^*}{V^*} = \frac{K_0}{1-K_0 W} \tag{2.42a}$$

$$\mathrm{W} = \frac{3R^2(R_1-R_2)(Q_2-Q_1)}{iR_p^3\omega(Z_1+Z_2)} \tag{2.42b}$$

The R and R_p are the radii of the concentric gas sphere and the liquid shell, respectively. K_0 is the bulk modulus of the mixture without the fluid flow. $R_1, R_2, Q_1, Q_2, Z_1, Z_2$ are coefficients associated with the petrophysical parameters, which can be found in the literature for the details

(Sun et al., 2015). The shear modulus is unchanged by the mix saturation in the White model. Take advantage of equation (2.42), and one can calculate the P wave velocity and attenuation.

Chapter 3. Wettability Effect on Wave Propagation in Saturated Porous Medium

This chapter is a published peer-reviewed journal paper in *The Journal of the Acoustical Society of America*:

Li, J. X., Rezaee, R., & Müller, T. M. (2020). Wettability effect on wave propagation in saturated porous medium. The Journal of the Acoustical Society of America, 147(2), 911-920.

3.1. Introduction

In dynamic poroelasticity, the relative fluid-solid motion induced by a passing wave has been extensively studied (Müller et al., 2010). However, most of the research on either macroscopic or microscopic level only considers the no-slip boundary, where the pore-scale flow velocity at the pore wall is zero. Hereafter we denote this as the no-slip boundary condition (or no-slip BC). For instance, in an attempt to account for the viscous boundary layer flow, Biot considered the velocity of the wave-excited flow (global flow) at the pore wall to be zero ($v_s = 0$) (Biot, 1956b). In general, however, the flow velocity at the solid boundary is not necessarily zero. Then a so-called slippage boundary condition ($v_s \neq 0$) characterized by a slip length is common in micro-fluid mechanics (Vinogradova and Belyaev, 2011). The slip length b is defined as an extrapolated distance relative to the pore wall, where the tangential fluid velocity component vanishes at the wall of a virtually enlarged pore (VEP) as shown in Figure 3. 1(Cottin-Bizonne et al., 2003; Ortiz-Young et al., 2013; Priezjev et al., 2005). The flow velocity at the solid boundary (interface of the real pore wall) is the slip velocity v_s.

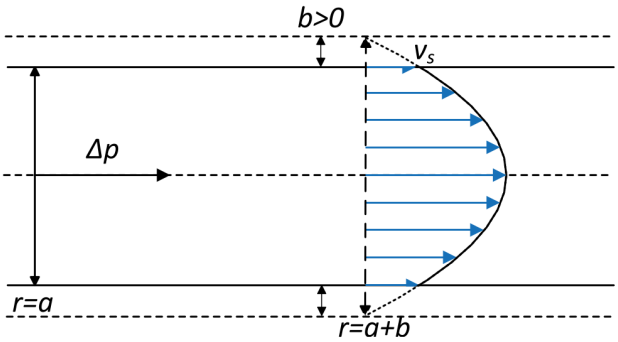

Figure 3. 1 The slip boundary condition (BC) with slip length b for oscillatory forced flow in a duct pore with radius r = a. The tangential velocity profile vanishes at the wall of a virtually enlarged pore (VEP) with radius r = a + b.

Literature has reported that the ratio of slip length to system size increase when the system size decrease. Generally, the proportion of slip length can reach 15% - 25% of the system size (pore size) in a nano-meter level system to 3.3%-3.8% of that in a millimetre level system (Lauga and Stone, 2003). Notably, the wettability or the degree of hydrophobicity of the flow channel can profoundly affect the degree of the flow slippage at the solid boundary. This has been proved in several experiments and molecular dynamics (MD) simulations (Barrat, 1999; Cottin-Bizonne et al., 2005; Huang et al., 2008; Ramos-Alvarado et al., 2016; Thompson and Robbins, 1990). These studies all point out that slippage will increase when the degree of wetting decreases (i.e. for increasing hydrophobicity).

From a MD simulation perspective, the increasing hydrophobicity leads to the decrease of the intermolecular potential energy between fluid and solid with a different fluid molecular organization near the solid, which causes the slippage (Cieplak et al., 2001; Lauga et al., 2007). When the contact angle, which quantifies the wettability, increase, the flow boundary condition can dramatically differ from the no-slip BC (Barrat, 1999). For instance, the hydrophobic surface gained by patterned nanoscale roughness significantly increases the slippage and reduces the friction of the flow at the wall of the boundary interface (Cottin-Bizonne et al., 2003).

Because of the complicated nature of the interaction during the interfacial flow, there is not a specific formula to quantify the slip length with its control factors. However, a quasi-universal relationship at a microscopic level between slip length and one of its most crucial control factors, the static contact angle, has been suggested by MD simulations (Huang et al., 2008),

$$b \propto (1 + \cos\theta_c)^{-2} \tag{3.1}$$

It relates the slip length b to the static contact angle of a liquid θ_c, i.e. where a liquid-vapor interface meets the solid surface. This relation is supported by laboratory observation (Ortiz-Young et al., 2013). Therefore, we take the term $(1 + \cos\theta_c)^{-2}$ is a kind of dimensionless slip length from which the relationship between slip length and wettability can be assessed.

In the small, middle and large contact angle limits, we have: $\lim_{\theta_c \to 0}(1 + \cos\theta_c)^{-2} = 0.25$, $\lim_{\theta_c \to 90}(1 + \cos\theta_c)^{-2} = 1$, and $\lim_{\theta_c \to 180}(1 + \cos\theta_c)^{-2} = +\infty$. Figure 3. 2 shows that the dimensionless slip length increases dramatically along with increasing contact angle in the

range of 40˚ - 140˚. Meanwhile, the other controlling factors of the slip length could also be related to the wettability or intermolecular energy. For instance, the surface roughness may induce the de-wetting or hydrophobic property which enhances the slippage (Lauga et al., 2007). In this chapter, we use the slip length as a proxy for the wettability given all the other control factors remaining the same.

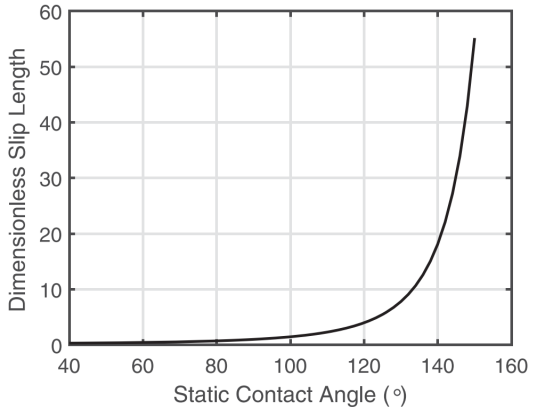

Figure 3. 2 The dimensionless slip length increases significantly during the transition of the flow surface from hydrophilic $\theta_c < 90°$ to hydrophobic $\theta_c > 90°$.

There are several models reported that account for the slip effect on the elastic wave in gas-saturated (Liu et al., 2018; Markov, 2007; Markov and Markov, 2018; Umnova et al., 2009) and in liquid-saturated porous media (Tsiklauri, 2002). The no-slip BC is violated if the characteristic size of pore or grain becomes comparable to the molecular mean free path, which approximates to the slip length for gas flow (Umnova et al., 2009). As a consequence for elastic waves in porous media, it is found that the slip BC leads to lower attenuation and higher phase velocity compared to the results of the no-slip BC (Liu et al., 2018; Markov and Markov, 2018).

The above pieces of evidence have revealed that the wettability expressed by the slip BC affects the wave dissipation, which may become substantial with escalating hydrophobicity. In this paper, we use a linear slip flow model with constant slip length to capture the wettability effect on wave propagation for a fully saturated isotropic porous medium. The slip length b is the only new parameter introduced in this study to account for the wettability effect. The structure of the paper is as follows. In section 3.2, the viscosity correction factor of the virtually enlarged pore (VEP) model with slip BC is derived. It leads to a frequency- and wettability (slip length)-dependent value for a given porous medium. In section 3.3 the dynamic permeability and tortuosity for the VEP model is worked out in analytical form and is compared with the high-

frequency Biot correction (Biot, 1956b). The low- and high-frequency limits of the results are discussed. In section 3.4, the phase velocities and attenuation factors are solved explicitly for the slip boundary VEP model. Moreover, the phase difference and amplitude ratio of the fluid and solid phases are analysed. Section 3.5 discusses the assumption of the model and its difference from the previous similar model. Last, section 3.6 summarizes the main findings.

3.2. Virtually Enlarged Pore (VEP) Model

3.2.1. The Velocity of the Oscillatory Forced Flow with Slip BC

Following Biot's analysis, we consider an oscillatory forced non-wetting fluid flow in a duct pore with radius a representing the characteristic pore size. The pressure gradient is in the axial direction and neglected in the direction normal to the boundary (Figure 3. 1). The displacement is assumed to only occur in the axial direction. Under sinusoidal loading $e^{\mathrm{i}\omega t}$, the flow velocity with respect to the solid wall is a function of the distance to the centre r and its expressions are developed by (Biot, 1956b) as

$$v = CJ_0(R) + \frac{X}{\mathrm{i}\omega}, \tag{3.2a}$$

$$R = \mathrm{i}r\sqrt{\frac{i\omega S}{D_\nu}}. \tag{3.2b}$$

where C is arbitrary constant, $J_0()$ is zero-order Bessel function, X is the body force $\rho_\mathrm{f} X = -\frac{\partial P}{\partial x} - \rho_\mathrm{f}\ddot{u}$, $\frac{\partial P}{\partial x}$ is the pressure gradient, $\ddot{u}$ is the accelerating term of solid, i is the imaginary unit for the complex number, ω is the angular frequency of the incident wave, r is the distance to the central axis. The square root part in equation (3.2b) is the diffusion wave number of the viscous wave, $k = \sqrt{\frac{\mathrm{i}\omega S}{D_\nu}}$ (Müller and Sahay, 2011a; Müller and Sahay, 2011b; Müller and Sahay, 2011c), S is the sinuosity to represent the general condition of the canted pore, which is not parallel to the direction of the pressure gradient (Biot, 1956b), $D_\nu = \mu_\mathrm{f}/\rho_\mathrm{f}$ is the kinematic viscosity, μ_f and ρ_f are the dynamic viscosity and density of the fluid, respectively.

Different from the no-slip BC, where the flow velocity becomes zero at the pore wall, the slip BC is characterized by the slip length b with $b > 0$. It has non-zero flow velocity at the pore wall ($v_s > 0$) and only at the mirror side of the pore wall the flow velocity extension line reaches zero,

$$v|_{r=a+b} = 0. \tag{3.3}$$

We notice that this zero-velocity only occurs when r = a + b, which is not the boundary in a real pore but in a virtually enlarged pore (VEP) as shown in Figure 3.1. For the moment, we assume a linear slippage with constant slip length *b* (Vinogradova, 1995). From equation(3.2a) and (3.2b) with the BC equation (3.3), we obtain the constant C

$$C = \frac{-X/\mathrm{i}\omega}{J_0(A+B)} \tag{3.4}$$

Therefore, the flow velocity in the VEP slip boundary model is obtained as,

$$v = \frac{X}{i\omega}\left[1 - \frac{J_0(\mathrm{R})}{J_0(A+B)}\right] \tag{3.5a}$$

$$A = ia\sqrt{\frac{i\omega\xi}{\beta}} \tag{3.5b}$$

$$B = i\mathrm{b}\sqrt{\frac{i\omega\xi}{\beta}} \tag{3.5c}$$

The HF Biot model adopts the no-slip boundary condition. It represents the condition for which the fluid is wetting the porous medium (Biot, 1956b; Murphy III et al., 1984). In contrast, the VEP model describes the condition of the non-wetting fluid saturated hydrophobic porous medium, where flow slippage occurs at the pore wall. This slippage is embodied in equation(5.5c). Essentially, it adds a viscous wave in the virtually extended boundary layer to the already existing viscous wave in the real pore channel.

The flow velocity field can be decomposed into two parts: one is the potential flow dominated by the pressure gradient, the other is the viscous flow in the boundary layer dominated by the kinematic viscosity and the pore surface properties (Johnson et al., 1987; Müller and Sahay, 2011c). The latter is a dimensionless item which can be deemed as normalized flow velocity which accounts for the dissipation.

For a duct pore with 10 μm radius saturated with water, the normalized velocities of the oscillatory forced flow in VEP model ($b = a/20$) is frequency dependent and plotted in Figure 3. 3a, which is based on equation (5.5a) regardless of the pressure gradient term $X/\mathrm{i}\omega$. At any given frequency, the velocity profile on the cross section of the pore is axisymmetric (Figure 3. 3b)

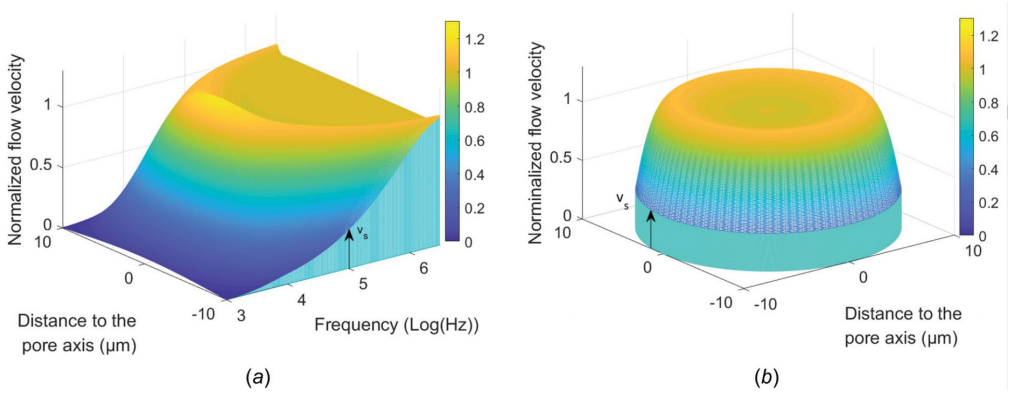

Figure 3. 3 Normalized velocity profile of flow in a capillary duct pore with 10 μm radius in VEP model at a frequency range of: (a) 1k Hz – 3M Hz, and (b)100k Hz.

Meanwhile, the slip velocity v_s increases with the increasing frequency. The velocity profile changes from parabolic shape to saddle shape during the transition from low frequency to high frequency. This feature is related to the crossover from a viscous dominated regime at low frequency to the inertial dominated regime at high frequency. At high frequency, inertia prevents viscous fluid flow through the pore (Müller and Sahay, 2011c) but the fluid close to the solid interface (viscous boundary layer) is influenced by the drag force of the solid motion (Pride et al., 1993). It, therefore, renders higher velocity in the vicinity of the pore wall than that of the bulk fluid (potential flow field), which is under the control of inertial acceleration (Charlaix et al., 1988). We will show in section 3.4 that the out-of-phase motion between the fluid and solid becomes intensified in the inertial dominated high-frequency range and that it deviates from the parabolic velocity profile.

The average pore-scale flow velocity $\bar{v}$ can be calculated from the equal transient volumetric flow rate principle,

$$\int_0^a v \cdot 2\pi r dr = \pi a^2 \bar{v} \ . \tag{3.6}$$

Substituting equation(3.5a) into (3.6), we obtain the average flow velocity for the VEP model

$$\bar{v} = \frac{2}{a^2}\int_0^a v \cdot r dr = \frac{X}{i\omega}\left(1 - \frac{2J_1(\mathrm{A})}{AJ_0(A+B)}\right) \tag{3.7}$$

In the derivation of equation (3.7), the following identity for the Bessel function has been used

$$\int x J_0(x)\, dx = x J_1(x) \tag{8}$$

$J_n(x)$ is Bessel function of n order with $n = 0, 1$.

3.2.2. Viscosity Correction Factor in VEP Model

From equation(3.5a), we obtain the viscous friction stress of the flow in the VEP model,

$$\tau = -\mu_{\mathrm{f}} \left[\frac{dv}{dr}\right]_{r=a}, \tag{3.9}$$

and the corresponding total friction force,

$$h_{VEP} = 2\pi a\tau = -\left(\frac{X}{i\omega}\right)\frac{2\pi\mu_{\mathrm{f}} A J_1(\mathrm{A})}{J_0(A+B)} \quad , \tag{3.10}$$

For comparison, the total friction force and the average flow velocity of the HF Biot theory are,

$$h_{Biot} = -\left(\frac{X}{i\omega}\right)\frac{2\pi\mu_{\mathrm{f}} A J_1(\mathrm{A})}{J_0(A)} \ , \tag{3.11}$$

$$\bar{v}_{Biot} = \frac{X}{i\omega}\left(1 - \frac{2J_1(\mathrm{A})}{AJ_0(A)}\right). \tag{3.12}$$

The frequency dependent viscosity correction factor $F_B(\omega)$, which quantifies the deviation from Poiseuille flow, is derived from the ratio of the total friction and the average flow velocity (Biot, 1956b),

$$\frac{f_B}{\bar{v}_B} = 8\pi\mu_{\mathrm{f}} F_B(\omega) \quad . \tag{3.13}$$

Now we can use equations (3.7), (3.10), (3.11) and (3.12) to calculate the ratio of the average flow velocities and the ratio of the friction force of the VEP model and the Biot model. It yields to

$$\theta_v = \frac{\bar{v}}{\bar{v}_{Biot}} = \frac{1-\frac{2J_1(\mathrm{A})}{AJ_0(A+B)}}{1-\frac{2J_1(\mathrm{A})}{AJ_0(A)}} \ , \tag{3.14}$$

$$\theta_f = \frac{h_{VEP}}{h_{Biot}} = \frac{J_0(A)}{J_0(A+B)} \quad . \tag{3.15}$$

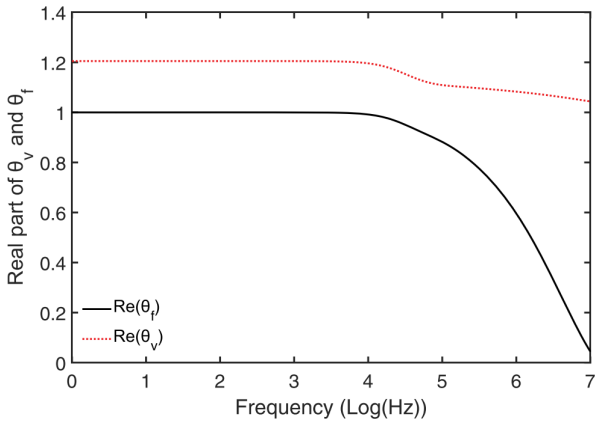

Figure 3. 4 The ratio of the average velocities and ratio of the friction force (real part) for VEP model and HF Biot model in the frequency domain for a 10 μm duct pore saturated by water.

Figure 3. 4 shows that the VEP model leads to higher average flow velocity and notably lower friction force than the HF Biot model, especially at the high-frequency range.

Substituting equation (3.14) and (3.15) into (3.13), we derive the viscosity correction factor for the VEP model,

$$F(\omega) = \frac{\theta_f}{\theta_v} F_B(\omega) \,. \tag{3.16}$$

We notice that at low-frequency limit $\lim_{\omega \to 0} F_B(\omega) \to 1$, and $\lim_{\omega \to 0} F(\omega) \to \frac{\theta_f}{\theta_v} < 1$, which agrees with the higher average flow velocity (flow rate) observation in the static flow with slip boundary than the results with no-slip boundary (Cheng and Giordano, 2002; Lauga and Stone, 2003). When the slip length $b = 0$, there are $\lim_{\omega \to 0} F(\omega) \to \frac{\theta_f}{\theta_v} = 1$ and the VEP model reduce to the HF Biot model, as expected.

3.3. Dynamic Permeability and Tortuosity of the VEP Model

3.3.1. Relationship Between the Viscosity Correction Factor and the Dynamic Permeability and Tortuosity

The attenuation of the mechanical wave in a porous medium is mainly caused by the viscous dissipation which is due to the relative motion between the pore-filling fluid and the solid frame (Biot, 1956b). The viscosity adjusted by the correction factor becomes the frequency dependent

dynamic viscosity. Alternatively, this is expressed in terms of dynamic permeability and tortuosity (Berryman, 2003; Johnson et al., 1987).

The dynamic permeability and tortuosity for HF Biot model under harmonic loading $e^{\mathrm{i}\omega t}$ (Hu and Wang, 2001) are expressed through,

$$\kappa_B(\omega) = \frac{\kappa_0}{F_B(\omega)+\frac{\mathrm{i}T_\infty \kappa_0 \rho_\mathrm{f}\omega}{\mu_\mathrm{f}\emptyset}} \tag{3.17}$$

$$T_B(\omega) = T_\infty \ - \frac{\mathrm{i}\mu_\mathrm{f}\phi}{\omega\kappa_0\rho_\mathrm{f}}F_B(\omega) \tag{3.18}$$

where κ_0 is the static permeability, T_∞ is the static tortuosity and ϕ is the porosity.

The corresponding dynamic permeability and tortuosity for VEP model follow the similar format as,

$$\kappa(\omega) = \frac{\kappa_0}{F(\omega)+\frac{\mathrm{i}T_\infty \kappa_0 \rho_\mathrm{f}\omega}{\mu_\mathrm{f}\emptyset}} \tag{3.19}$$

$$T(\omega) = T_\infty \ - \frac{\mathrm{i}\mu_\mathrm{f}\phi}{\omega\kappa_0\rho_\mathrm{f}}F(\omega) \tag{3.20}$$

Equations (3.16), (3.19), (3.20) with the incorporation of the VEP model are the core results of this paper.

3.3.2. Properties of the Dynamic Permeability and Tortuosity in the VEP Model

By analysing equation (3.17) - (3.20), we find in the high-frequency limit

$$\lim_{\omega\to\infty} \kappa(\omega) = \lim_{\omega\to\infty} \kappa_B(\omega) \to 0 \tag{3.21}$$

$$\lim_{\omega\to\infty} T(\omega) = \lim_{\omega\to\infty} T_B(\omega) = T_\infty \tag{3.22}$$

Moreover, at low-frequency limit,

$$\lim_{\omega\to 0} \kappa_B(\omega) = \kappa_0 \quad , \tag{3.23}$$

$$\lim_{\omega\to 0} \kappa(\omega) = \frac{\theta_v}{\theta_f}\kappa_0 > \kappa_0 \quad , \tag{3.24}$$

$$\lim_{\omega \to 0} Im[T_B(\omega)] = -\frac{\mathrm{i}\mu_f \phi}{\kappa_0 \omega \rho_f} \ , \tag{3.25}$$

$$\lim_{\omega \to 0} Im[T(\omega)] = -\frac{\theta_f}{\theta_v} \frac{i\mu_f \phi}{\kappa_0 \omega \rho_f} \tag{3.26}$$

It is worth noticing that only the imaginary part of dynamic tortuosity reaches a concise expression in the low-frequency limit (Johnson et al., 1987). In the fraction part of the dynamic tortuosity as equation (3.18) and (3.20), the complex viscosity correction factors $F_B(\omega)$and $F(\omega)$ cancel out the change of frequency dependent denominator at low frequencies rendering the real part of the fraction is none-zero.

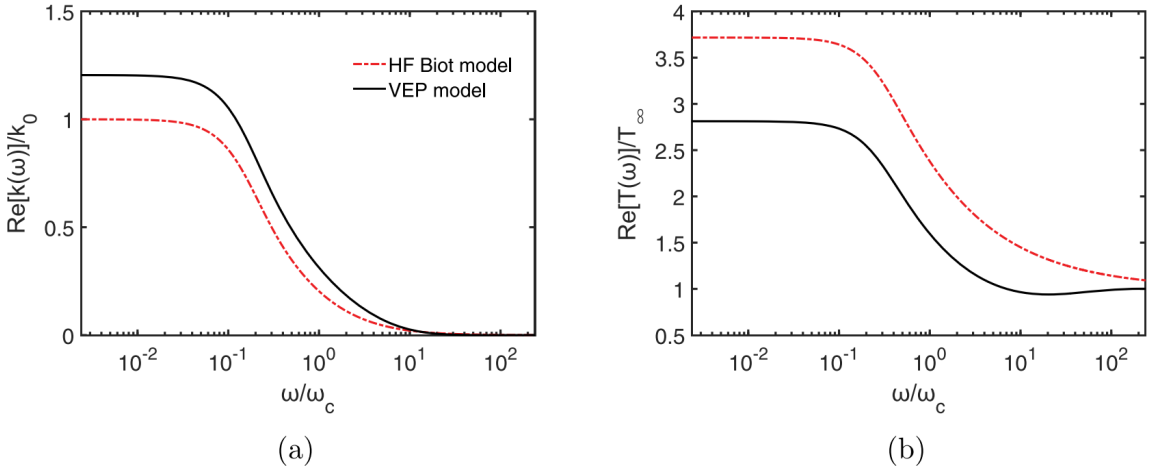

Figure 3. 5 Comparison of dynamic permeability (a) and tortuosity (b) (real parts) of HF Biot and VEP (b = a/20) models for a porous medium with 10 μm average pore radius.

One of the remarkable features of $\kappa(\omega)$ is that, in the low frequency limit, it reaches a value higher than the static permeability, which represents the case of the wetting fluid flow (Figure 3. 5).

This coincides with the literature reports wherein slip-corrected permeability is higher than the intrinsic permeability without slippage for the static flow (Hosseini and Tafreshi, 2010; Javadpour et al., 2015).

The dynamic permeability and tortuosity are scaled by static parameters ($\kappa_0, \mathcal{T}_\infty$) and the Biot characteristic frequency $\omega_B = \mu_f \phi / T_\infty \kappa_0 \rho_f$ (Charlaix et al., 1988; Sheng and Zhou, 1988; Smeulders et al., 1992). They are also connected via (Johnson et al., 1987; Müller and Sahay, 2011c),

$$\frac{T(\omega)}{T_\infty} = \frac{\omega_B}{i\omega} \cdot \frac{\kappa_0}{\kappa(\omega)} \tag{3.27}$$

3.4. Implementation of VEP Model

The VEP model can be incorporated into the Biot theory (Biot, 1956a) by either using the viscous correction factor to correct the viscosity or using the dynamic tortuosity to replace the static tortuosity. The two approaches are equivalent. Here we use the equations of motion with wettability dependent dynamic tortuosity to solve for the phase velocities, attenuation, and amplitude ratio and phase difference of fluid and solid phases analytically. A plane wave analysis is given in Appendix A. We use equation (3.1) to arbitrarily select two slip lengths $b = a/80$ and $b = a/20$ to represent the neutral wetting and strong non-wetting conditions of the fluid saturated rock which correspond to the contact angle of 90˚and 120˚, respectively. HF Biot model with the no-slip boundary is used to represent the wetting condition for the fluid to the rock matrix frame with a contact angle of 40˚. Meanwhile, Gassmann velocities are adopted as a benchmark for the phase velocities in the low frequency range. The parameters in **Error! Reference source not found.** are used in the numerical example.

Table 3. 1 Parameters of water-saturated sandstone.

Grain	Bulk modulus, K_s	50 GPa
	Density, ρ_s	2650 kg/m^3
Matrix	Porosity, ϕ	0.2
	Bulk modulus, K_d	18 GPa
	Shear modulus, μ_d	12 GPa
	Permeability, κ_0	200mD
	Tortuosity, T_∞	2.76
	Average pore radius, a	10 μm
	Sinuosity,S	1.49
Brine	Bulk modulus, K_f	2.25 GPa
	Density, ρ_f	1040 kg/m^3
	Viscosity, μ_f	1 cP
Remark: 1 cP =10^{-3} Pa·s; 1mD ≈ 10^{-15} m^2		

3.4.1. Phase Velocities and Attenuation

The Biot theory predicts two kinds of compressional (P-) wave (denoted as p+ and p-) and one shear (S-) wave (Biot, 1956a), which remain unchanged when the slip length dependent viscosity correction factor or dynamic tortuosity is applied. An explicit expression for the phase velocities and the attenuation factors is given in equation (A3) and (A4). The velocities of fast P (p+) and S-wave under various wettability conditions coincide with the predictions of the Gassmann model in the low-frequency range. In the high-frequency range, the velocities of all three kinds of waves increase when the contact angle (slip length) and hydrophobicity increase. For instance, **Error! Reference source not found.** shows the phase velocity and attenuation (inverse quality factor) for the fast and slow P-waves. We observe that the step transition of phase velocity is sharper and velocity dispersion is more pronounced for the non-wetting condition (large contact angle) than that of the wetting condition (small contact angle) which qualitatively agree with the experimental results (Li et al., 2001; Moerig et al., 1996). The velocities for each wave mode converge to the same value regardless of the wettability in an upper high frequency bound.

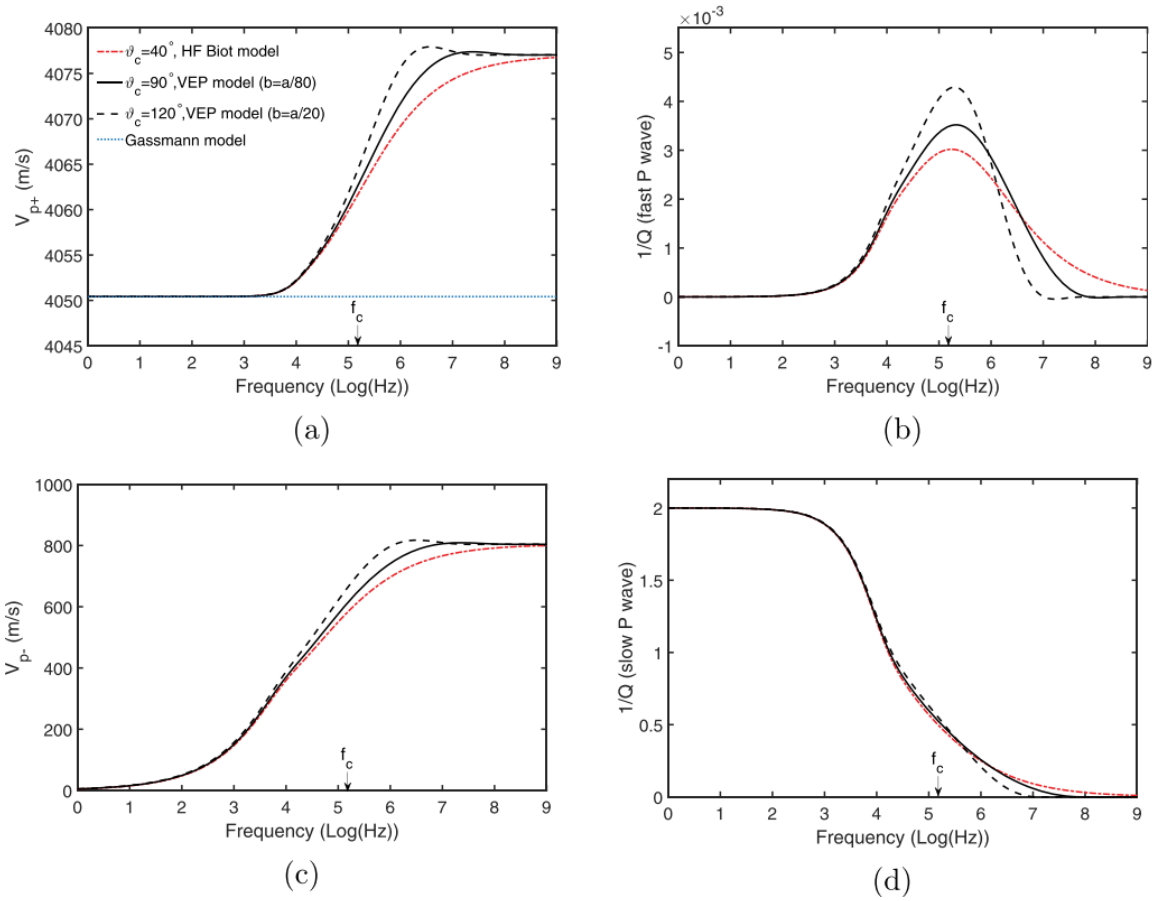

Figure 3. 6 Fast P wave phase velocity (a) and attenuation (b), and Slow P wave phase velocity (c) and attenuation (d) under different wettability conditions. The arrow indicates the Biot characteristic frequency $f_c = \frac{\omega_B}{2\pi}$.

As far as attenuation is concerned, the slow P-wave is less influenced by wettability. Since the friction reduction effect from the interfacial slip is weak at low frequencies (Figure 3. 4), it does not affect much the attenuation of slow P wave in this frequency range. The effect only becomes strong at high frequencies; however, the attenuation of the slow P-wave becomes negligibly small. This may explain the minimal impact of the wettability on the attenuation of the slow P-wave. For the fast P-wave and S-wave, the bulging attenuation curves become more prominent and better "localized" in the frequency domain when the contact angle increases. The attenuation peak also tends to a higher value when the non-wetting degree increases.

3.4.2. Amplitude Ratio and Phase Difference of Fluid and Solid Phases

The motions of the fluid and solid are in phase for fast P-wave and S-wave, while there is an opposite-phase motion for the slow P-wave for which the amplitude of the fluid is higher than that of the solid (Biot, 1956a). The amplitude ratios and the phase difference between the fluid

and solid phases are calculated with equation (A13) - (A16) in Appendix A. These properties are examined for the two kinds of P-waves in the following discussion, whereas S-wave has very similar behaviours as the fast P-wave in the amplitude ratio and the phase difference between the fluid and solid phases.

The amplitude ratio between the fluid and solid phases g_j (j = $p+$, $p-$) are plotted in the frequency domain in Figure 3. 7. We observe that for the slow P-wave the amplitude of the fluid is much larger than that of the solid phase. This indicates that the energy of the slow P-wave is mainly transmitted in the fluid phase that has been enhanced in non-wetting condition (large contact angle) at high frequencies. For fast P- and S-waves, we observe that the fluid and solid keep the same amplitude at low frequencies. However, at high frequencies of fast P and S-waves, the amplitude of fluid becomes lower than that of solid which is exaggerated by increasing hydrophobicity and contact angle.

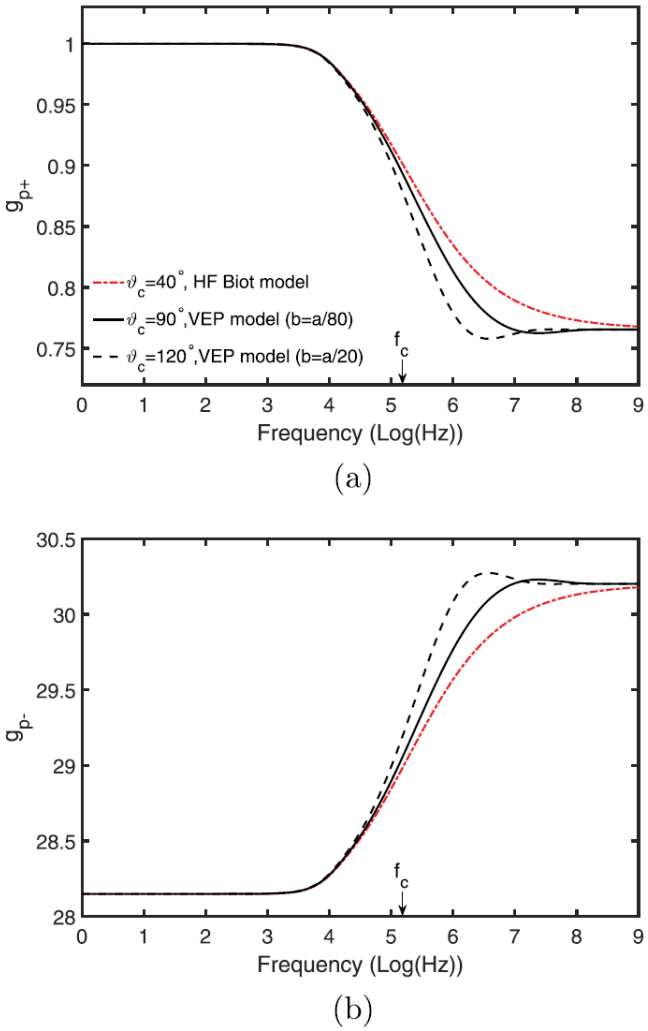

Figure 3. 7 Amplitude ratio of fluid and solid phases under different wettability conditions for (a) fast P wave, (b) slow P wave in the frequency domain. The arrow indicates the Biot characteristic frequency $f_c = \frac{\omega_B}{2\pi}$.

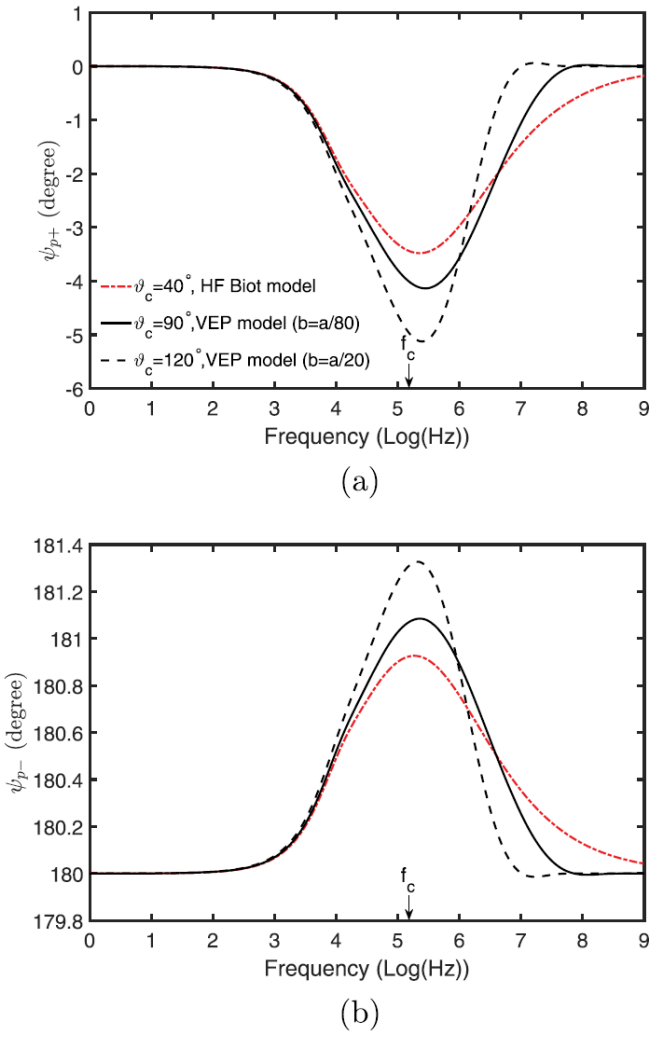

Figure 3. 8 Phase difference between fluid and solid phases under different wettability conditions for (a) fast P wave, and (b) slow P wave frequency domain. The arrow indicates the Biot characteristic frequency $f_c = \frac{\omega_B}{2\pi}$.

The phase difference ψ_j(j = p+, p-) is shown in Figure 3. 8. The phase difference of fluid and solid starts to deviate from zero with increasing frequency of the fast P-wave, which implies a slight out-of-phase motion between the two phases. The S-wave behaves similarly to the fast P-wave. For the slow P-wave, the phase difference also deviates from 180 deg at high

frequencies. The non-wetting condition with a larger contact angle renders a larger peak deviation for all kinds of waves. This indicates that the hydrophobicity enhances the opposite motion between fluid and solid for all three kinds of waves at high frequencies. For the large contact angle case, through the slip BC, the inertial motion of a fluid parcel is facilitated and the transaction zones of phase difference are sharper or better "localized" in the frequency domain. This means that the coupling between fluid and solid motion in non-wetting condition becomes weaker and therefore there is a tendency to promote out-of-phase motion. The negative values of the phase difference in fast P- and S-wave indicate the motion of the fluid phase is lagging behind that of the solid phase.

3.5. Discussion

In the Navier slip (Navier, 1823) and the Vinogradova slip models (Vinogradova, 1995; Vinogradova, 1998), the slip length is a constant, which only depends on the properties of the pore surface and the fluid.

This assumption is supported by various experimental results (Bonaccurso et al., 2002; Cottin-Bizonne et al., 2002; Joseph and Tabeling, 2005; Leger, 2002; Pit et al., 2000; Vinogradova and Yakubov, 2003). Following these results, we use the constant slip length assumption in the VEP model. It is worth mentioning that other studies suggest a shear rate dependent slip model (Spikes and Granick, 2003; Thompson and Troian, 1997). The effect of shear rate on the slip length is still a controversial element in the debate on the BC (Neto et al., 2005). Thompson and Troian (1997) suggest that the constant slip length is only valid at a low shear rate before it reaches the critical shear rate, while Spikes and Granick (2003) claim that the slip may only occur with a finite slip length at the shear rates above the critical shear rate. Even though the slip length may become non-linear at the boundary, we believe that an effective, constant slip length is a reasonable choice to represent the overall slippage for the non-wetting saturated case.

As mentioned in section 3.1, there have been several studies discussing the slip BC effect on wave propagation in a porous medium. Most notably, Tsiklauri (2002) suggests a phenomenological model by extending the HF Biot model. While the construction of Tsiklauri (2002) is similar to the VEP model suggested here, it has to introduce three parameters to describe the fluid slippage. In contrast, the VEP model only introduces one, physically meaningful parameter, the slip length b, to characterize the slippage effect.

There is experimental evidence that the bulk modulus of a core sample saturated by either strongly wetting or weakly wetting fluid does match the Gassmann-Biot theory prediction; however, the shear modulus of brine-saturated (i.e. a weakly wetting fluid) synthetic porous material is smaller than the Biot-Gassmann prediction (Wang et al., 2015). We suspect that two competing mechanisms contribute to these observations. On the one hand, a change in the surface energy which might enhance or reduce the stiffness of the grain contacts is independent of frequency (Murphy III et al., 1984). As a result, the drained frame moduli also change. However, the related theory itself is incomplete and also beyond the scope of this paper. On the other hand, the VEP model is based on the hydrodynamic analysis of saturated pore under excitation of a compressional wave, in which the bulk modulus is affected by the wettability/slippage. Whether the shear modulus is affected is still unknown. Thus, the bulk modulus may increase a little bit owing to the slippage resulting from weakly wetting condition, so as to compensate the decrease from the surface energy change.

3.6. Conclusion

We use the slip length to characterize the wettability of a fluid saturated porous medium. The wettability dependent virtually enlarged pore (VEP) model with slip BC is developed. We demonstrate that the VEP and HF Biot models can be converted to similar formats with a viscosity correction factor, dynamic permeability, and dynamic tortuosity. However, only the VEP model takes account of the wettability factor in the calculation. Wettability effect on the phase velocities, attenuation, the amplitude ratio of fluid and solid and their phase difference are analysed. The VEP model predicts higher phase velocities and attenuation peaks for hydrophobic fully saturated porous media in high-frequency range than the corresponding results of the hydrophilic ones. Meanwhile, the out-of-phase motion of fluid and solid is promoted in the non-wetting condition.

Chapter 4. Elastic Waves in Porous Media Saturated with Non-wetting Fluid

This chapter is a published peer-reviewed journal paper in *The APPEA Journal:*

Li, J. X., Rezaee, R., Müller, T. M., & Sarmadivaleh, M. (2020). Elastic waves in porous media saturated with non-wetting fluid. The APPEA Journal, 60(1), 315-325.

4.1. Introduction

Elastic wave propagation in porous media containing a fluid has been attracting attention not only because of its scientific value in the study of underground aquifers (Lin et al., 2004; Wang and Hsu, 2009) but because of its importance in geophysics (Nolet, 2012; Poletto and Miranda, 2004; Romanowicz, 2017) and wave motion enhanced oil recovery (Huh, 2006; Jeong and Kallivokas, 2017; Jeong et al., 2015; Kouznetsov et al., 1998) for the oil and gas industry.

Most of the poroelasticity theories either do not consider the fluid-solid coupling effect or only assume a wetting condition where the fluids are all wetting to the solid frame. For example, the Gassmann equations only considers the compressibility of the solid and fluid, not their relative motion. The Biot theory considers the relative fluid-solid motion but assumes that the solid frame is wetted by default (Biot, 1956a; Murphy III et al., 1984). However, the fluid bearing reservoir of sedimentary rocks can be modelled as either a hydrophilic (water-wetting) or hydrophobic (hydrocarbon-wetting) porous media, depending on the wettability of the rock matrix. Wettability of the rock matrix is a key parameter that affects not only the capillary pressure, and therefore, the mechanical properties (Feng et al., 2019; Lu et al., 2019; Qi, 2015; Qi et al., 2014) but also the hydrodynamic behaviour of the fluid (Barrat, 1999; Cottin-Bizonne et al., 2005; Huang et al., 2008; Ortiz-Young et al., 2013; Ramos-Alvarado et al., 2016).

The hydrodynamic properties of the wetting and non-wetting fluid in the same porous medium can be very different so that the frictional dissipation and the flow velocity are largely different from each other. The most obvious hydrodynamic property difference is that the pore-scale flow velocity of the wetting fluid becomes zero at the pore wall (Figure 4. 1a), while the non-wetting fluid, to which the pore surface is hydrophobic, tends to slip on the solid surface. This non-zero flow velocity at the solid surface is the so-called 'slip velocity' v_s (Figure 4. 1b) (Barrat, 1999; Cottin-Bizonne et al., 2005; Huang et al., 2008; Ortiz-Young et al., 2013; Ramos-Alvarado et al., 2016). The former hydrodynamic condition corresponds to the slip boundary condition (BC), while the latter condition corresponds to the non-slip BC. The slippage of the non-wetting fluid flow is quantified by the slip length b, which is defined as the

distance between the fluid-solid interfaces and the virtual no-slip plane, where the interpolated flow velocity profile vanishes (Figure 4. 1b).

There is evidence that wettability is one of the most critical factors affecting the slip length. For instance, Huang et al. (2008) conclude that the slip length b is proportional to the static contact angle θ_c in the vapour, which is an indicator of the wettability

$$b \propto (1 + cos\theta_c)^{-2}. \tag{4.1}$$

This relationship is further supported by experimental findings (Ortiz-Young et al., 2013). Therefore, we use slip length as a proxy for wettability.

Another model of slip BC links the apparent slip (AS) effect to the decrease in the viscosity of the fluid inside the viscous boundary layer, with a thickness equal to the viscous skin depth δ near the hydrophobic surface (Figure 4. 1c) (Lauga et al., 2007; Vinogradova, 1995). The slip length b is

$$b = \delta\left(\frac{\mu_f}{\mu_f^{slip}} - 1\right), \tag{4.2}$$

where μ_f^{slip} is the average viscosity of the fluid within the viscous skin depth δ and μ_f is the viscosity of the bulk fluid.

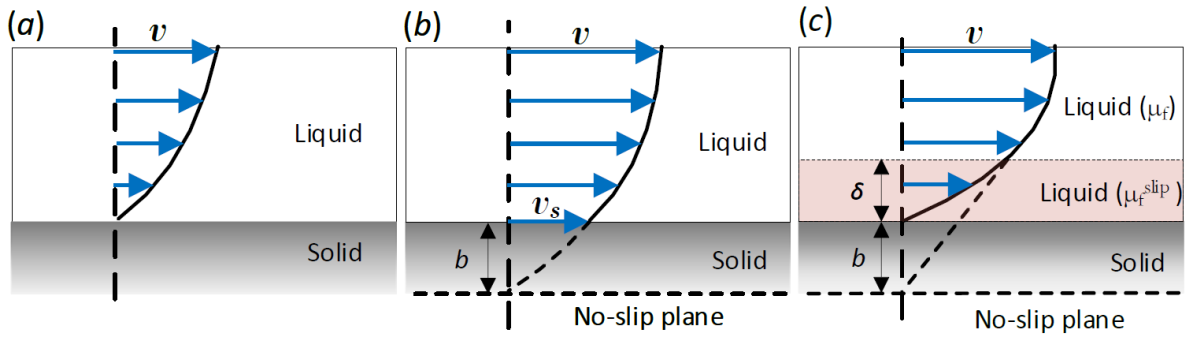

Figure 4. 1 (a) No-slip BC; (b) slip BC with slip velocity v_s and slip length b in a virtually enlarged pore wall; (c) slip BC with slip length b and smaller apparent viscosity μ_f^{slip} inside the viscous skin depth δ than the viscosity of the bulk fluid μ_f.

When b $\rightarrow$ 0, $\mu_f^{slip} \rightarrow \mu_f$ corresponds to the conventional no-slip BC; when b $\rightarrow\infty$, $\mu_f^{slip} \rightarrow \mu_f$ corresponds to ideal fluid flow, wherein complete slippage occurs. Previous studies

demonstrate that the slippage originates from a low fluid molecular density organisation near the hydrophobic surface, owing to the low intermolecular potential between the fluid and the solid (Barrat, 1999; de Gennes, 2002; Granick et al., 2003). This low fluid molecular density organisation is only constructed by several molecular layers, and thus, does not affect the mass density at the pore-scale but reduces the apparent viscosity of the non-wetting fluid.

Such wettability dependent molecular density has been studied by molecular dynamic (MD) simulations for argon liquid flow in a nanochannel (Cao et al., 2006) with the result shown in Figure 4. 2. We can see that the wetting ability represented by the static contact angle θ mainly affects the organisation of the liquid molecules near the solid boundary at r = ± 4.5σ, while the organisation of the molecules in the middle of the channel is less affected. σ = 3.405 × 10–10m is the characteristic length for the argon molecule in the MD simulation.

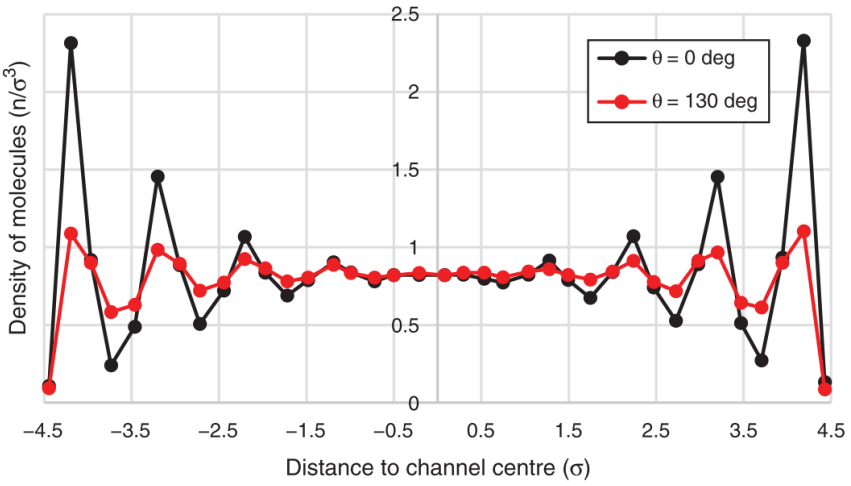

Figure 4. 2 The molecular density distribution in a nanochannel by MD simulation. Courtesy of Cao et al. (2006).

Because of the reduced apparent viscosity of the non-wetting fluid, the viscous dissipation of the wave energy is supposed to decrease, and the phase velocities should also be affected. The dynamic permeability and tortuosity, initially introduced by Johnson et al. (1987), are functions of the viscosity and vary according to the wetting condition between the fluid and the solid frame. In this paper, we incorporate the wettability (slip length) dependent apparent viscosity into the Biot model to examine the slip effect as a proxy of the wettability on the phase velocities, attenuation, and tortuosity.

4.2. Theory of Apparent Slippage and Effective Viscosity

As a wave passes through a saturated porous medium, wave-induced flow is generated at various scales (Müller and Gurevich, 2005). At pore-scale, the flow field can be decomposed into the viscous flow within the viscous skin depth and the potential flow in the rest space of the pores (Johnson et al., 1987; Landau and Lifshitz, 1987; Lighthill and Lighthill, 2001). For a porous medium saturated by a fluid of which density is ρ_{f} and viscosity is μ_{f}, the viscous dissipation, and therefore wave attenuation, is only caused by the viscous flow constrained within the viscous boundary layer with the viscous skin depth

$$\delta(\omega) = \sqrt{\frac{2\mu_{\mathrm{f}}}{\rho_{\mathrm{f}}\omega}} \quad , \tag{4.3}$$

which becomes much smaller than the pore size at high frequencies. The bulk fluid outside of the viscous skin depth is governed by the potential flow for which the flow pattern is identical to that for an ideal fluid and independent of the viscosity (Johnson et al., 1987; Müller and Sahay, 2011c). This means the viscosity of the bulk fluid is of less importance for the energy dissipation and the contribution to the average flow velocity.

Therefore, to account for the wettability/slippage effect on the wave motion, we replace the viscosity μ_{f} by the average viscosity inside the viscous skin depth μ_{f}^{slip},

$$\mu_{\mathrm{f}}^{slip}(\omega, b) = \frac{\mu_{\mathrm{f}}}{1+\frac{b}{\delta}} \ , \tag{4.4}$$

which can be derived from equation (4.2). We denote it as the effective viscosity that should be used for the calculation of the phase velocities and attenuations.

μ_{f}^{slip} is a function of slip length b, the viscosity of the bulk fluid μ_{f}, fluid density ρ_{f} and angular frequency ω. It is the same value as the normal viscosity at the low-frequency limit and decreases as frequency increases. When the slip length vanishes ($b \to 0$), the effective viscosity is identical to the normal viscosity μ_{f} relevant to the no-slip condition,

$$\mu_{\mathrm{f}}^{slip}|_{b\to 0} = \mu_{\mathrm{f}}. \tag{4.5}$$

It is convenient to normalise the effective viscosity μ_{f}^{slip} by the normal viscosity μ_{f}

$$\frac{\mu_{\mathrm{f}}^{slip}}{\mu_{\mathrm{f}}} = \frac{1}{1+\frac{b}{\delta}} . \tag{4.6}$$

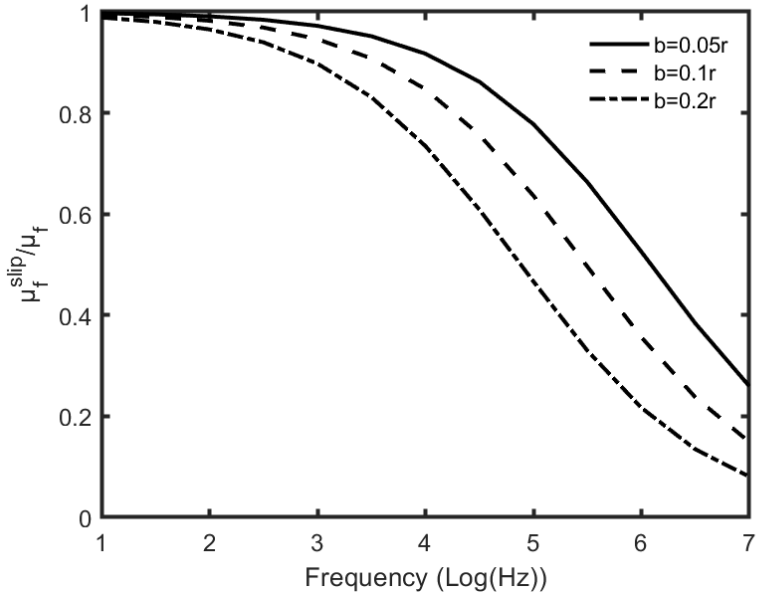

Figure 4. 3 The normalised effective viscosity under different slip lengths for brine in frequency spectral. Three slip lengths are a fraction of a typical pore size of sandstone r = 10 μm. Parameters in Table 4.1 are used.

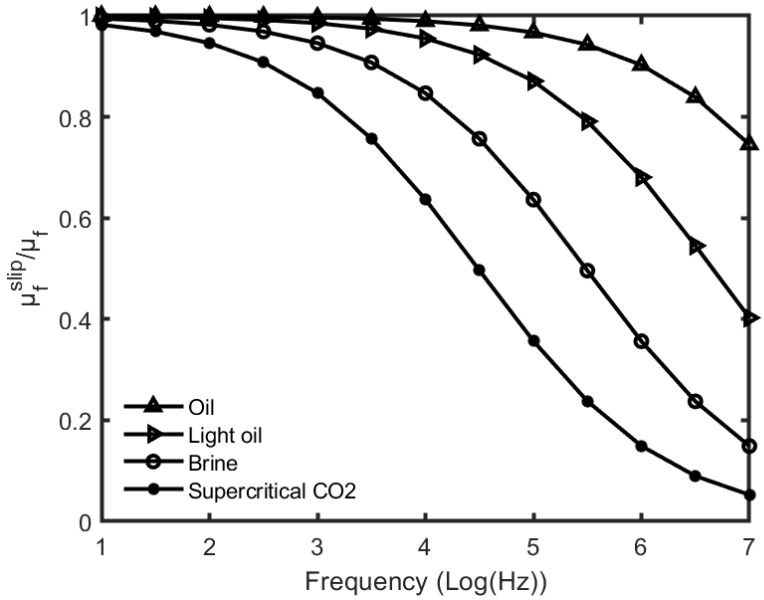

Figure 4. 4 Normalised effective viscosity of four different fluids in frequency spectral. The slip length b = 0.1r is a fraction of a typical pore size of sandstone r = 10 μm. Parameters in Table 4.1 are used.

The effective viscosity is a function of multiple parameters, where $\mu_{\mathrm{f}}^{slip} = f(\omega, b, \mu_{\mathrm{f}}, \rho_{\mathrm{f}})$. To examine the effects of these parameters on effective viscosity, we check the normalised effective viscosities of four types of typical fluids that commonly appear in an oil reservoir (Figure 4. 3 and Figure 4. 4). The parameters of the fluids are summarised in Table 4. 1.

Figure 4. 3 demonstrates that the effective viscosity decreases when the frequency or slip length (or hydrophobicity) increases. The densities of the reservoirs that contain the liquids are normally in the same order, but the viscosity of the reservoirs varies largely from one to another. It is clear that the higher the viscosity is, the less impact apparent slippage has on the frequency domain (Figure 4. 4).

Table 4. 1 Parameters of sandstone and four different fluids commonly found in the oil reservoir

Grain	Bulk modulus, K_s	50 GPa
	Density, ρ_s	2650 kg/m3
Matrix	Porosity, ϕ	0.2
	Bulk modulus, K_d	18 GPa
	Shear modulus, μ_d	12 GPa
	Permeability, κ_0	200mD
	Average pore radius, Λ	10 μm
	Static Tortuosity, T_∞	3
Oil	Bulk modulus, K_{f1}	2.16 GPa
	Density, ρ_{f1}	890 kg/m3
	Viscosity, μ_{f1}	240 cP
Brine	Bulk modulus, K_{f2}	2.25 GPa
	Density, ρ_{f2}	1040 kg/m3
	Viscosity, μ_{f2}	1 cP
Light oil	Bulk modulus, K_{f3}	0.57 GPa
	Density, ρ_{f3}	700 kg/m3
	Viscosity, μ_{f3}	10 cP
Supercrictical CO2	Bulk modulus, K_{f4}	0.3 GPa
	Density, ρ_{f4}	870 kg/m3
	Viscosity, μ_{f4}	0.5526 cP
Remark: 1 cP=10^{-3} Pa·s; 1mD≈10^{-15} m^2		

4.3. Apparent Slip Effect on Dynamic Permeability and Tortuosity

Johnson et al. (1987) developed a dynamic permeability model by analysing the potential flow and dissipation within the viscous skin depth. We denote this model as the 'JKD' model. It assumes that the vorticity only exists inside the viscous skin depth, which will become much smaller than the characteristic pore size at the high-frequency limit. In this case, the flow, except for the boundary flow within the viscous skin depth, is identical to that for an ideal fluid with a high-frequency limit tortuosity T_∞, which is the same value as the static tortuosity. The dynamic tortuosity $\tilde{T}$ (b, ω) below the high-frequency limit is frequency and wettability dependent, as shown in the following analysis.

The static tortuosity is a purely geometrical factor related to the porosity (Berryman and Thigpen, 1985),

$$T_\infty = 1 - C\left(1 - \frac{1}{\phi}\right), \tag{4.7}$$

where the weighting factor C = 1/2 for spheres and lies between 0 to 1 for other ellipsoids. With a random system of pores with all possible orientations, T_∞ = 3 (Stoll, 1977).

Based on the 'theory of apparent slippage and effective viscosity' above, we introduce the slippage effect into the JKD model by replacing the viscosity with the effective viscosity μ_{f}^{slip}. The wettability dependent dynamic permeability and the dynamic tortuosity under harmonic loading exp(–iωt) are,

$$\tilde{\kappa}(b,\omega) = k_o\left[F(b,\omega) - \frac{\mathrm{i}T_\infty\omega\kappa_0\rho_f}{\phi\mu_{\mathrm{f}}^{slip}}\right]^{-1} \tag{4.8}$$

and

$$\tilde{T}(b,\omega) = T_\infty + \frac{\mathrm{i}\phi\mu_{\mathrm{f}}^{slip}}{\omega\kappa_0\rho_{\mathrm{f}}}F(b,\omega), \tag{4.9}$$

respectively, where,

$$F(b,\omega) = \left(1 - \frac{4\mathrm{i}T_\infty^2\kappa_0^2\rho_{\mathrm{f}}\omega}{\Lambda^2\phi^2\mu_{\mathrm{f}}^{slip}}\right)^{\frac{1}{2}}. \tag{4.10}$$

Λ is the pore structure parameter with dimensions of length, with 2/Λ being the ratio of pore surface to pore volume or the specific area. The factor F(b, ω) plays a role similar to the viscous correction factor in the high-frequency Biot theory (Biot, 1956a). Both the dynamic permeability and the tortuosity are complex-valued. The phase of the dynamic permeability in degree is

$$Phase[\tilde{\kappa}(b,\omega)] = atan\left[\frac{Im(\tilde{\kappa})}{Re(\tilde{\kappa})}\right] \cdot \frac{180}{\pi}, \tag{4.11}$$

where $Im(\tilde{\kappa})$ and $Re(\tilde{\kappa})$are the imaginary and the real part of the complex value, respectively.

There exists the following empirical relation between T, Λ and the static permeability κ_0

$$\frac{\xi T_\infty \kappa_0}{\phi \Lambda^2} = 1, \tag{4.12}$$

where ξ = 8 for a group of non-intersecting canted tube-shape pores. Then, equation 4.10 becomes,

$$F_t(b,\omega) = \left(1 + \frac{\mathrm{i} T_\infty \kappa_0 \rho_\mathrm{f} \omega}{2\phi \mu_\mathrm{f}^{slip}}\right)^{\frac{1}{2}}, \tag{4.13}$$

where ξ = 12 for a group of canted slabs of fluid and,

$$F_s(b,\omega) = \left(1 + \frac{\mathrm{i} T_\infty \kappa_0 \rho_\mathrm{f} \omega}{3\phi \mu_\mathrm{f}^{slip}}\right)^{\frac{1}{2}}. \tag{4.14}$$

Figure 4. 5 compares the normalised dynamic permeability for both tube-shape and slab-shape pores saturated by brine with various slip conditions. The dynamic permeability only deviates from the static permeability in the high-frequency range (>1000 Hz in our example). The normalised dynamic permeability is slightly smaller for tube-shape pores than slab-shape pores under a certain frequency and slip length; however, it decreases when slip length increases in the intermediate frequency for both types of pore network. Therefore, the slip condition promotes the transition from the viscous dominated frequency regime to the inertia dominated frequency regime.

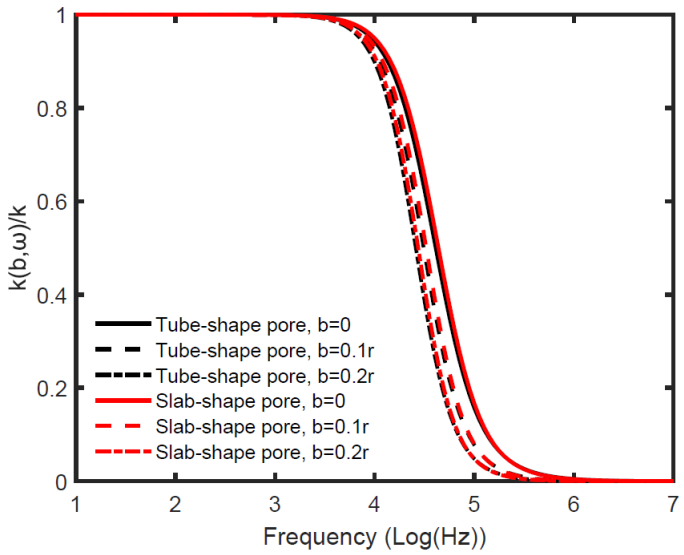

Figure 4. 5 The dynamic permeability normalised by the static permeability for tube-shape and slab-shape pores saturated by brine under various slip conditions.

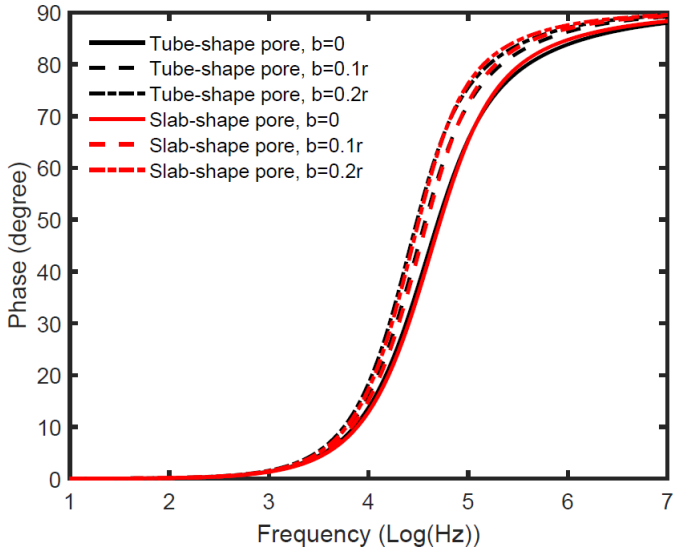

Figure 4. 6 The phase of the dynamic permeability for tube-shape and slab shape pores saturated by brine under various slip conditions.

The phase of the dynamic permeability increases when the slip length increases, indicating the apparent slippage (hydrophobicity) enhances the out-of-phase motion (Figure 4. 6).

The dynamic tortuosity of the tube-shape pore network is higher than that of the slab-shape pore network at low frequency (Figure 4. 7). Nevertheless, both networks converge to the static tortuosity in the high-frequency limit. The slip condition favours the convergence. The higher the slip length is, the closer the dynamic and static tortuosity will be.

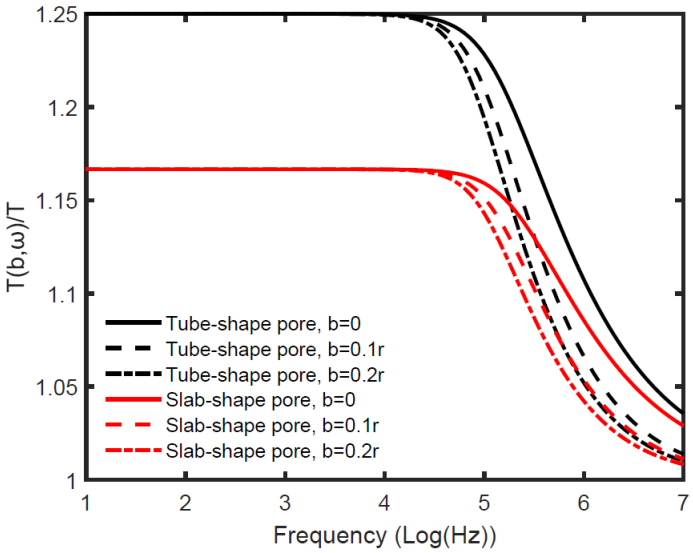

Figure 4. 7 The dynamic tortuosity normalised by the static tortuosity for tube shape and slab shape pores saturated by brine under various slip conditions.

In the high-frequency limit

$$\lim_{\omega\to\infty} \tilde{\kappa}(b,\omega) \to 0\ . \tag{4.15}$$

and

$$\lim_{\omega\to\infty} \tilde{T}(s,\omega) \to T_{\infty}, \tag{4.16}$$

whereas in the low-frequency limit

$$\lim_{\omega\to 0} \tilde{\kappa}(b,\omega) = \kappa_0 \quad , \tag{4.17}$$

and

$$\lim_{\omega\to 0} Im[\tilde{T}(b,\omega)] = \frac{i\mu_f\phi}{\kappa_0\omega\rho_f}. \tag{4.18}$$

It is worth noticing that only the imaginary part of dynamic tortuosity reaches a concise expression, which has been obtained by Johnson et al. (1987). In the second term of the dynamic tortuosity in equation 4.9, the complex factor F(b, ω) cancels out the change of the denominator at low frequencies, rendering the real part of the fraction as non-zero.

4.4. Phase Velocity and Attenuation

The plane-wave solution is commonly used to calculate the phase velocities and dissipation factor represented by the quality factor within the framework of Biot theory (Biot, 1956a; Carcione, 2015; Carcione and Gurevich, 2011; Stoll, 1977).

For a shear wave, the wettability dependent complex velocity is

$$V_s(b,\omega) = \sqrt{\frac{\eta_d}{\bar{\rho}}};\ \bar{\rho} = \rho - \rho_{\mathrm{f}}^2/\rho_1, \tag{4.19}$$

where

$$\rho_1 = \frac{\rho_{\mathrm{f}} T_\infty}{\phi} + \frac{\mu_{\mathrm{f}}^{eff}}{\mathrm{i}\omega\kappa_o}. \tag{4.20}$$

The wettability dependent complex P-wave velocity Vp follows from the quadratic equation

$$\bar{\rho}\rho_1 V_p^4 + a_1 V_p^2 + a_0 = 0, \tag{4.21}$$

where

$$a_1 = \left(2\alpha\rho_f - \rho\right)M - \rho_1\left(K_d + \alpha^2 M + \frac{4}{3}\eta_d\right) \tag{4.22}$$

and

$$a_0 = \left(K_d + \frac{4}{3}\eta_d\right)M. \tag{4.23}$$

To incorporate the wettability dependent dynamic permeability/tortuosity effect, we replace the effective viscosity $\mu_{\mathrm{f}}^{eff}(b,\ \omega) = F\mu_{\mathrm{f}}^{slip}$, where F is determined by equations 4.13 and 4.14.

An alternative plane-wave solution with dynamic tortuosity is given by Johnson et al. (1994b). The complex phase velocities of the normal-mode solutions can be solved explicitly. The detailed equations are included in Appendix A.

We note that the dynamic tortuosity $\tilde{T}$ (b, ω) is used here instead of the static parameter to account for the viscous dissipation.

Once the complex velocities are calculated by equations 4.19 and 4.21, the phase velocity and the inverse quality factor can be calculated,

$$V_{ph} = \left[Re\left(\frac{1}{V_c}\right)\right]^{-1}, \tag{4.24}$$

and

$$Q^{-1} = \frac{2Im\left(\frac{1}{V_c}\right)}{Re\left(\frac{1}{V_c}\right)}, \tag{4.25}$$

where Vc is the complex velocity and c = p+, p– and s.

The attenuation caused by the dissipation of wave energy is quantified by the inverse quality factor Q in equation 4.25. It is defined as the dissipated energy divided by the total wave energy. Another form of the inverse of quality factor Q is

$$Q^{-1} = \frac{Im(V_c^2)}{Re(V_c^2)}, \tag{4.26}$$

which represents the ratio of the time-averaged dissipated-energy density and twice the time-averaged strain-energy density (Carcione, 2015).

Figure 4.8 illustrates the phase velocity of the fast P wave of the fully saturated sandstone for four different fluids. For all cases, the phase velocity increases when the slip length increases in the intermediate frequency. The lower- and upper-velocity limits are unaffected by the slippage. The non-wetting fluid-saturated porous medium has a slightly higher velocity than the velocity of the wetting fluid saturation scenario. The fast P-wave velocity in the porous medium with slab-shape pores is slightly higher than that with tube-shape pores. Similar behaviour on the phase velocity is also found for the slow P wave (Figure 4.9).

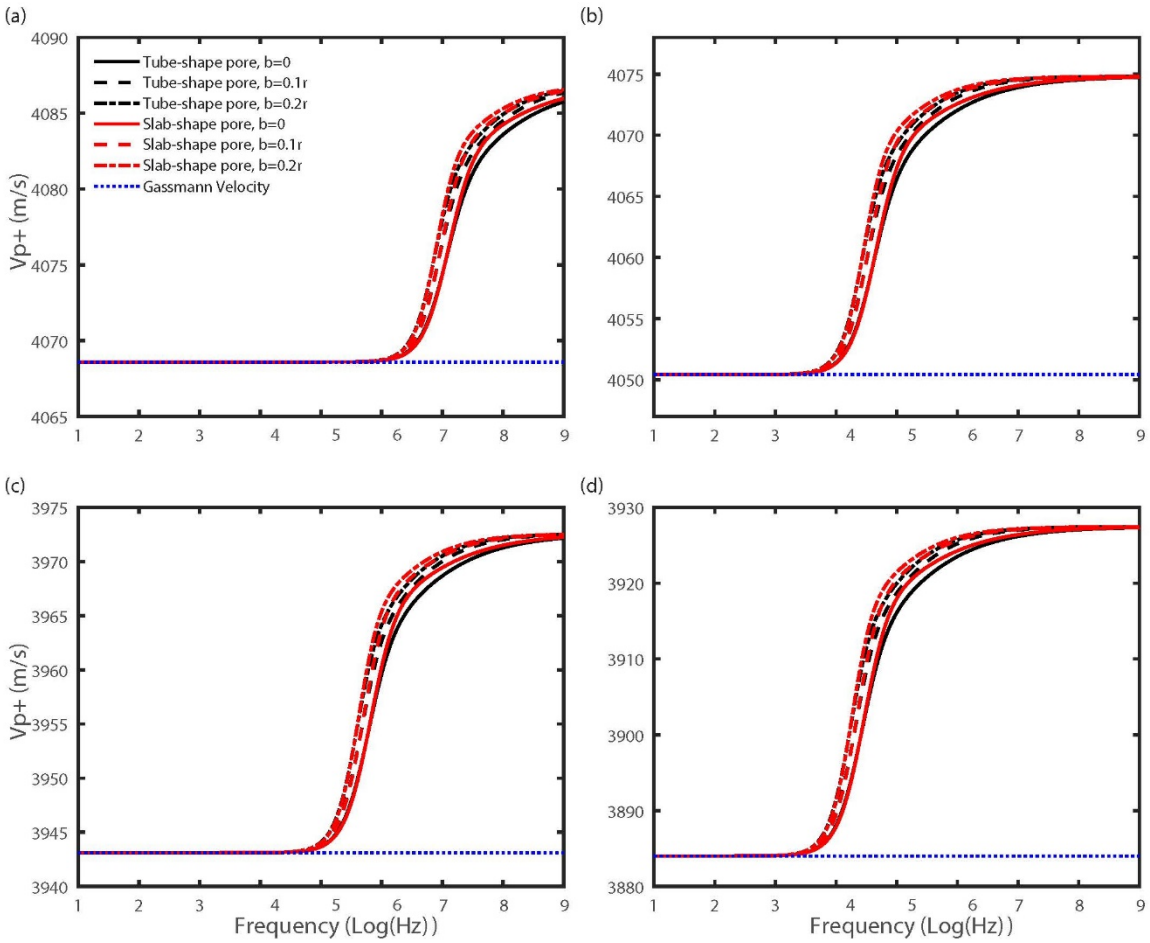

Figure 4. 8 The fast P-wave velocity of fully saturated sandstone. Four types of fluids are used: (a) oil, (b) brine, (c) light oil and (d) supercritical CO2. Parameters in Table 4. 1are used.

The attenuation represented by the inverse quality factor calculated using equation 4.25 is plotted in Figure 4.10 for fast P wave and in Figure 4.11 for slow P wave. For fast P wave, we can see that the tie shape attenuation curve is separated by the frequency of the peak attenuation into two parts, while in the low-frequency range attenuation increases, and in the high-frequency range the attenuation decreases when the slip length increases. Meanwhile, slippage tends to constrain the attenuation in a narrower frequency range than the case of no-slip condition. The critical frequency of the peak attenuation of four fluids saturation cases is in the sequence of: f_c (oil) > f_c (light oil) > f_c (water) ≈ f_c (s – CO_2). The peak attenuations are in sequence of: Q^{-1}(s – CO_2) >> Q^{-1}(light oil) > Q^{-1}(water) > Q^{-1}(oil).

For slow P wave, the attenuation decreases when the slip length increases at any given frequency. There is only a negligible difference in either velocity or the attenuation of the saturated porous medium with the tube-shape and the slab-shape pore networks.

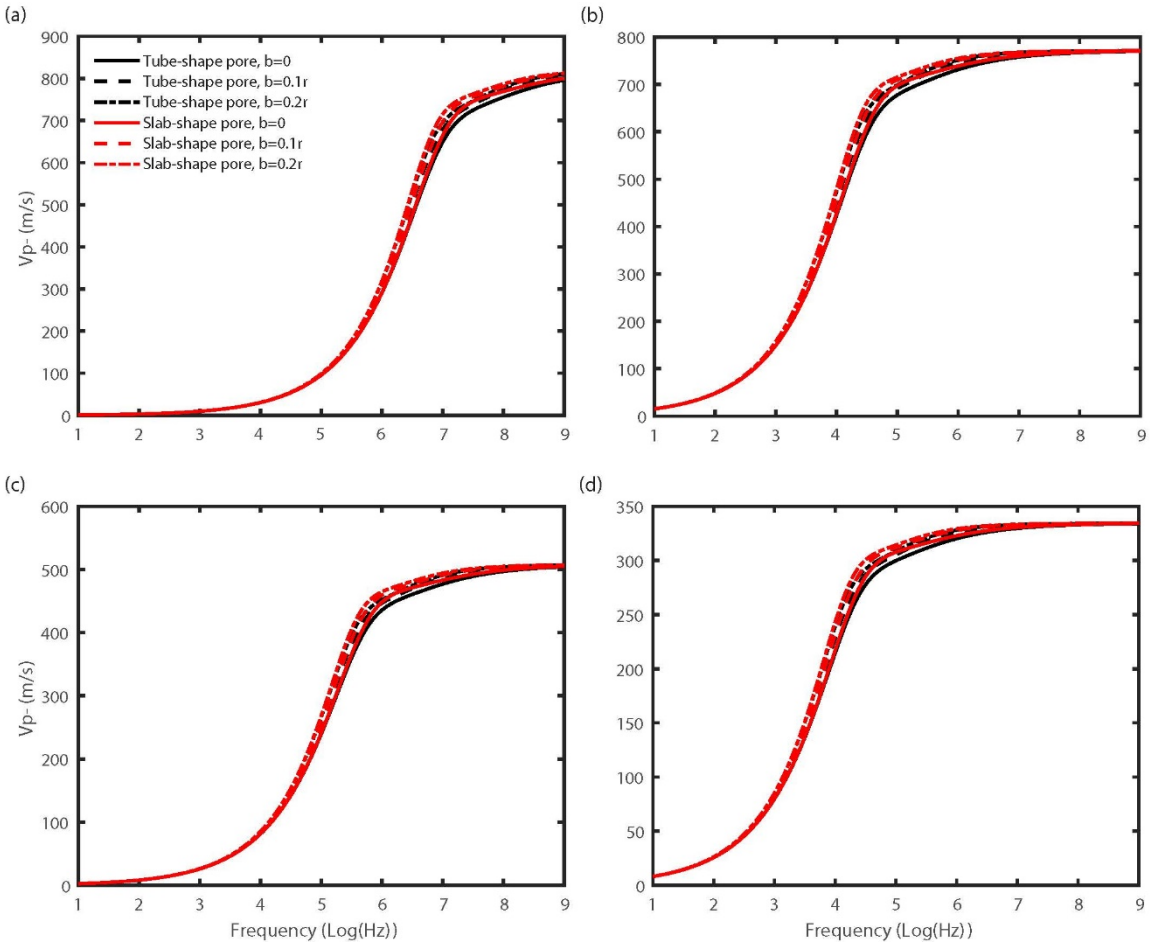

Figure 4. 9 The slow P-wave velocity of fully saturated sandstone. Four types of fluids are used: (a) oil, (b) brine, (c) light oil and (d) supercriticalCO2. Parameters in Table 4.1 are used.

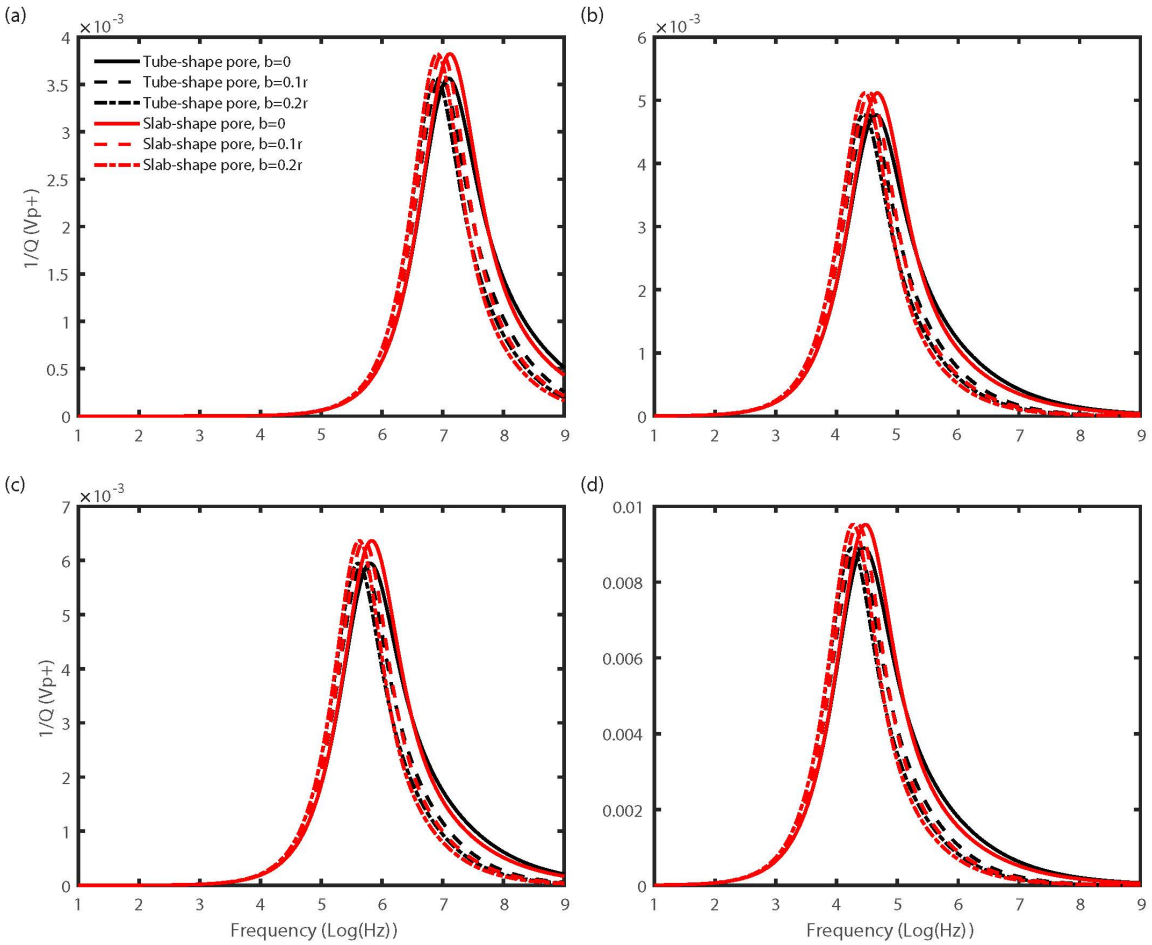

Figure 4. 10 The attenuation (fast P wave) of fully saturated sandstone. Four types of fluids are used: (a) oil, (b) brine, (c) light oil and (d) supercritical CO2. Parameters in Table 4.1 are used.

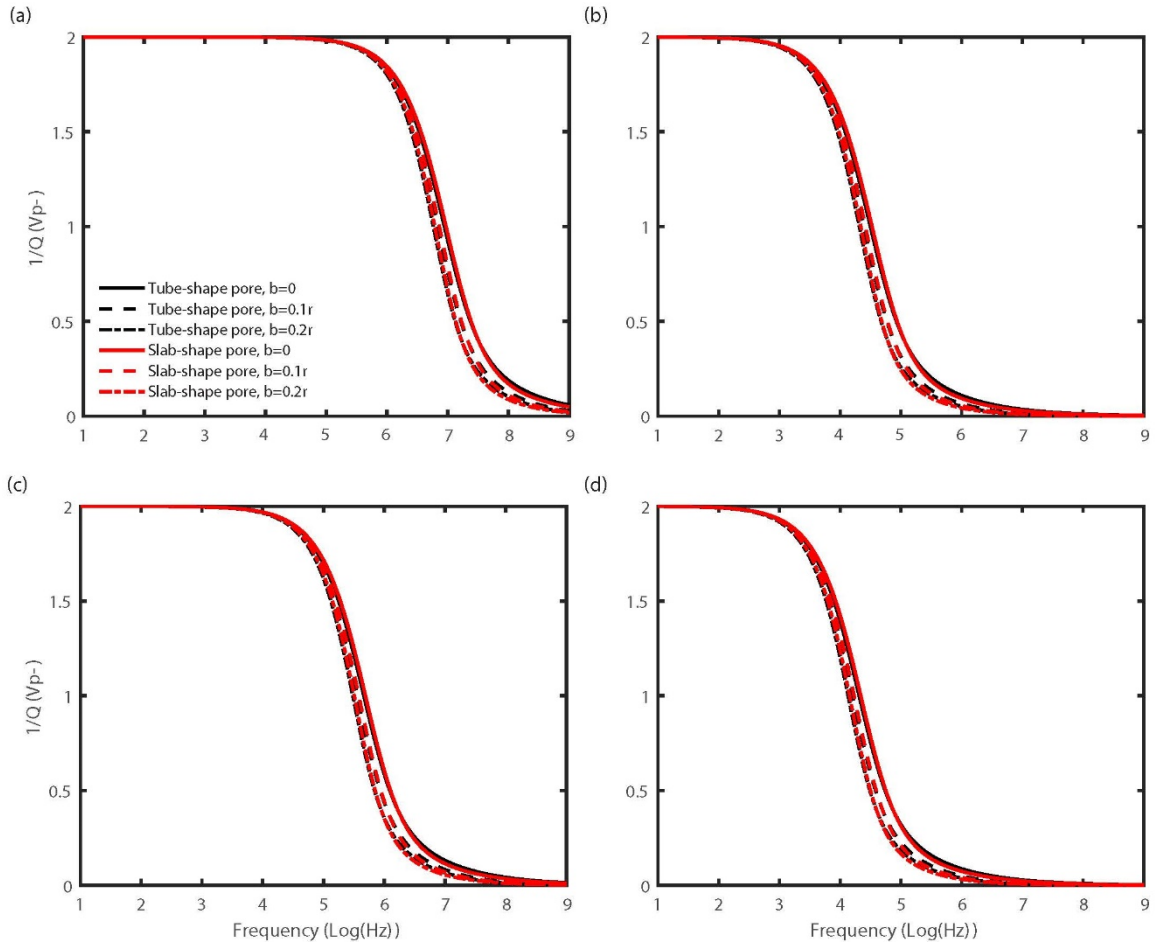

Figure 4. 11 The attenuation (slow P wave) of fully saturated sandstone. Four types of fluids are used: (a) oil, (b) brine, (c) light oil and (d) supercritical CO_2. Parameters in Table 4.1 are used.

4.5. Discussion

The peak attenuation is marked by the Biot characteristic frequency scaled by the tortuosity (Biot 1962),

$$\omega_B = \frac{\mu_f \phi}{\kappa_o \rho_f T_\infty}. \tag{4.27}$$

However, because of the joint effect of the wettability/slippage and the dynamic permeability/tortuosity, the peak attenuation shifts to a much lower frequency than the original Biot frequency. In fact, the viscosity and the tortuosity used in equation 4.27 have become frequency and wettability dependent variables based on the analysis in the previous sections

$$\omega_c = \frac{\phi \mu_f^{eff}(b,\, \omega_c)}{\kappa_o \rho_f T_\infty}, \tag{4.28}$$

where $\mu_{\mathrm{f}}^{eff}(b,\ \omega_c) = F_t\mu_{\mathrm{f}}^{slip}$ acts as effective viscosity for the slip boundary condition and F_t is determined by equation (4.13).

To solve equation (4.28), a simple function is constructed,

$$\mathrm{y}(\omega) = \frac{\mu_{\mathrm{f}}^{eff}(\mathrm{b},\omega)}{\mu_{\mathrm{f}}} - \frac{\omega}{\omega_c} \quad , \tag{4.29}$$

in which ω_c can be obtained numerically by finding the cross point of the curve of y function and x-axis or by finding the minimum value of $|y(\omega)|$ where the corresponding angular frequency is the characteristic frequency ω_c. The calculated critical frequencies $f_c = 2\pi\omega_c$ for a tube-shape porous medium with three different slip lengths are plotted by the vertical lines in Figure. 4.12.

4.6. Conclusion

We introduce the apparent slip model into the JKD dynamic permeability theory and Biot's poroelasticity theory. The vast interface of the pore network, where the fluid and solid contact each other, plays an important role in the wave motion. Wettability is one of the key controlling factors that dominate the hydrodynamic behaviour of the wave-induced flow. The non-wetting fluid tends to slip on the solid boundary, which can be characterised by a reduced apparent viscosity. By taking advantage of the apparent viscosity, the dynamic permeability, tortuosity, phase velocities and attenuation are analysed for the fully saturated sandstones in the cases of two types of pore network and four different fluids. We conclude that the dynamic permeability slightly decreases when the slippage/hydrophobicity increases in the intermediate frequency but the phase velocity slightly increases. Moreover, the critical frequency represents the peak attenuation shift to a lower frequency when slippage occurs.

Chapter 5. Pore Size Distribution Controls Dynamic Permeability

This chapter is a published peer-reviewed journal paper in *Geophysical Research Letters*:

Li, J. X., Rezaee, R., Müller, T. M., & Sarmadivaleh, M. (2020). Pore Size Distribution Controls Dynamic Permeability. Geophysical Research Letters, e2020GL090558.

5.1. Introduction

Analogous to the direct current (dc) and alternating current (ac) electrical conductivity of metals, the dc and ac permeability are prime characteristics of a porous medium. The estimation of the flow (dc) permeability in presence of a fluid pressure gradient is of uttermost importance in geo-fluid detection (Blunt, 2017), water resource management and development (Ghanbarian et al., 2016; Molz et al., 1989; Neuzil, 1986), biomechanics and mechanobiology (Benalla et al., 2012; Cardoso et al., 2013), nuclear waste disposal and storage (Liu, 2014; Reynes et al., 2001), and chemical engineering (Xue et al., 2018). When the fluid pressure gradient is time-harmonic, for example, when induced by elastic waves, oscillatory motion arises and then the ac (dynamic) permeability concept originally developed by Johnson et al. (1987) is essential with direct applications in borehole acoustics (Lin, 2011; Zhang and Müller, 2019).

The so-called JKD model of Johnson et al. (1987) for the ac permeability is known to work well in porous media with relatively simple pore structures (Charlaix et al., 1988; Sheng and Zhou, 1988; Zhou and Sheng, 1989). Various theoretical and numerical analyses point out the limitations of the JKD model in the presence of corrugated pore channels as typically observed in porous rocks (Achdou and Avellaneda, 1992; Cortis et al., 2003). Then, the bulk fluid flow contribution dominates the flow in the viscous boundary layer (VBL), resulting in slower convergence of the dynamic permeability to its high-frequency asymptotic limit. Recent oscillating-flow experiments and simulations have documented the anomalous phase of the dynamic permeability, which are believed to be related to the poroelastic coupling between fluid and solid as well as to microscopic heterogeneity such as variable pore sizes (Hasanov et al., 2020; Hasanov et al., 2019). The importance of pore sizes and their distribution on the hydrodynamics of oscillating flows has also been recognized (Achdou and Avellaneda, 1992). Given that the pore sizes in rocks are highly variable and their spatial distribution is complex, one expects that the ac permeability is strongly controlled by the pore size distribution (PSD). However, its impact is typically neglected or oversimplified, for example, by roughly estimating parameters in the existing dynamic permeability models (Müller and Sahay, 2011c;

Pazdniakou and Adler, 2013). This is striking since the pore size distribution in rocks is measurable in the laboratory and in situ in boreholes.

Perhaps the most popular laboratory techniques for PSD determination include experiments of mercury injection capillary pressure (MICP), gas absorption, and nuclear magnetic resonance (NMR) (Al Hinai et al., 2014; Xiao et al., 2016). However, due to environmental and economic concerns, modern approaches more commonly construct the capillary pressure curve and the PSD from NMR measurements (Eslami et al., 2013; Xiao et al., 2016). It is also common to extract the PSD from image analysis of scanning electron microscopy (SEM) or micro-computed tomography (μ-CT) (Blunt, 2017; Widiatmoko et al., 2010) with excellent visualization of pore structure. However, such image-based PSD is often restricted to very small areas or sub-volumes, making it unrepresentative for macroscopic formations. Thus, from this perspective, the PSDs from NMR or MICP are better choices, since they provide averaged values (i.e. core or even larger scale) and yet sufficient detail to represent macroscopic spatial variations. Especially, the inversion of PSD from NMR spectra is of great practical significance given its applicability in borehole measurements. In this letter, we construct a dynamic permeability model that incorporates the broadband PSD derived from NMR measurements.

5.2. Theory

5.3.1. Hydrodynamics of Oscillating Flow at Pore-scale

Let us consider a representative pore channel saturated by a viscous fluid with shear viscosity μ_{f} and density ρ_{f}. Under the action of an externally imposed, harmonic loading $\mathrm{e}^{-i\omega t}$, a fluid parcel performs an oscillatory movement along the channel axis. The fluid velocity can be decomposed into a potential flow field up and a viscous flow field due to the drag of the pore wall (Biot, 1956b; Lighthill and Lighthill, 2001),

$$\mathbf{u} = \mathbf{u_p}[1 - \tilde{v}] \,, \tag{5.1}$$

where $\tilde{v}$ is conceived as the viscous flow velocity normalized by $|\mathbf{u_p}|$. Only the viscous flow contributes to the Darcy flow, observed at macro-scale and through which the dc permeability is defined. In contrast, the potential flow is independent of the shear viscosity. With increasing frequency, the viscous skin depth$\delta = \sqrt{2\mu_{\mathrm{f}}/\rho_{\mathrm{f}}\omega}$ becomes very small and the oscillatory flow is dominated by the flow in the bulk volume (Cortis et al., 2003). Thus, with increasing

frequency, the dc permeability is expected to vanish and the frequency-dependent transition is governed by the ac permeability. For idealized pore geometries, the normalized velocity of bulk flow is a function of pore size *r*:

$$\tilde{v}(k(\omega);r) = \begin{cases} e^{ikr}, & \text{Flat pore wall} \\ \frac{1}{cosh(ikr)}, & \text{Slit pore} \\ \frac{1}{J_0(kr)}, & \text{Cylindrical pore} \end{cases} \tag{5.2}$$

Here *r* is half of the aperture length for planar and slit-like pores or the radius for the cylindrical pore. The viscous wave describing the process of vorticity diffusion has the wave number $k = (1 + \mathrm{i})/\delta$. $J_0(\,)$ denotes the zero-order Bessel function.

For an assemblage of pores, that is, a porous medium with porosity ϕ, the dc permeability is proportional to the square of the effective hydraulic length scale r_h, that is, $\kappa_0 \propto r_h^2$. This dc permeability becomes only meaningful for a low-frequency regime $\delta \gg r_h$, but not for a high-frequency regime when potential flow prevails as $\delta \ll r_h$. The crossover frequency is the Biot frequency (Biot, 1956a) scaled by the tortuosity T_∞: $\omega_B = \phi\mu_\mathrm{f}/T_\infty\kappa_o\rho_\mathrm{f}$ (Charlaix et al., 1988; Sheng and Zhou, 1988).

5.3.2. Interaction of Propagating and Diffusive Waves at Macro-Scale

The volume averaging framework of poroelasticity systematically brings the role of the diffusive viscous wave to the macroscopic level, that is, at the scale of a porous medium containing one or multiple pore networks (Sahay et al., 2001). The diffusive viscous wave in the VBL emerges at the macro-scale as slow shear (S-) wave, which is the fourth kind of wave in fluid-saturated porous media (Sahay, 2008). The conversion scattering from fast P- to slow S-waves in a weak-fluctuation approximation results in an effective P-wavenumber (Müller and Sahay, 2011b),

$$k_1 = k_1^\infty\left[1 + \Delta_1\left(1 + k_4^2\tilde{\ell}^2\right)\right]. \tag{5.3}$$

This means that an incoming P-wave (k_1^∞) is becoming attenuated due to conversion into the slow S-wave (k_4), or equivalently, due to the presence of VBL. Δ_1 represents a combination of variances of the randomly fluctuating medium parameters and $\tilde{\ell}^2$ contains their characteristic length scales. Similarly, a propagating slow P-wave k_2^∞ is becoming attenuated due to conversion scattering into the slow S-wave according to Müller and Sahay (2011c),

$$k_2 = k_2^{\infty}\left[1 + \Delta_1\left(1 + k_4^2\tilde{\ell}^2\right)\right]. \tag{5.4}$$

In equations (5.3) and (5.4), the complex-valued slow S-wave number is $k_4 = k_- + ik_+$ with

$$k_{\mp} = \sqrt{\frac{\omega}{2d_{\mathrm{f}}D_v}}\sqrt{\sqrt{(1 + d_{\mathrm{f}}m_{\mathrm{f}})^2 + \frac{\omega_B^2}{\omega^2}} \mp \frac{\omega_B}{\omega}} \tag{5.5}$$

where $d_{\mathrm{f}} = 1/(T_{\infty} - m_{\mathrm{f}})$, $m_{\mathrm{f}} = \phi\rho_{\mathrm{f}}/[\phi\rho_{\mathrm{f}} + (1-\phi)\rho_s]$ is the fluid mass fraction, ρ_s is the density of the solid. Thus, in the porous medium context, the normalized velocity of bulk flow $\tilde{v}(k(\omega); r)$ is obtained by replacing the wave number of the ordinary diffusive wave k in equation (5.2) by the slow S-wave number k_4.

5.3.3. Dynamic Permeability Based on Pore Size Distribution

Müller and Sahay (2011c) draw an analogy between the slow P-wave in the inertial regime k_2^{∞} and the potential flow field to develop a model for the dynamic permeability based on the frequency-dependent $k_2 \to k_4$ conversion scattering process. Key to this model is the interpretation of the dynamic length scale in equations (5.3) and (5.4),

$$\tilde{\ell}^2 = \int_0^{\infty} rB(r)e^{ik_4 r}dr. \tag{5.6}$$

It arises due to the presence of random heterogeneity, whose spatial correlation function is $B(r)$, and the slow S-wave number k_4 as a proxy for the vorticity diffusion process in the VBL. We remark that the use of equation (5.6) for heterogeneous porous media is permitted since equations (5.3) and (5.4) are macroscopic equations. Here, we conceptualize the heterogeneous porous medium as a medium in which the sub-porosity is variable in space. For such a multiple porosity medium, we assign to each incremental porosity ϕ_i, a characteristic hydraulic length r, which quantifies the dominant pore size associated with the spatial domain of ϕ_i. This is symbolically denoted as $\phi_i(r)$. We assume that this length is variable within a range $r \in [r_{min}, r_{max}]$. Then, the dynamic length scale becomes

$$\tilde{\ell}^2 = \int_{r_{min}}^{r_{max}} r\phi_i(r)\tilde{v}(k(\omega); r)\, dr. \tag{5.7}$$

We note that the finite range of integration replaces the requirement of a vanishing $B(r \to \infty)$ in the original weak-fluctuation approximation. Since laboratory measurements of the pore size and the corresponding distribution of the incremental porosity are discrete quantities, we

discretize the integral. Assuming that there are *n* different characteristic hydraulic lengths in $[r_{min}, r_{max}]$ with an increment $\Delta r = (r_{max} - r_{min})/n$, we find

$$\tilde{\ell}^2 = \sum_{r_{min}}^{r_{max}} \left(r\phi_i(r)\tilde{v}(k(\omega); r) \right) \Delta r. \tag{5.8}$$

Without the oscillating perturbation, the $\tilde{\ell}$ defined in equation (5.8) is a length scale $\tilde{\ell}\ (k_4 = 0) = \sqrt{\phi r_a \Delta r}$ associated with the average pore size $r_a = \sum r\phi_i/\phi$. The incremental porosity ϕ_i is the calibrated porosity, associated with all pores of the i^{th} pore size (Coates et al., 1999). Under the excitation of external harmonic loading, the frequency-dependent square of length scale $\tilde{\ell}^2$ controls the amount of the fluid in the porous medium contributing to Darcy flow. Therefore, the term $\Delta_1 \tilde{\ell}^2$ in equations (5.3) and (5.4) acts as the dynamic permeability. In the low-frequency limit, the dynamic permeability is not arbitrary but has to converge to the dc permeability. Thus, the dynamic permeability incorporating a discrete PSD (with measured r and ϕ_i) is

$$\tilde{\kappa} = \kappa_0 \sum_{r_{min}}^{r_{max}} r\phi_i(r)\tilde{v}(k_4(\omega); r) / \sum_{r_{min}}^{r_{max}} r\phi_i(r)\tilde{v}(k_4^0; r)\ , \tag{5.9}$$

where $k_4^0 \equiv k_4(\omega \to 0) = i\sqrt{\phi/\kappa_o T_\infty d_f}$. It allows us to quantify the dynamic permeability in porous media with multiple porosity peaks in the discrete PSD. Thus, equation (5.9) provides a possible cross-link between seismic sounding and the PSD probing techniques such as NMR.

5.3.4. Dynamic Permeability for Different Wettability Conditions

Based on the different hydrodynamic behavior of fluids on hydrophobic and hydrophilic solid surfaces, the impact of the wettability on the dynamic permeability is represented by the slip boundary condition (SBC) (Li et al., 2020a; Li et al., 2020b). The wettability indicator, the static contact angle θ_c for the liquid cluster immersed in its vapor on a solid surface, and the slip length b follow the scaling relationship $b \propto (1 + cos\theta_c)^{-2}$ (Huang et al., 2008; Ortiz-Young et al., 2013). Thus, the wettability of a porous medium can be modeled by a variable slip length ($b > 0$). The effective shear viscosity corresponding to SBC is the apparent viscosity of the fluid inside the VBL (Li et al., 2020b),

$$\mu_{\mathrm{f}}^{slip} = \frac{\mu_{\mathrm{f}}}{1 + \frac{b}{\delta_p(\omega)}}\ . \tag{5.10}$$

where $\delta_p(\omega) = |(1+\mathrm{i})/k_4|$ is a modified viscous skin depth. This approximation implies that the VBL has a finite thickness in the low-frequency limit, $\delta_p^0 = |(1+\mathrm{i})/k_4^0|$. Thus, $\mu_\mathrm{f}^{slip}(\omega \to 0) = \frac{\mu_\mathrm{f}}{1+\frac{b}{\delta_p^0}} \leq \mu_\mathrm{f}$, which in turn implies that the effective dc permeability exceeds κ_o,

$$\kappa_0^{slip} = \kappa_o \left(1 + \frac{b}{\delta_p^0}\right) \geq \kappa_o \, . \tag{5.11}$$

This means that a hydrophobic porous medium saturated by a nonwetting fluid corresponds to the SBC where the effective dc permeability is higher than that in the case of wetting fluid saturation, in agreement with Javadpour et al. (2015). There is also a close resemblance to the model of Berg et al. (2008). By using the effective viscosity μ_f^{slip} and the effective dc permeability κ_0^{slip} for SBC in equation 9, we obtain a generalization of the dynamic permeability model to account for the wettability condition.

5.3. Implications

5.3.1. Dynamic Permeability for Bimodal PSD

In order to evaluate the impact of PSD on dynamic permeability, we construct two different bimodal pore size distributions often observed for rocks (Xiao et al., 2016). The PSD of example #1 includes a large portion of big pores and only a little portion of small pores, a typical feature for conventional sandstones (black curve in Figure 5. 1a, b). In contrast, in example #2 the PSD means that the pore volume of small-sized pores comprises a larger portion of the pore volume than that of large-sized pores. This PSD is often characteristic for so-called tight rocks (red curve in Figure 5. 1a, b). We note that this name is used only tentatively since there is high variability among tight rocks. Real and imaginary parts of the dynamic permeability (without and with SBC) are shown in Figure 5. 1c, d. To investigate the effect of PSD solely, we use in both examples the parameters given in Table 5. 1. The slip length is arbitrarily chosen as $b = 0.1 r_e$ for the SBC, where the effective capillary radius $r_e = 5\sqrt{\kappa_0/\phi}$ (Berg et al., 2008; Blunt, 2017).

We observe that the dynamic permeability of the nonwetting fluid saturated hydrophobic porous medium (SBC) in the high-frequency range converges more quickly as compared to the hydrophilic case (Figure 5. 1c). Compared to the quick convergence to the low limit value in conventional rock (#1), the real part of the dynamic permeability for tight rock (#2) has a slower convergence rate. The negative real part of dynamic permeability in the frequency range around

1 MHz indicates that the motion of the bulk fluid is out-of-phase with respect to the solid frame. The imaginary part of the hydrophobic case is higher at low frequencies, but lower at high frequencies than that of the hydrophilic case indicating that the hydrophobicity of SBC promotes the relative motion of the fluid, therefore increase the dissipation in low frequencies, but diminishes the viscous friction at high frequencies (Figure 5. 1d).

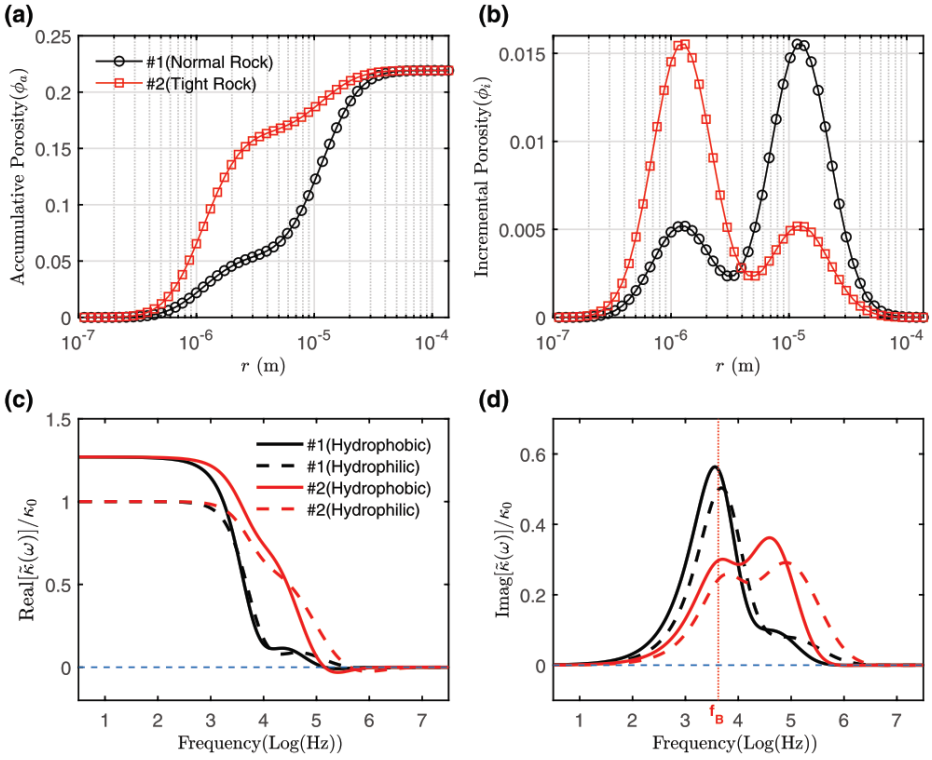

Figure 5. 1 (a) Accumulative and (b) incremental porosity of two bimodal pore size distributions; (c) real and (d) imaginary part of the dynamic permeability and approximation in the slip boundary (hydrophobic) condition. The horizontal dash lines indicate zero values. The vertical dotted line marks the Biot frequency $f_B = \omega_B/2\pi$.

Parameter	Value	Unit
Grain		
Density ρ_s	2650	kg/m^3
Frame		
Porosity ϕ	0.2192	
Permeability κ_o	3×10^{-12}	m^2
Tortuosity T_∞	2.78	
Fluid		
Density ρ_f	1000	kg/m^3
Viscosity μ_f	0.001	Pa•s

Table 5. 1 Parameters for water-saturated Bentheimer sandstone.

In contrast to the smooth crossover predicted by the JKD model, the PSD-dependent dynamic permeability exhibits quite different patterns. This is because the variability of the pore sizes

is embedded in our model. The imaginary parts have two peaks, which is especially prominent for the tight rock because of its large portion of the pore volume comprised of small size pores. The Biot frequency coincides with the low-frequency peak indicating the general validity of the relation $\tilde{\kappa}(\omega)/\kappa_o = f(\omega/\omega_B)$ with the corresponding characteristic pore size $r_c \sim \sqrt{\kappa_0/\phi}$. The high-frequency peaks arise due to the presence of smaller characteristic pore sizes.

5.3.2. Dynamic Permeability for Measured PSD

We infer the pore sizes and their distribution for a Bentheimer sandstone sample by using the Magritek 2 MHz NMR Rock Core Analyzer. Following the experimental protocol of Xiao et al. (2016), we obtain 53 data points of the NMR T2 (transverse relaxation time) distribution data, which are subsequently calibrated to pore size distribution by using the mercury injection data (Figures (5.2a, b)). The SEM image is taken at the same time for grain shape/sorting analysis (inset of Figure (5.2a)), which also illustrates the complexity of pore spaces (light red shading in the inset of Figure (5.2b)).

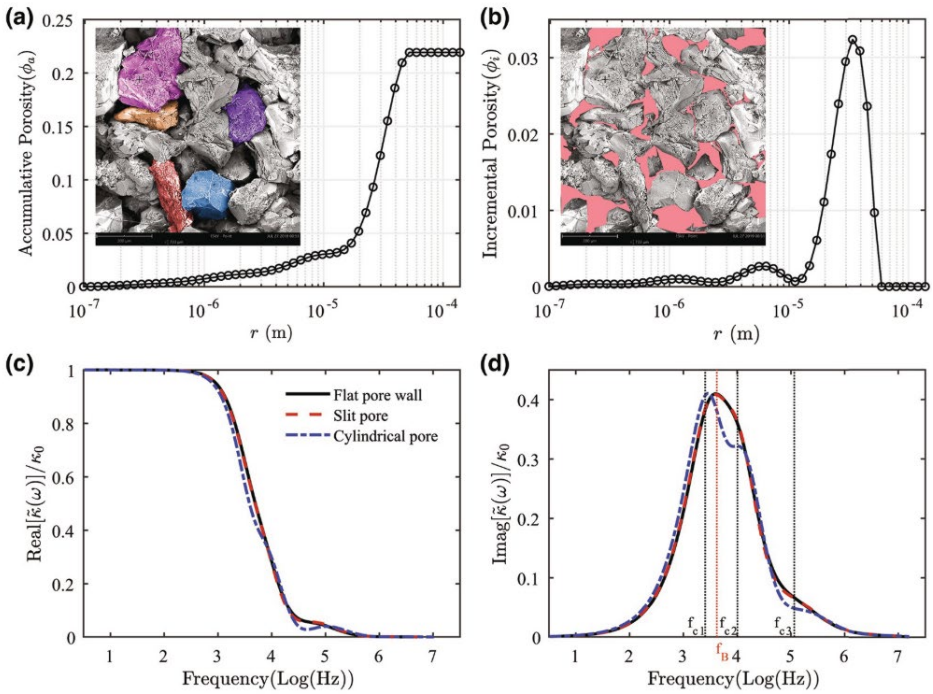

Figure 5. 2 The pore sizes and the distribution of (a) accumulative and (b) incremental porosity for Bentheimer sandstone obtained from NMR T2 data (53 measurement points) calibrated by the pore throat radii distribution of MICP; SEM image in the insets demonstrates the Bentheimer sandstone has well-sorted grain framework but complicated pore network structure (light red shading in (b)). A comparison of the (c) real parts and (d) imaginary parts of the dynamic permeability normalized by dc permeability for the Bentheimer sandstone by three different pore shape models. The Biot frequency f_B is marked

by the red dashed line. The characteristic frequencies f_{c1}, f_{c2}, f_{c3} are associated with the characteristic pore sizes. MICP, mercury injection capillary pressure; NMR, nuclear magnetic resonance; SEM, scanning electron microscopy.

Using the parameters in Table 5. 1, the real parts and imaginary parts of normalized dynamic permeability are shown in Figure 5. 2c, d. The dynamic permeability based on PSD has a lot of similarities with other dynamic permeability models (Achdou and Avellaneda, 1992; Johnson et al., 1987; Müller and Sahay, 2011c; Sheng and Zhou, 1988). For instance, the scaling function $\tilde{\kappa}(\omega)/\kappa_o = f(\omega/\omega_B)$ is validated for the dynamic permeability based on PSD (Figure 5. 2). It is clearly segmented by the Biot frequency $f_B = \omega_B/2\pi$ into two parts: the viscous dominated regime at low frequencies ($f \ll f_B$) where $\tilde{\kappa} \approx \kappa_o$, and the inertia dominated regime at high frequencies ($f \gg f_B$)), where the dynamic permeability decreases as frequency increases. The difference between the three pore shape models of PSD dependent dynamic permeability is insignificant, especially in the low-frequency range, thus validating the insensitivity of the dynamic permeability to the microstructure (Sheng and Zhou, 1988).

5.3.3. Characteristic Frequencies

In Figure 5. 1d and Figure 5. 2d, the Biot frequency f_B matches the main peak of the imaginary part of the dynamic permeability very well. In addition, we observe that at high frequencies there are further characteristic frequencies associated with characteristic pore sizes. Because the dynamic permeability model involves the slow S-wave, a characteristic frequency fc arises when the slow S wavelength λ is on the order of the characteristic pore size of a certain pore network. Substituting equation (5.5) for the slow S-wave number into $k_4 = 2\pi/\lambda$, we find

$$f_c = \frac{2\mu_{\mathrm{f}}}{T_\infty \rho_{\mathrm{f}}} \sqrt{\frac{4\pi^2}{\lambda^4} + \frac{\phi/(\kappa_o T_\infty d_{\mathrm{f}})}{\lambda^2}}\,. \tag{5.12}$$

At high frequencies, $f \gg f_B$, we have $1/\lambda^4 \gg 1/\lambda^2$ and thus

$$f_c = \frac{4\pi\mu_{\mathrm{f}}}{T_\infty \rho_{\mathrm{f}} \lambda^2}\,. \tag{5.13}$$

Interestingly, the characteristic pore sizes are not necessarily the pore sizes with local porosity extremes in the pore size distribution but rather they represent the local extremes of contribution to the bulk viscous flow, and hence the Darcy flow.

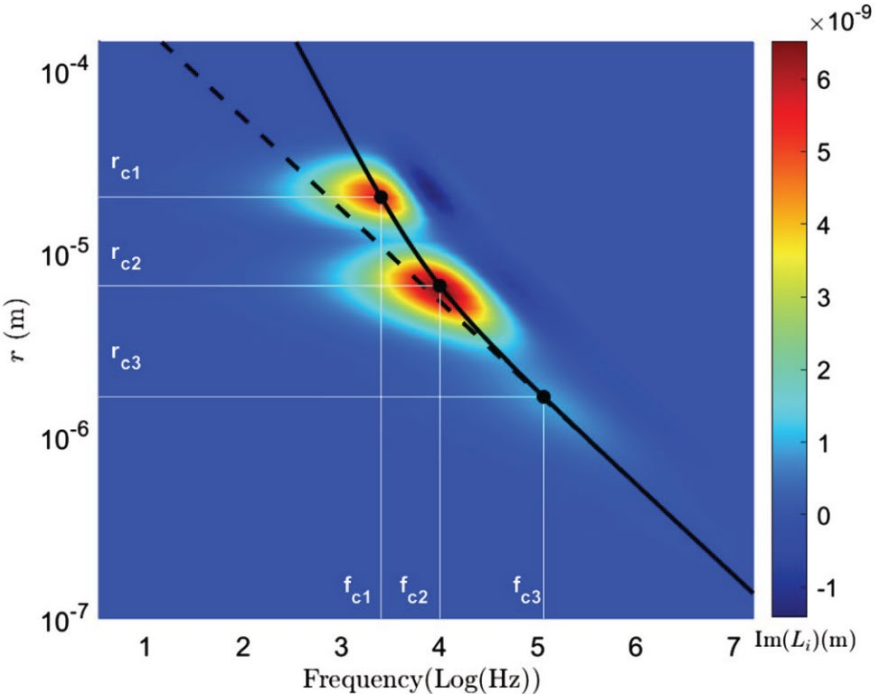

Figure 5. 3 Imaginary part of the length scale $L_i(\omega; r) = r\phi_i\tilde{v}$ as a function of frequency and pore size where the solid black line ($\lambda \approx 4r$) based on equation (5.12) corresponds to the pore-scale dissipation peaks and the high-frequency linear asymptotic approximation based on equation (5.13) is plotted as a dashed line.

According to equation (5.8), the dynamic permeability is controlled by the frequency-dependent length scale $L_i(\omega; r) = r\phi_i\tilde{v}$. The local peaks in the imaginary part are linked by the characteristic pore sizes (i.e. r_{c1}, r_{c2}, r_{c3} for Bentheimer sandstone) and the corresponding characteristic frequencies (Figure 5. 3) when the slow S-wavelength approaches the characteristic pore sizes $\lambda \approx 4r_c$. It means that the highest dissipation at pore scale occurs as the half wavelength of slow S-wave is comparable to the pore opening ($2r$). These sub-characteristic frequencies (i.e. f_{c1}, f_{c2}, f_{c3} for Bentheimer sandstone) result in the piece-wise curvature pattern in the dynamic permeability (Figure 5. 2c, d).

5.4. Discussion and Conclusions

The recent oscillating-flow experiments and simulations have documented the frequency dependence of permeability and anomalous phase of the dynamic permeability, which are believed to be related to the spatial heterogeneity and the coupling between pore pressure diffusion and elastic deformation (Bernabé et al., 2004; Hasanov et al., 2020; Hasanov et al., 2019). It lends support to our finding that the dynamic permeability is controlled by the pore size distribution. While this result was anticipated, our proposed model for $\tilde{\kappa}(\omega)$ makes a

quantitative connection for the first time. For multimodal PSDs with distinguishable peaks additional characteristic frequencies arise, which clearly manifest in the imaginary part of the dynamic permeability as additional peaks.

The wettability condition affects not only the dynamic permeability but also the dc permeability. Interestingly, for a porous medium with parameters in Table 5.1, we find that the effective dc permeability in slip boundary condition (equation (5.11)) is equivalent to the Berg model $\kappa_0^{slip} = \kappa_0 \left(1 + C \frac{b}{r_e}\right)$ by using the constant $C \approx 3.3$. This is very close to the value ($C = 4$) obtained by Berg et al. (2008) for the end-point relative permeability of nonwetting fluid saturation.

There are broader implications. The proposed model provides a link between PSD as obtained by NMR measurements and the dynamic permeability, which in turn, controls attenuation and dispersion of seismic waves at high frequencies ($f \gg f_B$). For example, in boreholes, either Stoneley wave or NMR can be applied to estimate the formation permeability. Therefore, in principle, the proposed model might lead to a cross-fertilization of experimental and in-field techniques. Moreover, since dynamic permeability is an integral part of seismoelectric theory, we expect that our model gives further impetus in the analysis of seismoelectric signals.

Chapter 6. Vorticity Dissipation and Slip Boundary Condition on Biot Mechanism in the Porous Media with Broadband Pore Size Distribution

6.1. Introduction

The poroelasticity of the fluid saturated porous medium is well described by Biot theory, which incorporates the global flow accounting for the viscous frictional attenuation (Biot, 1956a). It is extended to be applicable in the high-frequency range by the analysis of the hydrodynamics of the oscillatory flow in the slit and cylindrical pore to capture the deviation of the Poiseuille flow (Biot, 1956b). The velocity of the viscous fluid flow with respect to the pore wall includes a viscosity independent potential flow field and a viscous flow field where the latter can be described as a viscous wave.

By incorporating the fluid strain rate into the constitutive equations, Sahay (2008) find such viscous wave in porous media is a slow S-wave which drains energy from the propagating waves through the conversion scattering process (Müller and Sahay, 2011b).

The slow S- wave in porous media is a non-propagating diffusive wave as the fourth kind of wave beside the three kinds of waves predicted by Biot theory. Its wavenumber is $k_4 = k_- + ik_+$ with (Müller and Sahay, 2011c),

$$k_{\mp} = \sqrt{\frac{\omega\,\rho_{\mathrm{f}}}{2d_{\mathrm{f}}\mu_{\mathrm{f}}}}\sqrt{\sqrt{(1+d_{\mathrm{f}}m_{\mathrm{f}})^2+\frac{\omega_{\mathrm{B}}^2}{\omega^2}}\mp\frac{\omega_{\mathrm{B}}}{\omega}} \tag{6.1}$$

The crossover angular frequency ω_{B} is the Biot frequency scaled by the tortuosity,

$$\omega_{\mathrm{B}} = \frac{\phi\mu_{\mathrm{f}}}{T\rho_{\mathrm{f}}\kappa_o}. \tag{6.2}$$

where ρ_{f} and μ_{f} are the density and viscosity of the fluid, respectively, and κ_o is the permeability. The parameter $d_{\mathrm{f}} = 1/(T - m_{\mathrm{f}})$, T is the tortuosity, and $m_{\mathrm{f}} = \phi\rho_{\mathrm{f}}/[\phi\rho_{\mathrm{f}} + (1-\phi)\rho_{\mathrm{s}}]$ is the fluid mass fraction, ϕ is the porosity, ρ_{s} is the density of the solid. In the low-frequency viscous-dominated regime, the slow S- wave is found as a heavily damped diffusive wave so that it dies off rapidly near the pore wall (Sahay, 2008).

When a fast-compressional wave passes through the porous medium, the tangential shear stresses of the pore wall slow the fluid down so as to its relative velocity to be zero at the solid boundary, creating a profile of flow velocity with gradients. It occurs in each wave cycle as an

oscillating flow wherein the slow S-wave generated on the pore wall diffuses away in the normal direction, and the viscous fluid is transformed into rotational vortices within the viscous boundary layer (VBL). The shear stresses in the viscous fluid are equilibrated through vorticity diffusion (Müller and Sahay, 2011a; Müller and Sahay, 2010).

The vorticity quantifies the rotational motion of the fluid in the vicinity of the solid surface, which rapidly decays into the irrotational potential flow across the VBL as illustrated in Figure 6. *1*a (Johnson et al., 1987; Landau and Lifshitz, 1987; Lighthill and Lighthill, 2001; Müller and Sahay, 2011a). The vorticity vector $\vec{\Omega} = \mathrm{rot}\,\mathbf{v}$ obeys the right-hand rule where its sign depends on the direction of the fluid spin motion (Figure 6. 1b). A parabolic profile of the flow velocity ($\mathbf{v}$) is created when the largest flow velocity occurs in the middle of the pore but decreases towards the pore wall ($x = \pm r$) so that the fluid particles are pushed to conduct the circular motion from the centre to the sides. It can be visualized by imaging the spiral paddle wheels in the flow where the direction of the vorticity points out of the plane. Curl the fingers of the right hand in the direction of the spiral wheel, and if the thump points up, the vorticity is positive. If the thump points down, the vorticity is negative. Hence, the vorticity has an opposite sign for the two sides of the flow velocity profile plane but forms axis symmetry in the three dimensions at any given frequency.

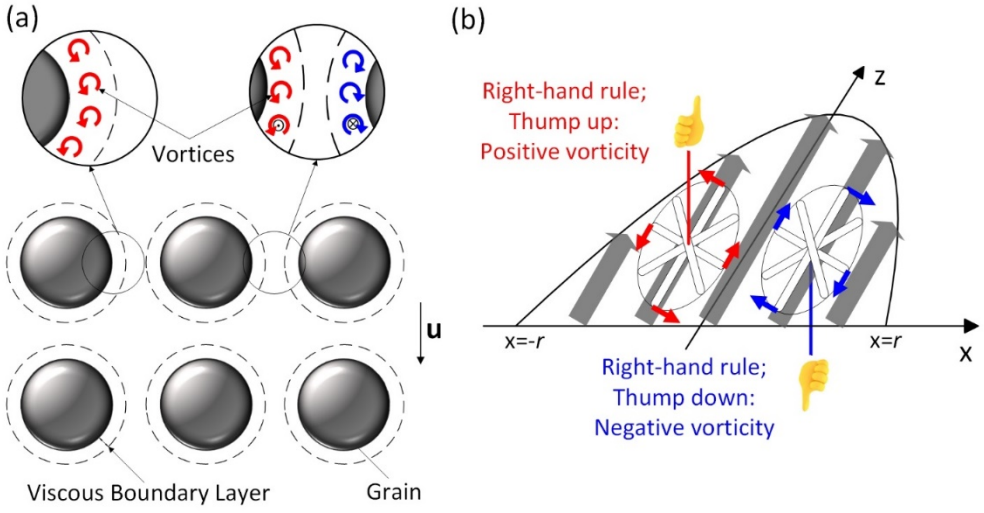

Figure 6. 1 (a) Schematic of the vortices in porous medium induced by the elastic waves; (b) vorticity direction determined by the right-hand rule.

We find that the frictional dissipation at pore-scale is controlled by the magnitude of vorticity at the pore wall where the vorticity is generated. The vorticity has its largest value at the pore wall and becomes smaller and smaller toward the interior of the fluid (Figure 6. 2).

Such vorticity dissipation increasing with the escalating frequency not only affects the overall rigidity but also becomes an important source of the wave attenuation in high frequencies, which cannot be ignored.

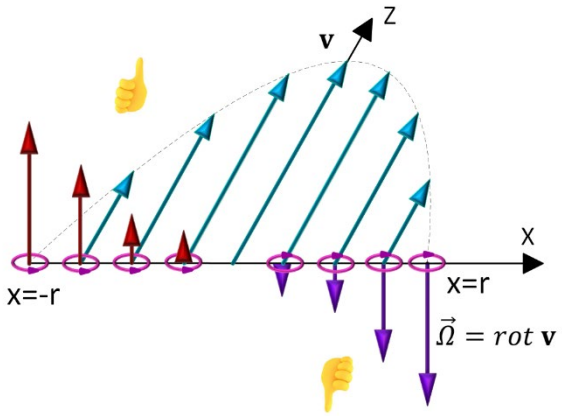

Figure 6. 2 Schematics of the profiles of the viscous fluid velocity v and the corresponding vorticity $\vec{\Omega}$.

The pore scale flow velocity and the vorticity dissipation are the functions of frequency and pore size. Although an average pore size is often conceived, it might be too simplified and unrepresentative for the natural sedimentary rock with broadband pore sizes and multiple peaks on their pore volume distribution. Thus, accurate values of flow velocity and friction require the average computation based on pore size distribution data, which can be measured by nuclear magnetic resonance (NMR) or mercury intrusion porosimetry (MIP) experiments (Xiao et al., 2016). The pore size distribution effects on the vorticity dissipation and, therefore, the wave dispersion and attenuation are explored in this paper.

In addition, the wettability of the porous media can also affect the wave dispersion and attenuation, which has been studied experimentally (Shakouri et al., 2019; Wang et al., 2015) and theoretically (Li et al., 2020a; Li et al., 2020b). Due to the vast interfacial area of fluid and solid contact, wettability plays a crucial role in porous media. In general, the wettability effect could be proxied by the slip boundary condition quantified by the slip length. It is based on the fact that the non-wetting micro-fluid parcel tends to slip on the hydrophobic pore wall where the intermolecular potential between the fluid and solid is weaker than that in wetting fluid saturated condition (Barrat, 1999; de Gennes, 2002; Granick et al., 2003). This particular feature renders that the flow velocity is higher and the friction on the solid boundary is lower for the non-wetting fluid than these for the wetting fluid under the excitement of the passing

wave (Barrat, 1999; Cottin-Bizonne et al., 2005; Huang et al., 2008; Ramos-Alvarado et al., 2016).

The structure of this chapter is as follows. Firstly, we derive the analytical forms of the pore-scale flow velocity and vorticity of oscillating flow in the single pore and the porous media context, respectively. We further use numerical examples to visualize and compare the velocity and vorticity field in various frequencies and pore sizes. Secondly, the wettability effect is considered by using the apparent slip model wherein the frequency-dependent viscosity is adopted for slip boundary conditions. Further, the effective viscosity is computed to account for the combined effect of vorticity dissipation, slip boundary and pore size distribution. We numerically exam the model and compare it with the Biot model on two sandstone samples with different pore size distributions. Lastly, we check the experimental results, which can be qualitatively explained by our model.

6.2. Pore-scale Vorticity Diffusion in Porous Media

6.2.1. Vorticity Diffusion and the Frictional Dissipation

The oscillatory flow model in an infinitely long cylindrical tube has been derived by Biot (1956b). For a cylindrical tube with radius r and saturated by viscous fluid oscillates with viscosity μ_{f} and density ρ_{f} in the z direction, the Navier-Stokes equation is,

$$T\rho_{\mathrm{f}}\frac{\partial \mathrm{v}}{\partial t} = F_b + \mu_{\mathrm{f}}\nabla^2\mathrm{v}. \tag{6.3}$$

$F_b = -\nabla\mathrm{P} - T\rho_{\mathrm{f}}\frac{\partial \mathrm{u}}{\partial t}$ is equivalent to external volume (body) force. The term ∇P is the pressure gradient and u is the velocity of the solid. Here we start with this simple model with Fourier sign $exp(-\mathrm{i}\omega t)$. The velocity of the fluid with respect to the solid is,

$$\mathbf{v}(\omega, x) = \mathbf{u_p}\left[1 - \frac{J_0(kx)}{J_0(kr)}\right]. \tag{6.4}$$

The $\mathbf{u_p}$ is the potential flow independent of viscosity and the J_0 () is zero-order Bessel function. The $\mathrm{k} = \sqrt{\mathrm{i}\omega/D_0}$ is the wavenumber of the diffusive viscous wave with diffusivity $D_0 = \mu_{\mathrm{f}}/T\rho_{\mathrm{f}}$, which equals to the kinematic viscosity scaled by the tortuosity. The thickness of the viscous boundary layer is known as viscous skin depth, which is the penetration depth of the vorticity in the oscillatory viscous flow. For the infinite long cylindrical tube, it is,

$$\delta_0(\omega) = \frac{1+\mathrm{i}}{\mathrm{k}} = \sqrt{2D_0/\omega}\ . \tag{6.5}$$

By substituting equation (4) back into equation (3) and taking the curl operating on both sides, the potential flow term vanishes identically and we obtain the diffusion equation,

$$\frac{\partial\vec{\Omega}}{\partial t} = D_0\frac{\partial^2\vec{\Omega}}{\partial x^2}\ . \tag{6.6}$$

where the vorticity

$$\vec{\Omega}(\omega, x) = rot\ (\mathbf{v}) = k\frac{J_1(kx)}{J_0(kr)}\cdot\mathbf{u_p}\ . \tag{6.7}$$

For the dynamic motion of the viscous fluid in the porous media, equation (4) is still applicable by using the wave number of the slow S- wave k_4 to replace that of the ordinary viscous wave k. Thus, the relative fluid velocity becomes

$$\mathbf{v}(\omega, x) = \left[1 - \frac{J_0(k_4x)}{J_0(k_4r)}\right]\cdot\mathbf{u_p}\ . \tag{6.8}$$

The corresponding vorticity is

$$\vec{\Omega}(\omega, x) = rot\ (\mathbf{v}) = k_4\frac{J_1(k_4x)}{J_0(k_4r)}\cdot\mathbf{u_p}\ . \tag{6.9}$$

which obeys the diffusion equation,

$$\frac{\partial\vec{\Omega}}{\partial t} = D_p\frac{\partial^2\vec{\Omega}}{\partial x^2}\ . \tag{6.10}$$

If we consider the planar wave solution for the vorticity as $\vec{\Omega} = \vec{\Omega}_0 e^{i(k_4x-\omega t)}$, we obtain its frequency dependent diffusivity as

$$D_p(\omega) = \frac{i\omega}{k_4^2}\ . \tag{6.11}$$

Therefore, the viscous skin depth for the porous media is,

$$\delta_p(\omega) \equiv \frac{1+i}{k_4} = \sqrt{2D_p/\omega}\ . \tag{6.12}$$

Owing to the oscillatory motion of the viscous fluid, the viscous boundary cannot maintain a stable near-to-pore layer as it is in the steady flow, which renders the viscous skin depth to be a complex value. At low-frequency limit, δ_p has a finite value,

$$\delta_p^0 = \delta_p(\omega \to 0) = \frac{1+i}{k_4^0}\ . \tag{6.13}$$

where $k_4^0 \equiv k_4(\omega \to 0) = i\sqrt{\frac{\phi}{\kappa_o T d_\mathrm{f}}}$.

Because the vorticity is mainly confined within the viscous skin depth, we can define a quantity to represent the magnitude of the pore-scale vortices, which equals to the product of the vorticity and the viscous skin depth,

$$\vec{\Omega}_\delta(\omega, x) = \vec{\Omega} \cdot \delta_p \quad . \tag{6.14}$$

Since the symmetry of the cylindrical pore model, the vorticity $\vec{\Omega}(\omega, x) = rot\ (\mathbf{v}) = \frac{\partial \mathrm{v}}{\partial \mathrm{x}}$. Therefore, the viscous frictional stress τ is proportional to the vorticity at the pore wall.

$$\tau(\omega, r) = \mu_\mathrm{f} \cdot \left(\frac{\partial \mathbf{v}}{\partial \mathrm{x}}\right)\Big|_{x=r} = \mu_\mathrm{f} \cdot \vec{\Omega}\big|_{x=r} \quad . \tag{6.15}$$

Thus, at the pore wall interface, the magnitude of the pore-scale vortices defined by equation (6.14) is proportional to the pore-scale frictional dissipation caused by the vorticity, which is a function of frequency and the pore size. The normalized magnitude of the interface vortices is,

$$\Omega_i(\omega, r) = \left(\vec{\Omega}_\delta\big|_{x=r}\right)/\mathbf{u_p} = k_4 \frac{J_1(k_4 r)}{J_0(k_4 r)} \quad . \tag{6.16}$$

6.2.2. The Critical Frequency and The Critical Pore Size

The critical frequency arises if the wavelength of the slow S-wave is on the order of the pore size when maximum interaction between the propagation waves and the diffusive wave (slow S-wave) occurs (Müller and Sahay, 2011c). Li et al. (2020c) find that the pore-scale critical frequency for each pore size is the frequency when the half of the slow S-wavelength is comparable to the pore opening ($\lambda \approx 4r$), which can be calculated by substitute the wave number k_4 into $k_4 = 2\pi/\lambda$.

$$f_c = \frac{2\mu_\mathrm{f}}{T\rho_\mathrm{f}}\sqrt{\frac{4\pi^2}{\lambda^4} + \frac{\phi/(\kappa_0 T d_\mathrm{f})}{\lambda^2}} \quad . \tag{6.17}$$

It convergences to the linear function at high frequencies ($\omega \gg \omega_B$),

$$f_c = \frac{4\pi\mu_\mathrm{f}}{T\rho_\mathrm{f}\lambda^2} \quad . \tag{6.18}$$

When this critical frequency coincides with the Biot characteristic frequency $f_c = \omega_B/2\pi$, the corresponding critical pore size (i.e. radius) can be derived,

$$r_B = c\pi\sqrt{\frac{\kappa_0}{2\phi}}\ , \tag{6.19}$$

where the constant parameter $c = \sqrt{m_s + \sqrt{1 + m_s}}$ and the $m_s = 1 - m_{\mathrm{f}} = (1-\phi)\rho_{\mathrm{s}}/[\phi\rho_{\mathrm{f}} + (1-\phi)\rho_{\mathrm{s}}]$ is the solid mass fraction. For the common sedimentary rock saturated by oil or water $c \approx 3/2$.

6.2.3. Numerical Examples of The Pore-scale Vorticity and Flow Velocity Field

In this section, we use numerical examples to exam the pore-scale vorticity and flow velocity field. A porous medium (i.e. sandstone) is considered with grain density $\rho_s = 2650\ \mathrm{kg/m^3}$, permeability $k_0 = 200mD$, and porosity $\phi = 0.2$ and saturated by water with density $\rho_{\mathrm{f}} = 1000\mathrm{kg/m^3}$ and viscosity $\mu_{\mathrm{f}} = 1$ cP. The tortuosity is calculated by $T = 1/2\,(1 + 1/\phi) = 3$.

The normalized magnitude of interface vortices $\Omega_i(\omega, r)$, which represent the pore-scale vorticity dissipation are plotted in Figure 6. 3. The pore-scale frequency f_c coincides the highest values in the imaginary part of the normalized magnitude of interface vortices ($\mathrm{Im}(\Omega_i)$). The Biot frequency f_B and the critical pore radius r_B divide Ω_i into four quadrants:

I: large pores ($r > r_B$) at high frequencies ($f > f_B$): high magnitude of vortices with largest peak values at frequencies closed to Biot frequency f_B;

II: large pores ($r > r_B$) at low frequencies ($f < f_B$): high magnitude of vortices with largest peak values at frequencies closed to Biot frequency f_B;

III: small pores ($r < r_B$) at low frequencies ($f < f_B$): low magnitude of vortices;

IV: small pores ($r < r_B$) at high frequencies ($f > f_B$): transition of vortices magnitude from low level to a high level at pore-scale critical frequency f_c.

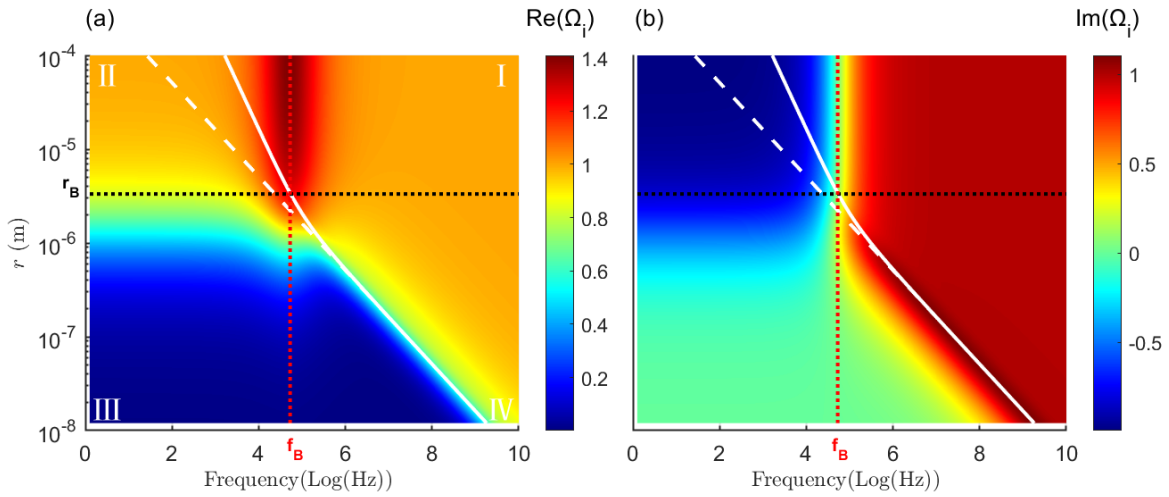

Figure 6. 3 Real part and (b) imaginary part of the normalized magnitude of interface vortices $\Omega_i(\omega, r)$ are function of frequency and pore size, which are plotted at log-log scale. The pore-scale critical frequency f_c defined by equation (6.17) is plotted as a solid white line and its linear asymptotic value defined by equation (6.18) are plotted as a white dash line. The Biot frequency $f_B = \omega_B/2\pi$. and the critical pore radius r_B defined by equation (6.19) are plotted in red and black dash lines, respectively.

We further compare the pore-scale relative flow velocity **v** normalized by the potential flow and the corresponding normalized $\vec{\Omega}_\delta$ in the single cylindrical tube (Biot, 1956b) and the porous media on the frequency domain (Figure 6.4 and 6.6). Two different pore sizes are checked. One pore size is r $= \delta_p^0 < r_B$ representing the maximum pore size in which the viscous flow is dominated and at low frequency limit. The other pore size r $= 5\sqrt{\kappa_0/\phi} > r_B$ is considered as the effective capillary radius in the porous medium (Blunt, 2017; Dullien, 2012). It shows that the viscous skin depths (black dashed lines) in the porous medium (e.g. sandstone) have a finite value rather than an infinitely large value for the single infinite long cylindrical tube at the low-frequency limit.

For the small size pores ($r \leq r_B$), the vorticity in porous medium retains a low level at the low-frequency range ($f < f_B$) due to the underdevelopment of the viscous flow (Figure 6.5). However, the vorticity increases rapidly at the high-frequency range ($f > f_B$) though it is restricted within the viscous skin, which becomes much smaller than the pore size. The vorticity vector obeys the right-hand rule and has the opposite sign on the two sides (Figure 6.1 and 6.2), however, the vorticity is axial-symmetry in the three dimensions (Figure 6.5d). At the same time, the velocity profile gradually deviates from the parabolic shape and evolves to be a flange shape in the high-frequency range (Figure 6.5b).

For the large size pores ($r \gg r_B$) in the porous medium, the viscous skin depth can only occupy a portion of the pore space so that the potential flow dominates the bulk fluid flow in any frequency, which is different from the scenario in the single cylindrical pore (Figure 6.6). The viscous skin depth reaches the highest value at the Biot frequency f_B when the magnitude of the vortices $\vec{\Omega}_\delta$ also comes to the peak (Figure 6.7). The velocity profile is parabolic shape at the low-frequency range ($f < f_B$) but becomes flange shape at the high-frequency range ($f > f_B$) (Figure 6.7a, b).

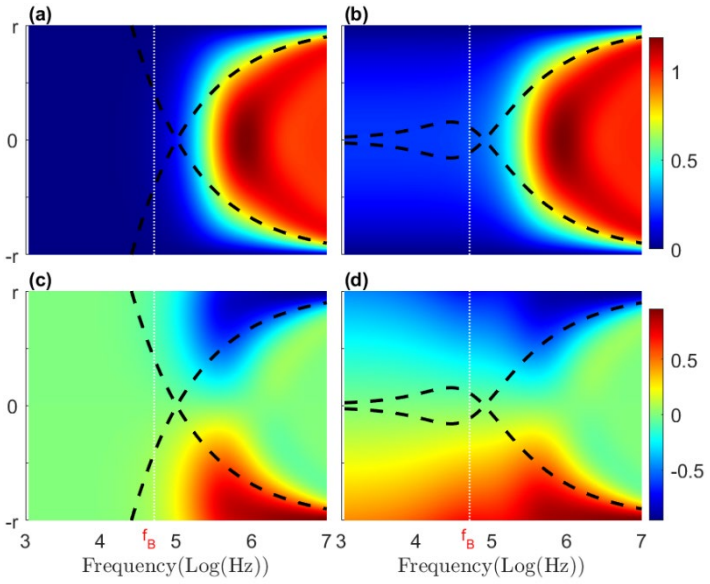

Figure 6. 4 The pore-scale profiles of normalized **v** in (a) cylindrical tube and (b) porous medium; and pore-scale profiles of the corresponding normalized $\vec{\Omega}_\delta$ in (c) cylindrical tube and (d) porous medium at frequency domain. The viscous skin depths are marked as black dashed lines. The crossover frequency $f_B = \omega_B/2\pi$ are marked as white dashed lines. The pore radius $r = \delta_p^0$.

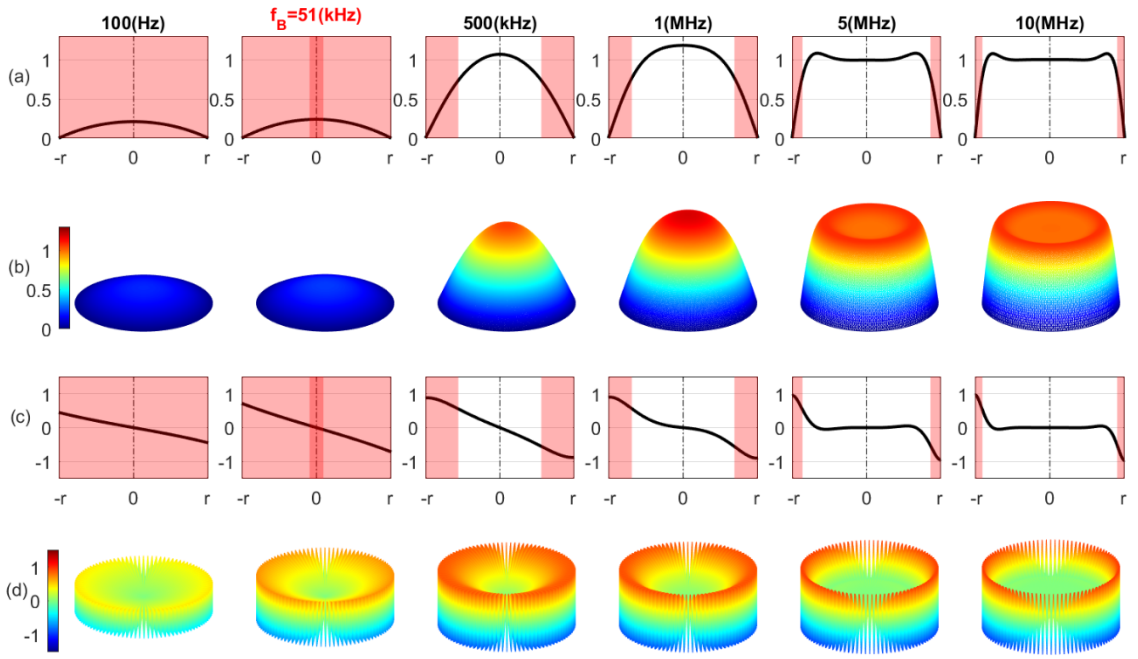

Figure 6. 5 (a) the pore-scale profiles of normalized v in a porous medium at 6 different frequencies and (b) the corresponding 3D plot; (c) the pore-scale profiles of normalized $\vec{\Omega}_\delta$ in porous medium at 6 different frequencies and (d) the corresponding 3D plot; The viscous skin depths are marked as light red shadings. The pore radius $r = \delta_p^0$.

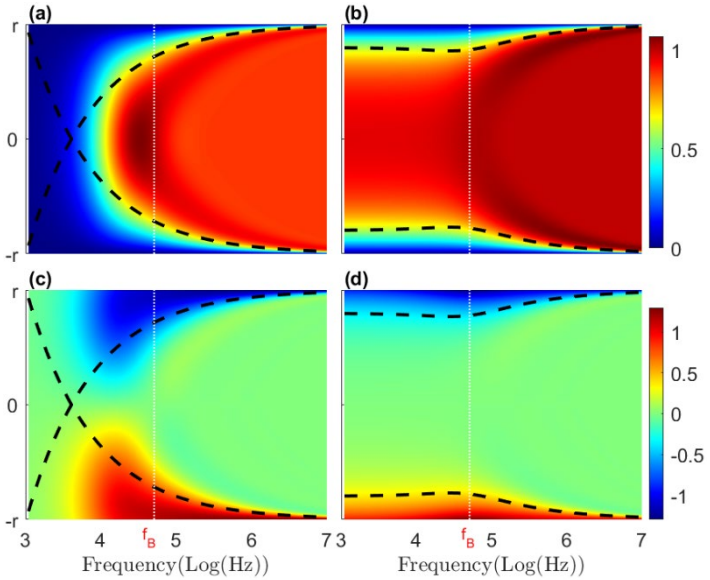

Figure 6. 6 The pore-scale profiles of normalized v in (a) cylindrical tube and (b) porous medium; and pore-scale profiles of the corresponding normalized $\vec{\Omega}_\delta$ in (c) cylindrical tube and (d) porous medium at frequency domain. The viscous skin depths are marked as black dashed lines. The crossover frequency $f_B = \omega_B/2\pi$ are marked as white dashed lines. The pore radius $r = 5\sqrt{\kappa_0/\phi}$.

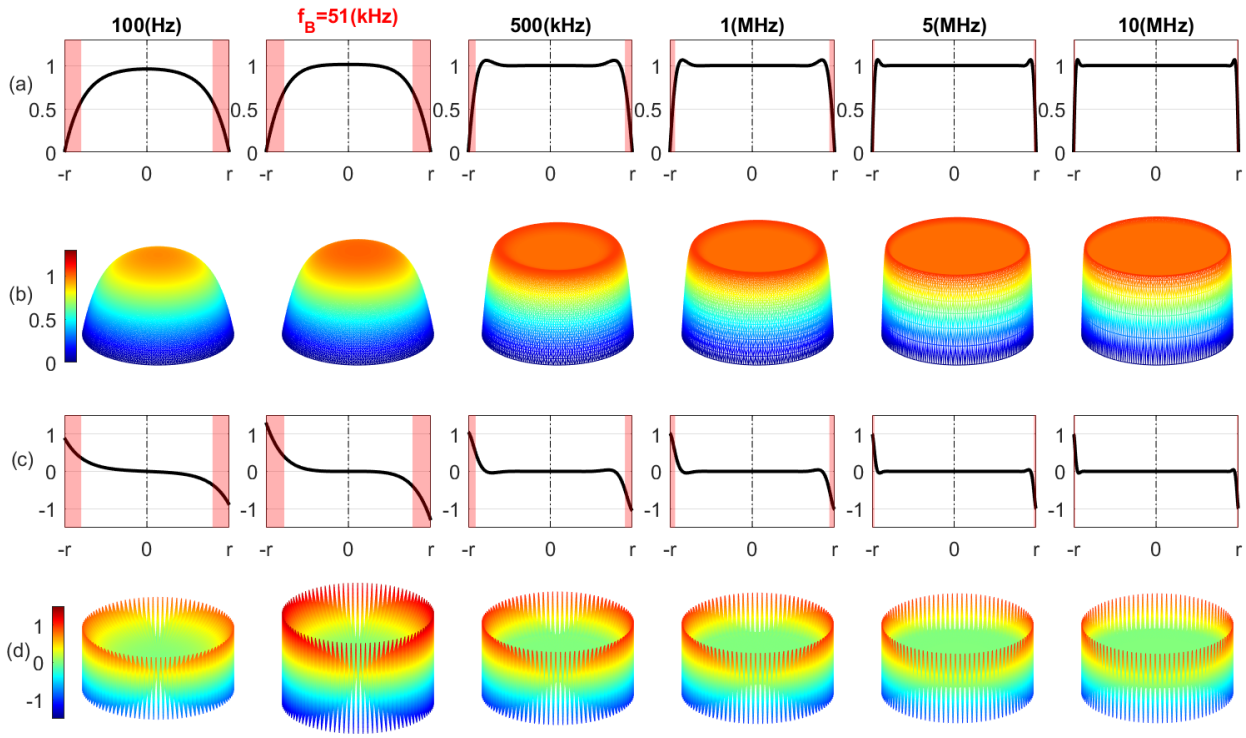

Figure 6. 7 (a) the pore-scale profiles of normalized v in sandstone at 6 different frequencies and (b) the corresponding 3D plot; (c) the pore-scale profiles of normalized $\vec{\Omega}_\delta$ in porous medium at 6 different frequencies and (b) the corresponding 3D plot; The pore radius $r = 5\sqrt{\kappa_0/\phi}$.

6.3. Effective Viscosity for the Porous Media with Broadband Pore Size Distribution and Slip Boundary Condition

6.3.1. Viscosity Correction Based on Pore Size Distribution Data

In order to describe the viscous frictional effect in the porous media at high frequencies, Biot (1956b) workout a viscosity correction factor by analysis of the ratio of the average velocity v_i and the frictional force h_i at pore-scale, which could be considered as a frequency and pore size-dependent frictional coefficient.

$$B_{Biot} = \frac{v_i(\omega,r)}{h_i(\omega,r)} \quad . \tag{6.20}$$

In the Biot model, all pores are considered to have the same characteristic pore size $r = a$. However, as the analysis in section 6.4, the contribution of the pores with various pore sizes have important differences. Thus, for the porous medium in which the pore size is distributed in a wide range, pore size distribution should be considered so that a distribution of friction

would then occur between pores as the frequency varies with a corresponding distribution in the velocity pattern.

The pore-scale average velocity of the oscillatory-forced fluid flow in the porous medium based on equation (6.8) is:

$$v_i(\omega, r) = \left[1 - \frac{2J_1(k_4 r)}{k_4 r J_0(k_4 r)}\right] \cdot \mathbf{u_p} \ , \tag{6.21}$$

and the frictional force based on equation (6.15) is:

$$h_i(\omega, r) = 2\pi r \mu_f \tau = 2\pi r \mu_f k_4 \frac{J_1(k_4 r)}{J_0(k_4 r)} \cdot \mathbf{u_p} \ . \tag{6.22}$$

However, the volume-averaged velocity and the frictional force are not only frequency dependent but also pore size distribution dependent. For the porous medium with a broadband pore size distribution (each pore size $r_i \in (r_{min}, r_{max})$ corresponds to an incremental porosity ϕ_i), their volume averaged values are,

$$\bar{v}(\omega, r, \phi_i) = \frac{\sum_{r_{min}}^{r_{max}} \phi_i v_i}{\phi} \ , \tag{6.23}$$

$$\bar{h}(\omega, r, \phi_i) = \frac{\sum_{r_{min}}^{r_{max}} \phi_i h_i}{\phi} \ . \tag{6.24}$$

Therefore, the corresponding frictional coefficient becomes,

$$B_\omega(\omega, r, \phi_i) = \frac{\bar{v}(\omega, r, \phi_i)}{\bar{h}(\omega, r, \phi_i)} \ . \tag{6.25}$$

In the low-frequency limit, its value is,

$$B_0(r, \phi_i) = \frac{\bar{v}_0(r, \phi_i)}{\bar{h}_0(r, \phi_i)} \ . \tag{6.26}$$

where

$$\bar{v}_0 = \frac{\sum_{r_{min}}^{r_{max}} \phi_i v_i^0}{\phi} \ , \tag{6.27}$$

$$\bar{h}_0 = \frac{\sum_{r_{min}}^{r_{max}} \phi_i h_i^0}{\phi} \ , \tag{6.28}$$

$$v_i^0 = \left[1 - \frac{2J_1(k_4^0 r)}{k_4^0 r J_0(k_4^0 r)}\right] \cdot \mathrm{u_p} \ , \tag{6.29}$$

$$h_i^0 = 2\pi r \mu_f k_4^0 \frac{J_1(k_4^0 r)}{J_0(k_4^0 r)} \cdot \mathrm{u_p} \ . \tag{6.30}$$

The viscosity correction factor $\mathrm{F}(\omega, r, \phi_i)$ is defined as the ratio of the frictional coefficient and its value at zero frequency limit, which measures the deviation from Poiseuille flow friction as a function of frequency.

$$\mathrm{F}(\omega, r, \phi_i) = \frac{B_\omega}{B_0} \ . \tag{6.31}$$

6.3.2. Effective Viscosity with Slip Boundary Condition

The velocity and vorticity derived above are based on the no-slip boundary condition; however, for a non-wetting fluid situated porous medium, the slip boundary condition is appropriate. The viscosity with slip boundary condition has been achieved by using the apparent slip model (Li et al., 2020b; Li et al., 2020c),

$$\mu_{\mathrm{f}}^{slip}(\omega, b) = \frac{\mu_{\mathrm{f}}}{1+\frac{b}{\delta_p}} \leq \mu_{\mathrm{f}} \ . \tag{6.32}$$

In the low-frequency limit, $\mu_{\mathrm{f}}^{slip}(\omega \to 0) = \mu_{\mathrm{f}} / \left(1 + \frac{b}{\delta_p^0}\right)$ results in the increase of the effective static permeability,

$$\kappa_0^{slip} = \kappa_0 \left(1 + \frac{b}{\delta_p^0}\right) \geq \kappa_0 \ . \tag{6.33}$$

where b is the slip length whose value is dependent on the wettability of the porous medium to the saturated fluid. In general, the slip length and contact angle obeys the quasi-universal relationship $b \propto (1 + cos\theta)^{-2}$ (Huang et al., 2008; Ortiz-Young et al., 2013) i.e. the strong wetting fluid has zero slip length $b = 0$ corresponding to the hydrophilic non-slip boundary condition and non-wetting fluid has finite slip length $\mathrm{b} > 0$ correspondings to the hydrophobic slip boundary condition.

It is worth noting that the increase of the effective static permeability is caused by the decrease of the viscosity with slip boundary condition so that the component $\left(1 + \frac{b}{\delta_p^0}\right)$ related to the slip boundary condition should not be included in the calculation of the fluid mobility of the fluid $\left(\kappa_0 / \mu_{\mathrm{f}}^{slip}\right)$, otherwise, the slip boundary condition would be overused.

By using the viscosity μ_{f}^{slip} defined in equation (6.32) to replace the ordinary viscosity μ_{f} in the equation (6.31) and the sub-equations, one enables its feasibility for any kind of slip boundary condition. The effective viscosity, therefore, can be defined as,

$$\mu_{\mathrm{f}}^{eff}(\omega, r, \phi_i, b) = \mathrm{F} \cdot \mu_{\mathrm{f}}^{slip} \quad . \tag{6.34}$$

By using the effective viscosity for the slip boundary, we can further explore the wettability effect on the hydrodynamics of the wave-induced-fluid-flow and the attenuation and velocity of the elastic wave propagation.

6.4. The Solution of Velocity Dispersion and Attenuation in the Porous Media

The velocity dispersion is often referring to the discrepancies between the measured velocities of waves with different frequencies in the saturated porous medium. The dispersion occurred is due to the attenuation, which could be caused by the intrinsic attenuation of the rock matrix or the frictional attenuation of the viscous fluid. The wettability plays a role in the latter part of the attenuation and the corresponding dispersion. For two porous media with the same solid frame properties but saturated by different wetting fluids, the dispersion is mainly due to the frictional attenuation which is affected by the fluid slippage (wettability) based on our previous analysis. Therefore, the dispersion can be an indicator of wettability.

In order to incorporate the vorticity dissipation and slip boundary condition effect, the solution of the velocity and attenuation in the porous media with broadband pore size distribution can be calculated by equations (4.14) and (4.15) by using the effective viscosity μ_{f}^{eff} defined by equation (6.34). The compressional and shear moduli of the saturated porous media can be further calculated by,

$$\mathrm{M}_{sat} = V_p^2 \rho_b \quad , \tag{6.35}$$

$$\mu_{sat} = V_s^2 \rho_b \quad , \tag{6.36}$$

where $\rho_b = \rho_s + \phi(\rho_f - \rho_s)$ is the bulk density of the saturated porous medium.

The dispersion of velocity and modulus are defined as,

$$\Delta \mathrm{V}_{ph} = \frac{V_{ph}(high\ frequency) - V_{ph}(low\ frequency)}{V_{ph}(low\ frequency)} \tag{6.37}$$

$$\Delta \mathrm{M}_{sat} = \frac{\mathrm{M}_{sat}(high\ frequency) - \mathrm{M}_{sat}(low\ frequency)}{\mathrm{M}_{sat}(low\ frequency)} \tag{6.38}$$

$$\Delta \mu_{sat} = \frac{\mu_{sat}(high\ frequency) - \mu_{sat}(low\ frequency)}{\mu_{sat}(low\ frequency)} \tag{6.39}$$

Since the shear wave only transmits in the solid phase, we can use the shear modulus of the dry porous media as an approximation of the shear modulus of the saturated porous media with the low frequency wave.

6.5. Results and Application

6.5.1. Pore Size Distribution Data

To exam the theory of wettability and pore size distribution dependent wave propagation, we numerically construct two kinds of pore size distribution (PSD) data as demonstrated in Figure 6.8: one (#1) PSD contains more portion of large size pores and a small portion of small size pores; the other one (#2) PSD contains more portion of small size pores and a little portion of large size pores. The pore size range ($10^{-7}m < r_i < 10^{-4}m$) is selected to simulate the typical sandstone. The other parameters are used as in Table 6.1.

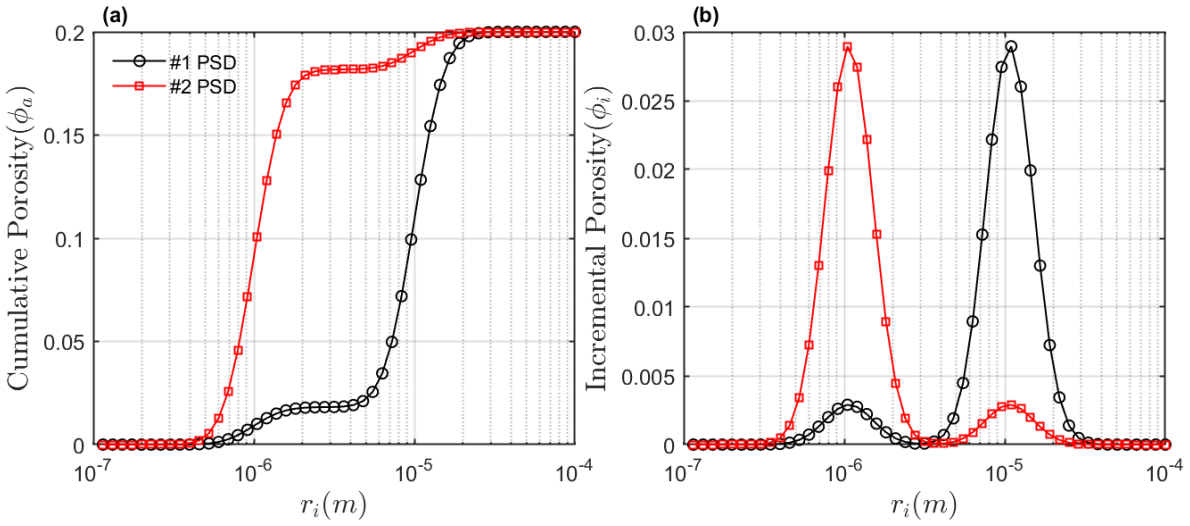

Figure 6. 8 (a) Cumulative porosity and (b) incremental porosity.

Table 6. 1 Parameters of brine-saturated sandstone.

Grain	Bulk modulus, K_s	35 Gpa
	Density, ρ_s	2650 kg/m^3
Matrix	Porosity, ϕ	0.2
	Permeability, κ_0	200mD
	Bulk modulus, K_d	15 Gpa
	Shear modulus, μ_d	12 Gpa
Brine	Bulk modulus, K_f	2.25 Gpa

	Density, ρ_f	1040 kg/m^3
	Viscosity, μ_f	1 cP

Remark:

- ✓ 1 cP=10-3 Pa·s; 1mD≈10-15 m2.
- ✓ Tortuosity is calculated by $T_\infty = \frac{1}{2}\left(1 + \frac{1}{\phi}\right)$.
- ✓ The slip length $b = \sqrt{\kappa_0/\phi}$ is selected for the slip boundary condition (non-wetting fluid saturation).

The effective viscosities are calculated based on Eq. (6.34) as in Figure (6.9) for the porous media with two different PSD, respectively. We note that the effective viscosity in the slip boundary condition is smaller than it in the non-slip condition, which is especially obvious in the high-frequency range. The #2 PSD with smaller size pores has seen slightly smaller effective viscosity than it in the #1 PSD in the same boundary condition.

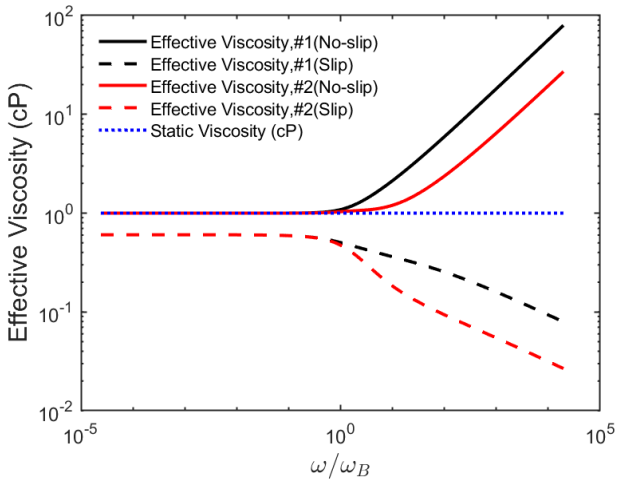

Figure 6. 9 The effective viscosity in the porous media with two kinds of pore size distributions (PSD) and different slip boundary conditions.

6.5.2. Wave Attenuation and Velocity Dispersion

The velocities and the attenuation (1/Q) of P- and S-waves are calculated for the two PSDs and the corresponding slip boundary condition in Figure (6.10). It is clear that the slip length only affects the step transition of the phase velocities in the intermediate frequency, however, does not affect the lower and upper velocity bounds which correspond to phase velocities at the low and high-frequency limits, respectively. In the low-frequency limit, the velocity of fast P- wave and S- wave agree with the predictions of Gassmann's theory. The two kinds of P- waves and the S- wave have a similar pattern that the velocities increase if the slip length/hydrophobicity increase, which can qualitatively explain the recent experiment result (Shakouri et al., 2019). However, the extent of the influence of the slippage on the velocity is dependent on the inherent

dispersion of the porous medium (i.e. the difference between the high and the low limit velocities). On the other hand, the impact of the pore size distribution on the velocity is not significant.

The attenuation of the wave is quantified by the dissipation factor $1/Q$, which is the reciprocal quality factor (Figure 6.10b,d). The slip boundary promotes the out-of-phase motion at the low frequency where the attenuation is higher than it in the non-slip condition. But the vorticity dissipation and friction decrease due to the slip boundary so that the attenuation becomes lower value quickly at high frequency. For the same boundary condition, the attenuation in the #1 sample where large size pores are rich is significantly higher than it in the #2 sample where small size pores are dominated. However, either of them has higher attenuation than the predictions of Biot theory (blue lines). This agrees with the analysis of the magnitude of interface vortices, which represent the vorticity dissipation, as shown in Figure 6.3, where vorticity dissipation is more prevalent in the relatively large pores.

The slow P- wave as a diffusive wave is highly attenuated at the low frequency (Chandler and Johnson, 1981; Müller and Sahay, 2011b), which is still valid for any apparent slip condition. The fluid and solid frame conduct the out of phase motion in the slow P wave where the reduced effective viscosity aid the friction reduction so that the slip effect lowers the attenuation rapidly when the frequency increase (Figure 6.11). However, for the non-slip condition ($b = 0$), the attenuation becomes higher than the Biot prediction (blue lines) due to the vorticity dissipation at high frequencies.

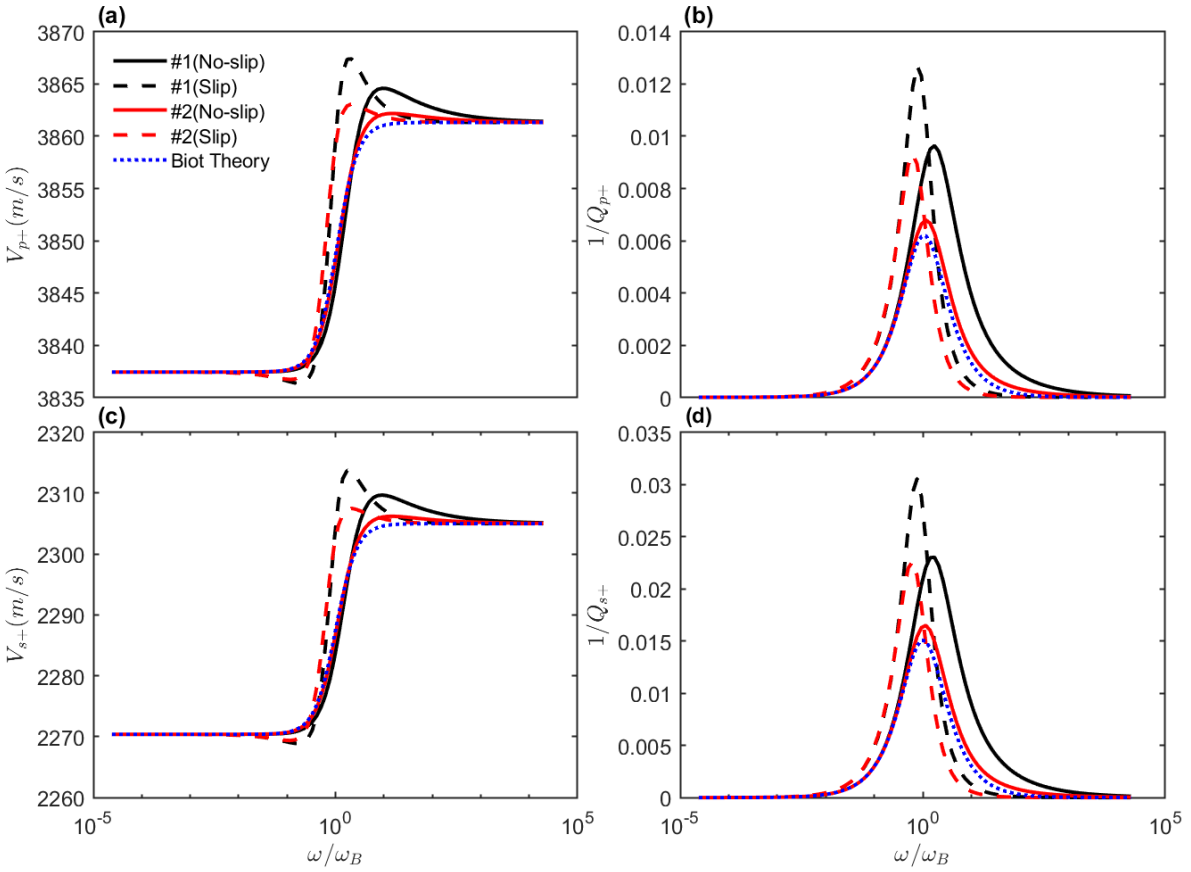

Figure 6. 10 The velocities (V) and the attenuation (1/Q) of P-wave (p+) and S-wave (s-) are compared in the porous medium with different PSD and wettability conditions. No-slip condition only has the vorticity loss only and slip condition has the vorticity loss plus the slip effect in the boundary layer.

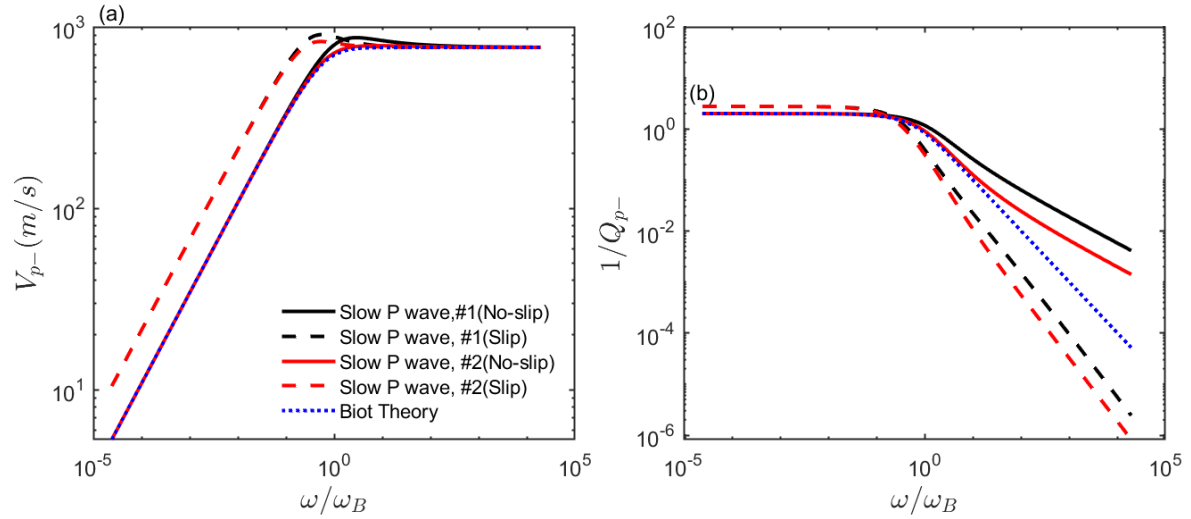

Figure 6. 11 The velocities and the attenuation (1/Q) of slow P-wave (p-) in the porous medium with different PSD and wettability conditions.

6.9.2. The implication in the prediction of wettability

The major discrepancies of the velocity between different boundary conditions occur in the area closed to the critical frequency ω_B. For the same frequency, the velocity difference of slip

boundary and non-slip boundary may not be big enough to be detected. However, if we use two or more detectors with more frequencies, as shown in Figure (6.12), the velocity differential or the velocity dispersion may be able to be used as an indicator of the slip boundary, therefore, the indicator of the wettability. For example, for two frequencies signals on the two sides of the critical frequency, the P-wave velocity dispersion of the slip boundary (hydrophobic) condition ΔV_p^{slip} is always higher than it in the non-slip boundary (hydrophilic) condition ΔV_p. This principle is also applicable to the S-wave. The combined dispersion of P- and S-waves, either velocities or moduli (i.e. cross-plot), can further support the reliable wettability determination.

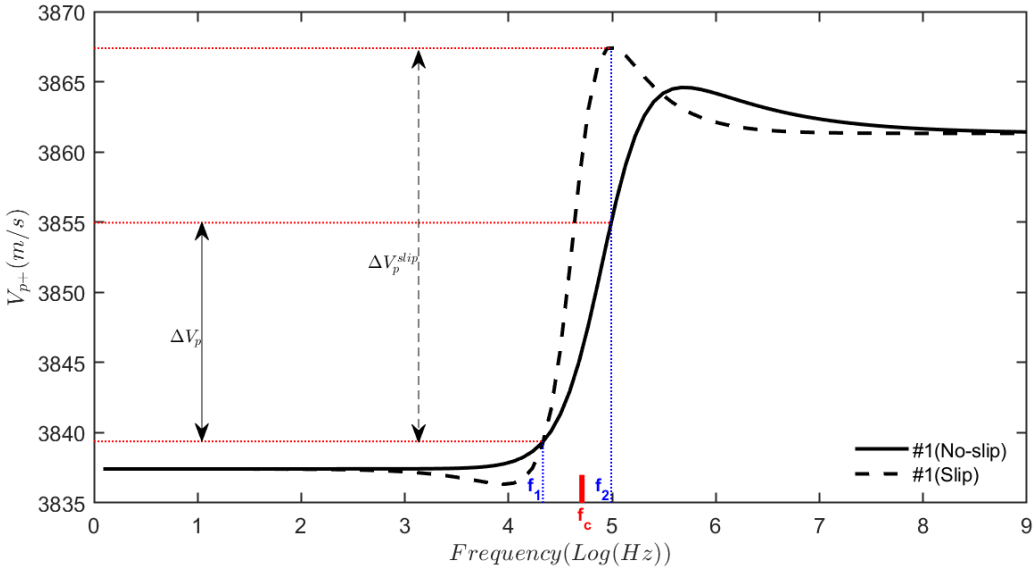

Figure 6. 12 The velocity dispersion is an indicator of different slip boundary conditions (wettability). The hydrophobicity promotes a higher dispersion than it in the hydrophilic condition.

6.5.3. Experimental Validation of Natural Sedimentary Rock

Based on the theoretical analysis and the numerical example, we figure out that the combined P- and S-wave dispersion can possibly be used for wettability estimation. To validate the method for the real porous media, we measured the P- and S-wave velocities in various natural sedimentary rocks (Bentheimer sandstone, Berea sandstone and Indiana carbonate) and with different wettability conditions. The saturation fluids water and decane are used. The saturation conditions are specified in Table 6.2.

The dispersions of the moduli are calculated based on equations (6.37-6.39), and their cross-plots are demonstrated in Figure (6.13). We can see that the measured dispersion with non-wetting saturation (hydrophobic condition) is generally higher than its value in the wetting saturation (hydrophilic condition), which is especially true for the rocks with low clay contents (i.e. Bentheimer sandstone and Indiana carbonate).

The dispersion data points can be segmented by the dash lines in different groups to determine the wetting (blue points) and non-wetting conditions (red points) in the cross-plots (Figure (6.13)). In this way, the wettability can be determined from the measurement of the dispersions. However, for Berea sandstone, such segmentation is more challenging. It is because that the clay content in the Berea sandstone is relatively high, and its impact compensates for the wettability impact on the dispersion.

In the oil field, the wetting fluid (e.g. water) tends to spread and cover the solid minerals, while the non-wetting fluid (e.g. oil) is isolated by the wetting fluid and prevented from direct contact with the solid. During the wave passing, the non-wetting fluid tends to flow over the wetting fluid, which is a slip boundary condition. Therefore, the proposed method can also be applicable for the in-situ wettability determination in the oil reservoir.

Table 6. 2 Saturation condition in the natural sedimentary rocks with different wettability.

No.	Rock type	Wettability condition	Saturated fluid	Boundary Condition
1	Bentheimer sandstone	Hydrophilic	Water (wetting fluid)	No-slip
2	Bentheimer sandstone	Hydrophobic	Decane (wetting fluid)	No-slip
3	Bentheimer sandstone	Hydrophilic	Decane (non-wetting fluid)	Slip
4	Bentheimer sandstone	Hydrophobic	Water (non-wetting fluid)	Slip
5	Berea sandstone	Hydrophilic	Water (wetting fluid)	No-slip
6	Berea sandstone	Hydrophobic	Decane (wetting fluid)	No-slip
7	Berea sandstone	Hydrophilic	Decane (non-wetting fluid)	Slip
8	Berea sandstone	Hydrophobic	Water	Slip

			(non-wetting fluid)	
9	Indiana carbonate	Hydrophilic	Water (wetting fluid)	No-slip
10	Indiana carbonate	Hydrophobic	Decane (wetting fluid)	No-slip
11	Indiana carbonate	Hydrophilic	Decane (non-wetting fluid)	Slip
12	Indiana carbonate	Hydrophobic	Water (non-wetting fluid)	Slip

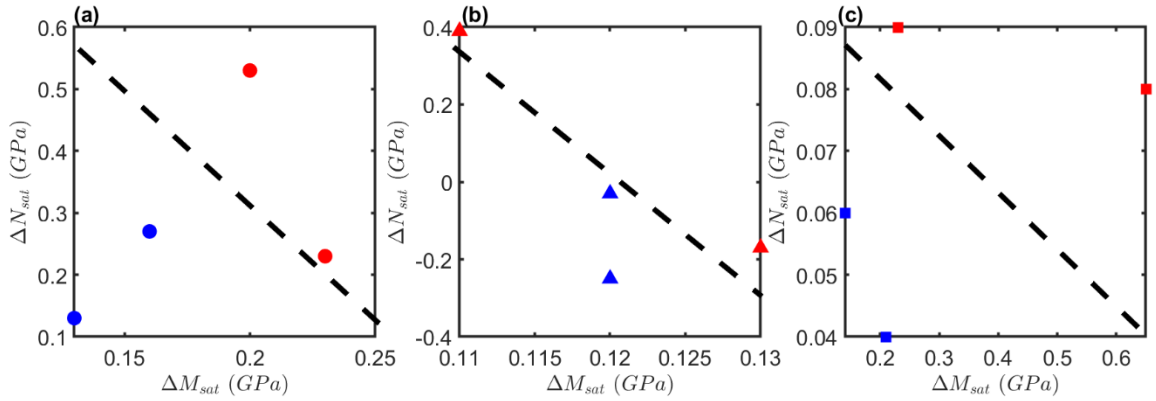

Figure 6. 13 The crossplot of the dispersions of compressional wave moduli and shear moduli for (a) Bentheimer sandstone, (b) Berea sandstone and (c) Indiana carbonate. The red and blue data points are from porous media saturated by non-wetting fluid and wetting-fluid, respectively.

6.6. Discussion

The viscous skin depth concept has been widely used in acoustical physics in the porous media saturated by fluid (Gurevich, 2002; Johnson et al., 1987; Murphy III et al., 1986). However, the most common viscous skin depth defined by equation (6.5) is derived by the analysis of the oscillatory flow above an infinite large flat plane (T=1) (Landau and Lifshitz, 1987) which is unrepresentative for the torturous pore network in the porous media context.

To tackle this problem, Biot (1956b) attempts using a sinuosity factor multiplying the angular frequency to give the weight of the unparallel placement of the cylindrical tube with respect to the direction of wave propagation. For a similar reason, Johnson et al. (1987) use the tortuosity factor multiplying the fluid density in the macroscopic model. In fact, these two approaches serve the same purpose to introduce the impact of the tortuosity on the inertia term, which reduces the viscous skin depth (Figure (6.14)) and decreases the diffusivity of the viscous wave

(vorticity) (Figure 6.15). Sahay (2008) further proves such viscous wave at low frequencies in porous media is slow S- wave.

At the low frequencies ($f < f_B$), the slow S-wave is heavily damped whose frequency-dependent diffusivity defined by equation (6.11) increases when frequency increases (Figure 6.15); at the high frequencies ($f > f_B$), it becomes an ordinary viscous wave where the diffusivity is constant for no-slip boundary conditions but decreases along with the increasing frequency for the slip boundary condition. It is because the effective viscosity in the slip boundary decreases when frequency increases.

Correspondingly, the viscous skin depth in the porous media has finite value when $f < f_B$, reaches its peak at the critical frequency f_B and decreases along with increasing frequency when $f > f_B$. The viscous skin depth becomes smaller in the slip boundary condition consequently due to the reduced effective viscosity (Figure 6.14).

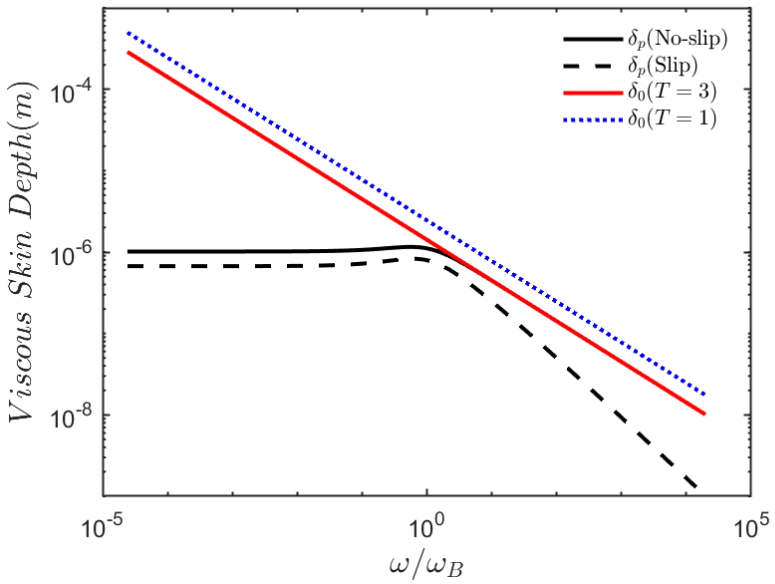

Figure 6. 14 Comparison of the viscous skin depth in the infinite long cylindrical tubes (T=1 and 3) and the sandstone (no-slip and slip boundary). The slip length $b = \sqrt{\kappa_0/\phi}$ is arbitrarily selected for the slip boundary condition.

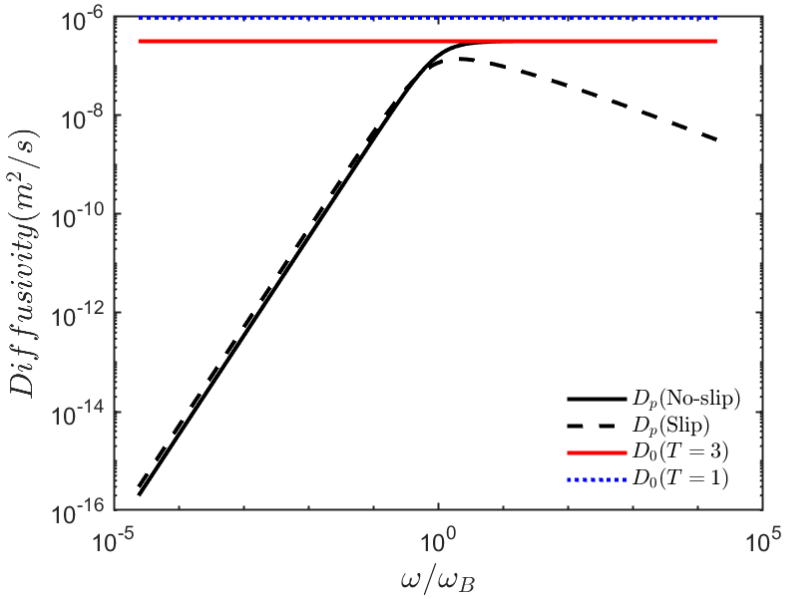

Figure 6. 15 Diffusivity of the vorticity diffusion in the infinite long cylindrical tube D_0 and the porous medium D_p.

The magnitude of the wettability impact on the velocity and the corresponding dispersion may not be detectable if the clay content in the rock (i.e. Berea sandstone) is relatively high, which may introduce a more complicated viscoelastic effect and distort the response to the wettability.

The

6.7. Conclusion

The vorticity dissipation and the slip boundary condition have been applied to the Biot mechanism for the wave propagation in the porous medium with broadband pore size distribution.

Vorticity dissipation related to the viscous loss due to the shear drag within the fluid comprises an important part of the frictional attenuation in the saturated porous medium. The extra energy dissipation occurs through the vorticity diffusion of the viscous fluid in the wave of slow S-wave, which draws the energy from propagating waves by the mode conversion. In this chapter, the slow S- wave is adopted into the oscillating flow model and explores the profiles of the velocity and the vorticity in the pore scale. The vorticity is mainly constrained within the viscous skin depth, which in the porous media context is finite in low frequencies and becomes much smaller than the pore size in the high frequencies.

The non-wetting fluid tends to slip on the solid boundary in the wave-induced-fluid-flow, which is a slip boundary condition and different from the basic assumption of the conventional Biot theory. Slip length represents the degree of the slippage and can be used as a proxy for the wettability or hydrophobicity degree, which plays a role in the wave motion. The slip boundary condition is treated by an apparent slip model where the fluid behaves less viscous inside the viscous boundary layer under the excitement of elastic waves. Wettability takes effect in the hydrodynamics of the microfluidics by the implementation of slip boundary where the effective viscosity is developed.

In general, the non-wetting fluid saturated porous material has higher phase velocities than the wetting fluid saturated one for all kinds of P- waves and S- wave in the intermediated frequencies but convergent to the same value in the low and high-frequency limits. The attenuation demonstrates a higher peak value, and the entire attenuation curve is constrained in a narrower frequency range for the slip BC (non-wetting saturation) compared to that of the no-slip BC (wetting saturation). The theoretical model developed has the potential to be applied in the prediction of wettability by measuring the velocity dispersion, which has been qualitatively validated by the experiments.

Chapter 7. Wettability-dependent Wave Velocities and Attenuation in Granular Porous Media

This chapter is based on below published conference papers and unpublished journal papers:

Li, J. X., Rezaee, R., Müller, T. M., Madadi, M., & Sarmadivaleh, M. (2020). Wettability dependent P-wave scattering and velocity saturation relation in granular medium. SEG Technical Program Expanded Abstracts 2020.

Li, J. X., Rezaee, R., Müller, T. M., Madadi, M., Ma, R., & Sarmadivaleh, M. (2021). Path dispersion of elastic waves in granular matter. Paper presented at the SEG/SPWLA 2020 Workshop: 7th Workshop on Porous Media: Structure, Flow and Dynamics, Virtual, 2–3 December 2020.

Li, J. X., Rezaee, R., Müller, T. M., Madadi, M., Ma, R., & Sarmadivaleh, M. (2021). Wettability-dependent Wave Velocities and Attenuation in Granular Porous Media. Submitted to *Geophysics.*

7.1. Introduction

Since granular porous media provide zones with high porosity and permeability that is important for freshwater aquifers, oil and gas production, and CO_2 geo-sequestration, there are wide genre of scientific interests in its properties especially the acoustic properties (Güven et al., 2017; Johnson and Jia, 2005; Liu and Nagel, 1992; Melosh, 1996; Moebius et al., 2012; Scott, 1996). In the context of groundwater exploitation and exploration geophysics, soft and unconsolidated sediments (e.g. soil and sand packings) in the subsurface are often conceptualized as fluid-saturated granular porous media. In particular, for the interpretation of sonic and seismic data it is important to understand their overall elastic properties, velocity dispersion, and attenuation mechanisms (Anthony and Marone, 2005; Daniels and Hayman, 2008; Dutta et al., 2010).

It is known that for porous media saturated with more than one fluid the wave velocity is not only dependent on the saturation, i.e., the volumetric proportion, but also dependent on the fluid distribution, i.e., the geometrical arrangement and length scales of fluid pockets. In this regard, there have been several experiments to study the velocity-saturation-relation (VSR) in various lithologic rocks with mixed liquid-gas saturation (Alemu et al., 2013; Cadoret et al., 1995; Lebedev et al., 2009; Lopes et al., 2014; Murphy III, 1984).

These VSR can be often constrained by the two end-member models of patchy and uniform saturation. They correspond to the upper bound and lower bound velocities described by the Gassmann-Hill (GH) and Gassmann-Wood (GW) equations, respectively (Toms et al., 2006). Similar experiments for granular media are not known. Even the applicability of the GW and GH bounds in partially saturated granular porous media remains unclear. Nonetheless, it is known that wave velocities are strongly different in dry and saturated granular media (Brunet et al., 2008; Griffiths et al., 2010; Job et al., 2008). Therefore, one can expect a pronounced signature of partial saturation to be present in granular media as well.

As far as velocity dispersion and attenuation in partially saturated rocks are concerned, there are multiple models to account for wave-induced-fluid-flow (WIFF), which is thought to be a relevant dissipation mechanism caused by the relative motion of solid and fluid (Ba et al., 2011; Dutta and Odé, 1979; Johnson, 2001; Lo et al., 2005; Mavko and Mukerji, 1998; Müller and Gurevich, 2004; Santos et al., 1990; Sun et al., 2018; White, 1975).

These models are used to interpret observed VSRs that do not follow either the GH or GW bounds, but show trends in between these bounds. These WIFF models also allow us to interpret the attenuation-saturation relation (ASR) (Liu et al., 2016; Qi et al., 2014).

While it is known that waves in granular media become attenuated, one may expect additional attenuation in partially saturated granular media (Brunet et al., 2008). However, the precise nature of WIFF in granular media is unknown, and therefore the applicability of one of the above-mentioned models remains questionable.

The presence of two fluids inevitably implies that two-phase flow concepts such as capillarity and wettability become relevant. For example, Qi et al. (2014) find that capillarity stiffening may result in higher wave velocities and accordingly modify the GW bound based on ideas earlier suggested by Nagy and Blaho (1994) and Tserkovnyak and Johnson (2003). Lo et al. (2017) discover the dynamic response of the water retention curve (relationship of capillary pressure and water saturation) during water drainage in unsaturated porous media under the acoustic excitations. The wettability as interfacial phenomena is thought to be a key factor controlling the spatial distribution and fluids and location of the fluid displacement, which could have a significant influence on the capillary pressure, relative permeability and water-flooding performance (Anderson, 1986b; Anderson, 1986e; Anderson, 1986f; Bultreys et al., 2016; Hu et al., 2017; Khishvand et al., 2017).

However, in none of the above studies, the wettability of the porous media to the saturated fluids has been considered. Ignoring the wettability impact on wave propagation may lead to errors and mis-interpretation of experimental and field test results. Therefore, in an attempt to understand the effect of wettability on waves velocities, we aim at experiments in an idealized porous medium, in which we can have full control of the wettability. For this purpose, we choose glass bead packings as a particular simple representation of a granular medium.

Although there are a lot of similarities between a granular porous medium and rigid porous medium and some poroelastic theories may be applicable to the granular medium, the grains in the granular medium have an additional degree of freedom compared to the solid frame of consolidated rigid porous media. In non-cohesive granular media under external stress, some grains are load-bearing, others not. This results in an inhomogeneous pattern of load-bearing grains, the so-called force chain networks. Force chain networks can be directly observed by

photo-elastic visualization experiments (Howell et al., 1999; Ladd and Reber, 2020; Owens and Daniels, 2011).

Since the contact force chain network bears the strongest stress on the direction of the compression, it dominates the mechanical properties of granular media, including the elastic response to the external disturbance such as acoustical perturbation (Sayers, 2021). When the granular medium is saturated by two immiscible fluids, the grain contacts are always occupied by the wetting fluid because of the capillary action, while the non-wetting fluid is forced into the relatively larger pores (Anderson, 1986a). Such a wettability-dependent spatial distribution of fluids is most likely to affect the structure of the force chain network. Different from the dry Hertzian contacts, the presence of the liquid bridges in the grain contacts (i.e. the water bridges in the water-wetting sample) induce the elastohydrodynamic collision of grains under ultrasonic frequency, which consequently increase the stiffness of the contact, enlarge the force chain network and therefore increase the characteristic length of the force chains (Davis et al., 1986; Job et al., 2008).

In this paper, we explore the wettability effect on the wave propagation in the (partial) saturated granular media by the experiments combining acoustic measurement and core flooding. We first present the experiment setup and results. The waveform of the P- and S-wave on each step of incremental water injection (an increase of water saturation) are recorded for both water-wetting and gas-wetting glass bead packings. The velocity-saturation-relation (VSR) and attenuation-saturation-relation (ASR) are extracted from the waveforms. Then, the wettability dependent scattering patterns are identified for two samples with different wettability. A wettability-dependent characteristic length of the force chains is used to interpret the wave scattering observations and the piece-wise function of effective bulk and shear moduli are proposed to simulate the transition from the coherent wave in dry or low saturation to incoherent wave in high and full saturation.

7.2. Experimental Setup

The experimental setup consists of a poly-carbonate cylinder (15.5mm inner diameter and 48-52mm length) packed with spherical glass beads with a quasi-identical diameter of 200 ± 50 μm and two piston piezoelectric acoustic transducers mounted on the two ends. This is the typical configuration to carry out acoustic measurements in granular materials (Johnson and Jia, 2005). The fluid can be injected through the inlet line and the displaced fluid exits through

the outlet line (Figure 7.1). Olympus V103 and V153 piezoelectric transducers with broadband frequency range 0.2 – 2 MHz and 1 MHz centre frequency are used to generate and receive P- and S-wave pulses, respectively. A uniaxial pressure of about 150 kPa is applied on the outside faces of the transducers to guarantee dense packing.

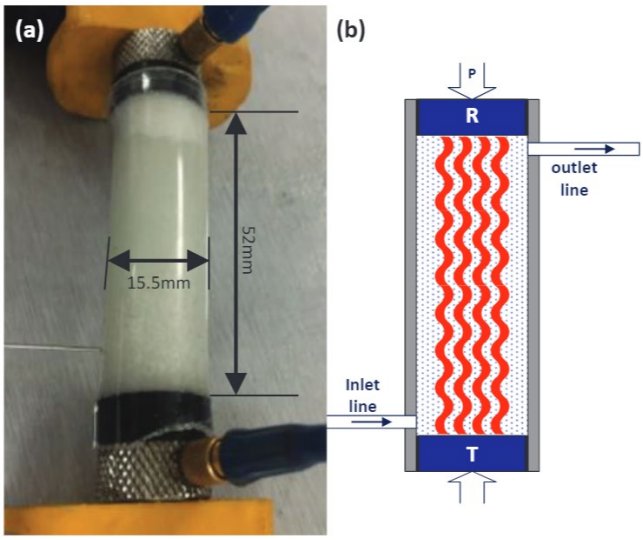

Figure 7. 1 (a) Real and (b) schematic experimental set-up for conducting acoustic measurement during the water-air core flooding in the glass bead pack under axial pressure P. T and R denote the piezoelectric transmitter and receiver, respectively.

To indicate the wettability the contact angle is measured. The water droplets are applied on the original glass surface and the Quilon-C treated surface, respectively, in the air environment. The measured contact angle is on a water-air-glass interface is 7.64°, which is far less than 90° indicating that the pure, untreated glass beads are strongly water-wetting (Figure (7.2)). The water is incrementally injected into the packing through the inlet line with an approximate flow rate of 0.7 ml/s. The acoustic measurement is conducted after each incremental injection. The change of water saturation is precisely captured by measuring the weight of the sample.

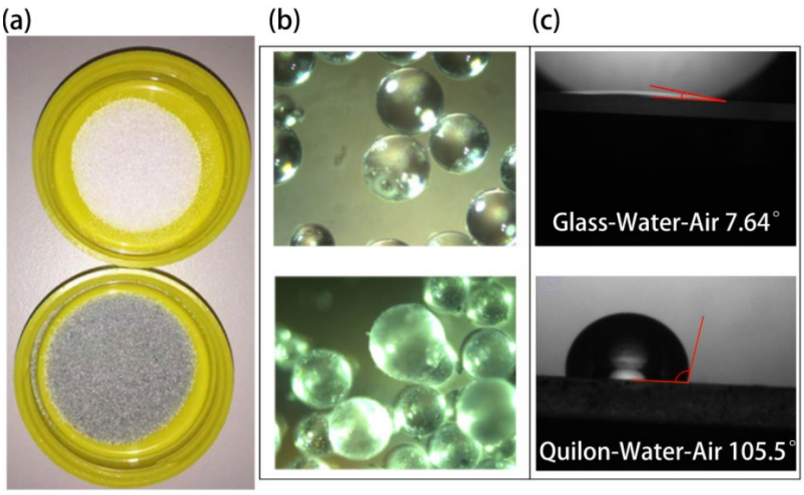

Figure 7. 2 (a) Original glass bead sample (top) appearing in shiny white color and the Quilon-C treated glass bead sample (bottom) in dark green color; (b) microscopy images of the original glass beads and treated beads; (c) the corresponding contact angle of water droplet on the original glass surface (top) is 7.64° and on the processed glass surface after Quilon chemical treatment (bottom) is 105.5°.

The same injection-measurement procedure is performed on the glass bead packing when the wettability is altered in order to have gas wetting glass beads. Quilon-C in isopropyl alcohol solution is used to alter the wettability of the original water-wetting glass beads to be gas-wetting by following the same procedures outlined in the literature (Garrouch and Sharma, 1995). The chemical contains C-14-C-18 fatty acids with chromium, which bonds the negatively charged glass bead surface rendering a gas-wetting thin coating on the spheres. An advantage of such treatment is that there is little impact on the porosity of the fully saturated porous medium (Garrouch and Alikhan, 1997). We find that the porosity of glassbead packing changes from 38.5% as the original hydrophilic condition to 37.5% as processed hydrophobic condition. The hydrophobicity or gas-wetting condition is confirmed by a 105.5° measured contact angle on the water-air-glass interface after the Quilon chemical treatment (Figure 7.2).

While the porosity and permeability are not significantly changed due to the chemical treatment, the mechanical properties are expected to change. In the case of water-wetting glass bead packing, the sample can be thought of as almost uncemented, only held together by the enclosure of the sleeve and the uniaxial compression applied. However, in the gas-wetting glass bead packing, the water-repellent coating and the possible residual chemical deposition on the glass beads as demonstrated in Figure 7.2b act as cement layers. They strengthen the entire stiffness of the gas-wetting glass bead packing (Dvorkin et al., 1991; Dvorkin et al., 1994).

This is confirmed by the observation that the P-wave velocity of dry gas-wetting glass bead packing is higher than the value of the dry water-wetting sample (Figure 7.5 and 7.6).

7.3. Experimental Results

7.3.1. Water-wetting Case

Seismograms of P- and S-wave are recorded separately for the water-wetting sample for each saturation step (Figure 7.3). We observe that in the P-wave transmission experiment (Figure 7.3a) there is a clear transition from a stable coherent wave pulse towards a set of incoherent scattering waves with shorter wavelengths for increasing water saturation. With incremental water injection, initially, the traveltime of the first arrival slightly increases and the amplitude decreases slowly until a critical water saturation $S_c \approx 89\%$ is reached. Beyond this saturation, the traveltime becomes very short and the amplitude increases sharply. For the S-wave transmission experiment, there is only one coherent pulse recognizable whose traveltime increases slightly with the increase of water saturation. Nevertheless, the P-wave arrival is visible on the S-wave measurement at low and intermediate water saturation (Figure 7.3b).

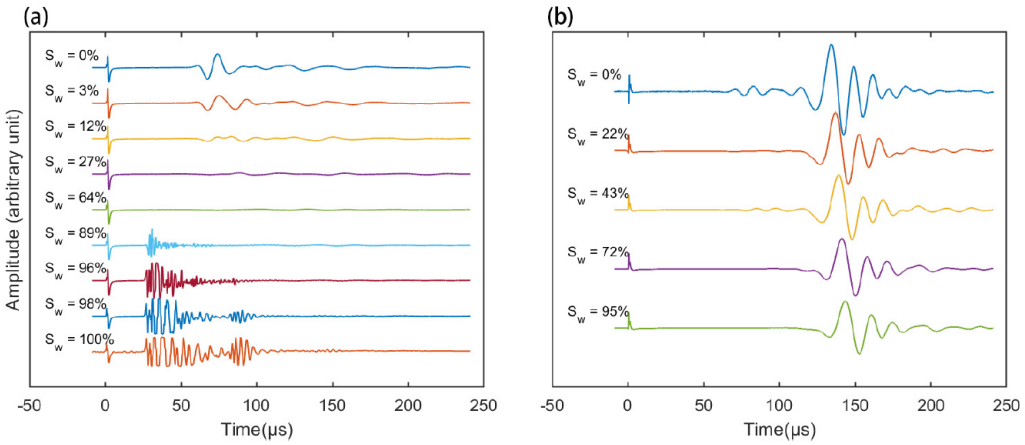

Figure 7. 3 Recorded waveforms of (a) P-wave and (b) S-wave after incremental injection for water-wetting glass bead packing. The small peak at the t=0 is the cross-talk signal during the pulse generation.

7.3.2. Gas-wetting Case

The gas-wetting glass beads are obtained from the original water-wetting beads treated by the wettability alteration agent Quilon C. Better cemented contact between glass beads is expected after the treatment. This is indeed corroborated since we observe higher amplitude and higher

velocity for dry gas-wetting glass bead packing compared to the original water-wetting one. However, with the increase of water saturation, the gas wetting packing exhibits a strong damping effect, and the waveforms of both P- and S-wave become attenuated drastically (Figure 7.4). The increase of water saturation stops around 93%-94% in the standard water flooding procedure with about 6% residual gas saturation. After a three-fold increase of the injection pressure, we spot some of the suspected scattered P-waves after the critical water saturation $S_c \approx 98\%$, though the amplitude is very small (Figure 7.4a). The gas as wetting fluid phase is trapped inside the grain contact and hardly displaced by the water in the standard water injection process. However, the increased injection pressure may overcome the capillary pressure and thereby push the non-wetting water into some of the grain contacts.

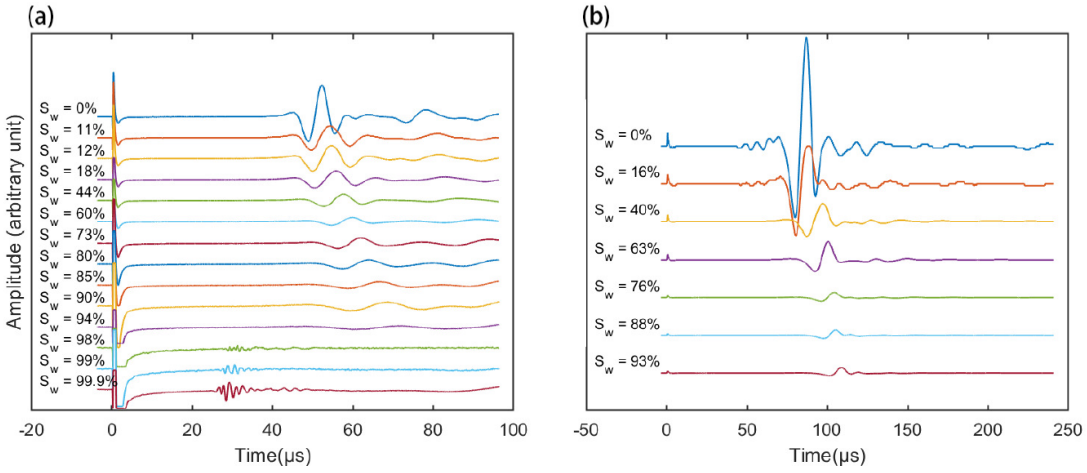

Figure 7. 4 Recorded waveforms with incremental water injection for gas-wetting glass bead packing: (a) P-wave; (b) S-wave transmission experiments.

7.4. Wettability Impact on the Velocity and Attenuation

The inferred velocity-saturation-relation (VSR) of both P- and S-wave transmission experiments are plotted in Figures 7.5 and 7.6 for the water-wetting and gas-wetting samples, respectively. The results are compared with the Gassmann-Wood limit (lower bound for uniform saturation) and Gassmann-Hill limit (upper bound for patchy saturation), where the detailed formulas are given in Appendix B. The predictions of the Biot theory, i.e., for a fully saturated porous medium are also provided for reference by using the parameters provided in Table 7.1. In addition, we infer the attenuation-saturation relation for both transmission experiments. The attenuation is obtained via the spectral-ratio method (with key formulas in Appendix C). The results are plotted in Figure 7.7.

7.5.1. Water-wetting case

For the water-wetting sample, water tends to occupy the glass bead surface and the grain contacts as soon as the fluid is fingering through the inter-granular voids. This favors the generation of capillary bridges (pendulum rings made of water). Initially, such capillary bridges may only appear in the finest and smallest pores. The water then quickly occupies the relatively large pores. At low to intermediate water saturation, the capillary bridges are not fully established in all grain contacts. Therefore, the force chains are thought to form a discontinuous pattern like schematically indicated in the inset of Figure 7.5. Then the P-wave VSR is closer to the prediction of Gassmann-Wood bound. At the same time, the attenuation of the P-wave (Figure 7.7a) becomes higher with increasing water saturation but the attenuation of the S-wave (Figure 7.7b) is less affected by the change of water saturation. Once the water saturation reaches a critical saturation (i.e., $S_c \approx 89\%$) and beyond, the force chains under ultrasonic frequency become reinforced and the grain contacts saturated by water form in a continuous percolating pattern (inset of Figure 5).

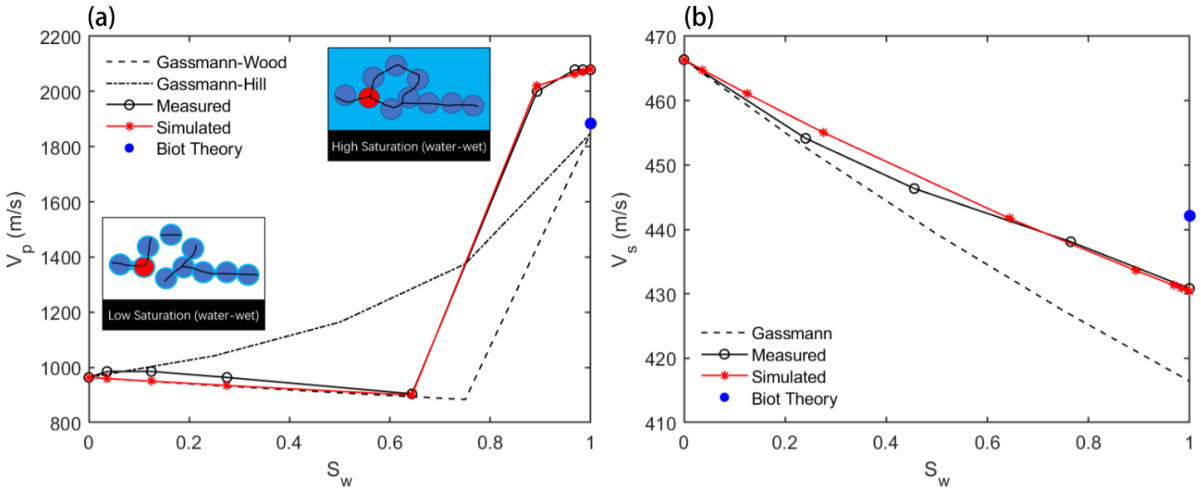

Figure 7. 5 The measured velocity-saturation relation in water-wetting glass bead packing is compared with Gassmann-Wood and Gassmann-Hill theoretical predictions for (a) P-Wave and (b) S-Wave. As a reference, Biot theory is used for the calculation of the velocities of the sample under full water saturation. The inset cartoons illustrate the network of force chains (black solid line) in low and fully saturated samples.

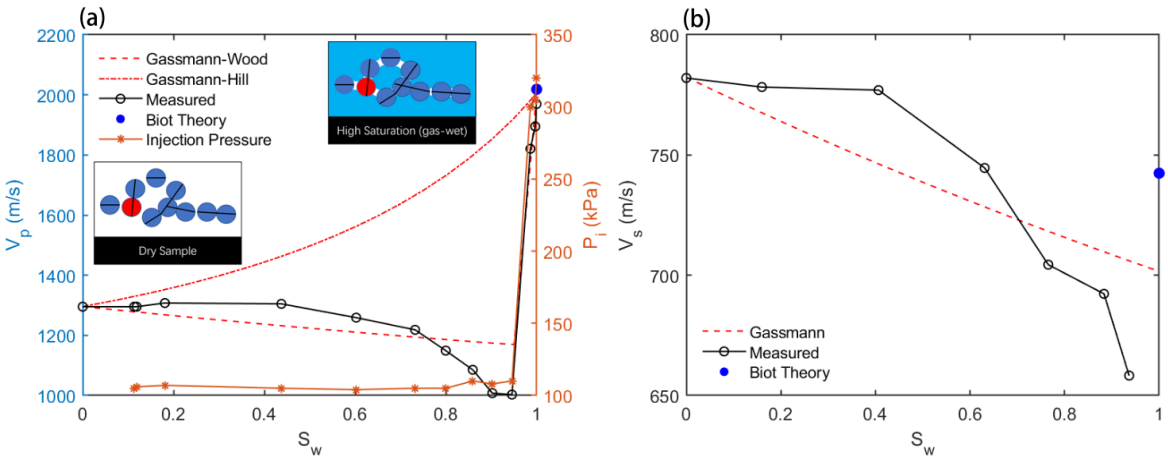

Figure 7. 6 Velocity-saturation relations in gas-wetting glass bead packing vs Gassmann-Wood and Gassmann-Hill predictions for (a) P-Wave and (b) S-Wave. The last three measurements in high water saturation are obtained after increasing 300% injection pressure P_i. The inset cartoons demonstrate the network of force chain (black solid line) in dry and high to near fully saturated samples.

Table 7. 1 Parameters of glassbead packing and the injected water

Parameters	Symbol	Value	Unit
Water			
Density	ρ_w	997	kg/m^3
Bulk Modulus	K_w	2.25E+09	Pa
Viscosity	μ_w	1.00E-03	Pa·s
Solid			
Density	ρ_s	2455	kg/m^3
Bulk Modulus	K_s	3.70E+10	Pa
Hydrophilic water-wetting dry frame			
P Wave Velocity	V_p	963.504	m/s
S Wave Velocity	V_s	466.36	m/s
Porosity	φ	0.385	
Tortuosity*	T	1.80	
Permeability†	κ	3.37E-11	m^2
Hydrophobic gas-wetting dry frame			
P Wave Velocity	V_p	1295.24	m/s
S Wave Velocity	V_s	782	m/s
Porosity	φ	0.375	
Tortuosity*	T	1.83	
Permeability†	κ	3.00E-11	m^2

* $T \approx \frac{1}{2}\left(1+\frac{1}{\phi}\right)$ as (Berryman and Thigpen, 1985);

† Kozeny-Carman (KC) permeability $\kappa = \frac{\phi^3}{36k(1-\phi)^2}d^2$ as (Xu and Yu, 2008), where the empirical KC constant $k = 5$ and grain diameter $d \approx 2 \times 10^{-4} m$.

This interstitial liquid-induced structural change of the force chains has a paramount impact on the velocity and the attenuation. On the one hand, it leads to higher effective elastic moduli (both bulk modulus and shear modulus) of matrix frame. Since the composite density does not change appreciably, the corresponding P- and S-wave velocities at higher saturation are larger compared to the Gassmann predictions (Figure (7.5)). On the other hand, the overall growth of the force chain network is accompanied by a local clustering of grains connected via capillary bridges. These clusters, in turn, can be characterized by a characteristic length that exceeds the individual grain size. Once the characteristic length becomes comparable to the P-wavelength, the notion of an effective medium is no longer valid. Instead, one expects that the P-wave is elastically scattered at the clusters. This could explain the emergence of the incoherent wave pulses seen in Figure (7.3). Given that the frequency range of the piezoelectric transducer is 0.2-2 MHz, the P-wavelength ranges from 1-10 mm for either water-wetting or gas-wetting samples in (near) full water saturation condition. However, the diameters of the glass beads are much smaller, d = 0.2 ± 0.05mm. If the characteristic length of the force chains is short-ranged ($\xi \sim d$) due to the gas filled grain contacts, there should be little incoherent signals and a stable P-wave pulse is propagating. However, the observation of the incoherently scattered waves in the water-wetting sample is suggestive of the existence of long-range characteristic length ($\xi \sim 5d - 10d$).

The appearance of these incoherently scattered waves is also clearly marked as a negative $1/Q_p$ in the P-wave attenuation-saturation relation (Figure 7.7a). The negative value is a consequence of using the spectral ratio method to determine the inverse quality factor 1/Q. It essentially consists of dividing the amplitude spectrum of a waveform by a reference amplitude spectrum. (i.e., the signal in an aluminium core with the same length as the sample). This reference amplitude spectrum in shown in Figure 8b (black line). The amplitude spectrum corresponding to the first period of a scattered wave in the water-wetting sample has two peaks (Figure 8b, red line). The centre frequency that corresponds to the first peak (#1 in Figure 8b) is lower than the centre frequency of the reference amplitude spectrum. Computing the spectral ratio at this centre frequency yields to a positive Q value. Conversely, computing the spectral ratio at the centre frequency of the second peak (#2 in Figure 8b) yields to a negative Q value. The changes in the force chain network due to the injection of the liquid bring the amplitude spectrum a bi-modal pattern, which contains not only low-frequency coherent waves but also high-frequency incoherent scattering components (Figure 9a). These scattered waves are associated with a

negative 1/Q. In this sense, the Q factor does not quantify the amplification of a pulse but is an indication of the change of signal character.

The Gassmann-Wood predictions match the measured P-wave velocity reasonably well at low- to intermediate water saturation as long as the saturation is below the critical water saturation S_c. At a water saturation beyond S_c, the force chain networks can be thought of as unrelaxed grain contacts, where local pressure gradients induced by the wave are not equilibrated. Such a scenario resembles the high-frequency unrelaxed frame concept developed by Mavko and Jizba (1994) and described by the Mavko-Jizba relations. The basic idea is that the non-equilibrated wave-induced pressure perturbation at grain contact is incorporated in form of high-frequency unrelaxed "wet-frame moduli" K_{uf} and μ_{uf}. These moduli are higher compared to the moduli at low frequencies when the pressure gradients are equilibrated. We find that the Mavko-Jizba relations work well to predict the P- and S-wave velocities of the fully saturated water-wetting sample as the water occupies the grain contacts to form a "wet-frame". By taking advantage of the two end velocities (dry and full saturation), we are able to simulate the P-wave velocities at high saturation ($S_w \geq S_c$) and S-wave velocities by the Voigt averaged elastic moduli:

$$K = \begin{cases} K_{GW}; & when\ S_w < S_c \\ K_d(1 - S_w) + K_{MJ}S_w & when\ S_w \geq S_c \end{cases} \tag{7.1}$$

$$\mu = \mu_d(1 - S_w) + \mu_{MJ}S_w \ , \tag{7.2}$$

where the K_{GW} are Gassmann-Wood limit of the bulk modulus of the partially saturated sample, K_{MJ} and μ_{MJ} are the bulk and shear moduli of the fully saturated sample by Mavko-Jizba relations, K_d and μ_d are the bulk and shear moduli of the drained (dry) sample. We list the relevant formulas in Appendix B.

The results of the simulation of velocities in water-wetting sample by using the piecewise function equations 7.1 and 7.2 match the experimental measurements very well as demonstrated in Figure (7.5).

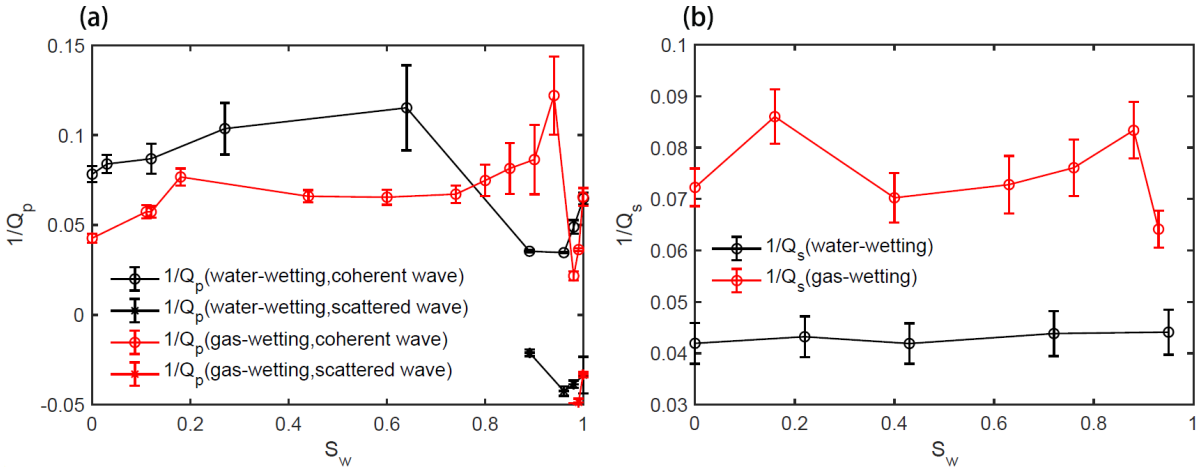

Figure 7. 7 Attenuation-saturation relations of (a) P-wave and (b) S-wave for both water-wetting and gas-wetting samples.

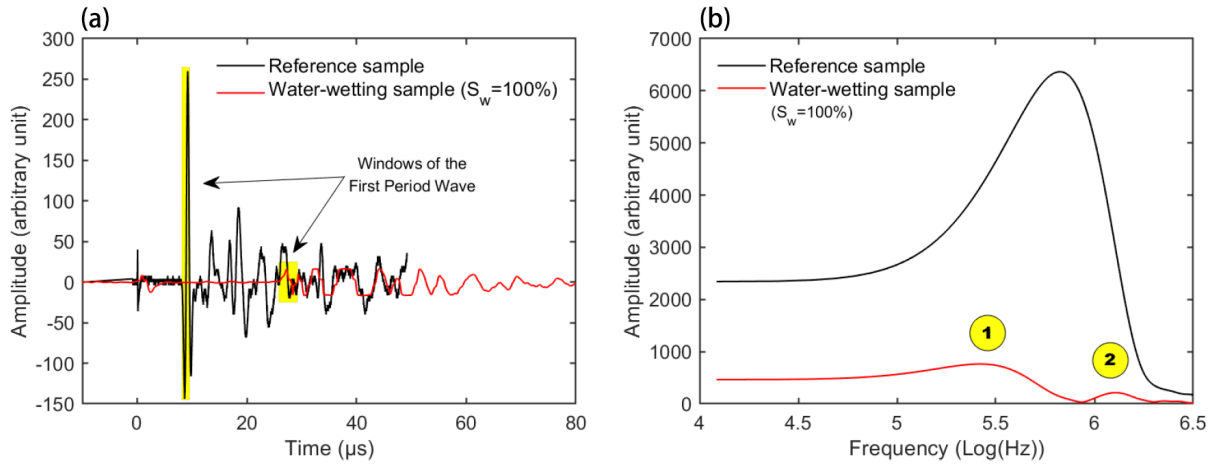

Figure 7. 8 (a) The waveforms through the reference sample (aluminium dummy core) and water-wetting sample with 100% water saturation where the time windows of the first period of waveforms are selected (shading highlight) for calculating the amplitude spectrum in each sample; (b) the corresponding spectra by Fourier transform where two peaks are produced in the spectrum of signals in fully saturated water-wetting sample.

7.5.2. Gas-wetting case

Our hypothesis is that only the fluid between the grain contacts has a significant impact on the force chain network and therefore on the effective bulk moduli of the matrix frame. For the gas-wetting case, air as wetting-fluid tends to occupy the grain contacts while water is forced into the relatively large interstitial pores from the beginning to the end of the water injection (inset of Figure 7.6). However, the bulk modulus of the air in the grain contacts of the gas-wetting glass beads is negligibly small so that there should be no big change in the structure of the force chain network and the effective moduli of the matrix frame during the water flooding. The measured P-wave VSR coincidentally agrees with the predictions of the Gassmann-Wood

limit but far away from Gassmann-Hill predictions indicating that the two immiscible fluids tend to be in a homogenous mixing condition but with little heterogeneous patchy fluid pocket (Figure 7.6).

The water saturation stops increase at about 93-94% in the normal water flooding procedure with about 6% residual gas saturation for the gas-wetting sample. However, after increasing about 300% injection pressure overcoming the capillary pressure, the non-wetting water was pushed into some of the grain contacts. In our interpretation, this should lead to a force chain reinforcement. This is supported by the observation of small amplitude "scattered" waves, which in fact contain both coherent part and incoherent part (Figure 9b). Their P-wave attenuation obtained by the spectral-ratio method is as similar to the scenario of the water-wetting sample.

7.5.3. The Role of Wettability in P-wave Transmission

There is only one coherent pulse observed in the S-wave transmission experiments regardless of the saturation condition and the wettability of the samples. However, in the P-wave transmission experiments, there is a transition from the coherent P-wave pulse in the dry samples to the incoherently scattered waves in the samples with high water saturation.

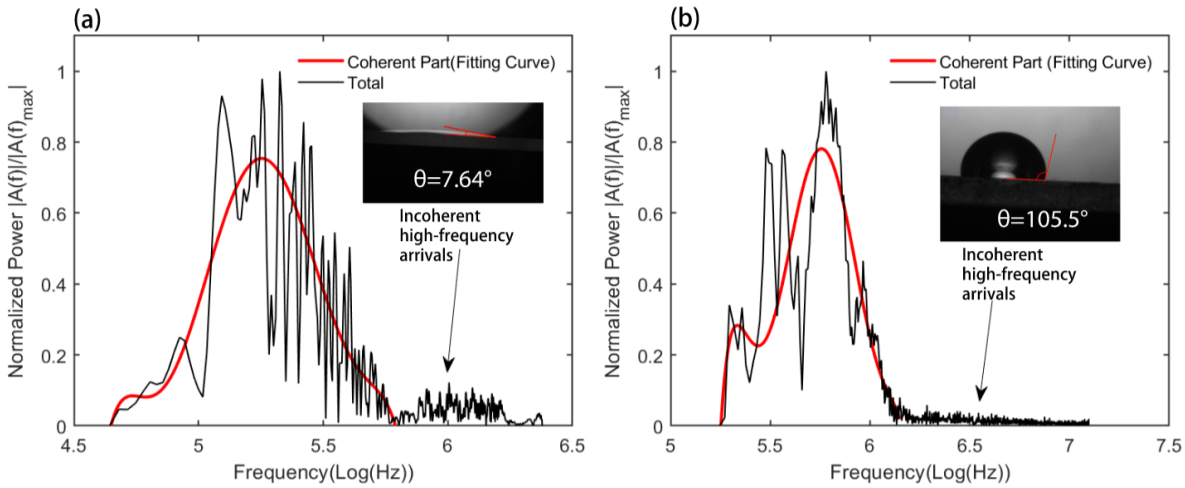

Figure 7.9 The Amplitude spectra A(f) normalized by the maximum value for the fully saturated (**a**) water-wetting and (**b**) gas-wetting glass bead packings. The insets of figures show the contact angle of water droplet on the glass-air interface.

The amplitude spectra of P-waves in the fully water-saturated samples are plotted in Figure 7.9. We observe that the water-wetting spectra contain a low-frequency part and a high-frequency part. Similar experimental observations are reported by Güven et al. (2017) and Jia et al. (1999). However, the incoherent arrivals in the spectra of the gas-wetting sample are rare and small. We project that the fluid in the grain contacts plays a crucial role in the continuity of the force chains, where the liquid promotes the development of long force chains as in the water-wetting glass bead packing, but the gas, i.e., air restrains the extension of the force chains as in the gas-wetting glass bead packing. In such a way, the wettability is identified to have a significant impact on the force chain network by controlling the intergranular fluid distribution, which further determine the wave velocity, attenuation and scattering.

7.5. Discussion

7.5.1. Path Effect on the Acoustics of Porous Granular Media

When the wetting phase fluid is injected into the dry granular porous medium, it percolates through the pore space and occupies relatively small voids (i.e., grain contacts) in sequence. In this way, the force chains are extended and re-organized. However, it is unlikely that the percolation process proceeds such that a homogeneous force chain pattern (FCP) is generated. This should be especially true when the capillary pressure is small and the impact of gravity on the fluid distribution become considerable. In the following we explore some of the factors that may be responsible for the generation of heterogeneous FCPs, which in turn could explain the wavefield signatures observed from ultrasonic experimentation.

We hypothesize that heterogeneous FCP may occur during the injection such that the notion of an effective medium is no longer valid and instead the heterogeneous FCP gives rise to preferential wave (ray) paths, i.e., the path effect. To verify this hypothesis and investigate the path effect in porous granular media, we repeat the experiment as described in Section 2 but introduce two changes. First, we inject decane instead of water as the wetting phase fluid. The benefit of decane over water is that the decane has smaller interfacial tension in air (σ= 24.47mN/m) compared to water (σ= 72mN/m) (Rolo et al., 2002). The glass bead surface has similar wettability to the decane as to the water in the air with a contact angle of less than 10° so that the capillary pressure $P_c = 2\sigma \cos\theta / r$ for the decane-air system is only about 1/3 of the water-air system. Hence, the interplay between capillary forces and gravity (the sample in Figure 1 is oriented horizontally) should be more pronounced, thereby generating a more

favorable condition for FCP generation.

Second, we use a shorter sample of length L = 2.8cm (roughly half of the length of the original sample as in Figure 1). Because the shorter sample is used in the decane injection experiment, a portion of the heterogeneous decane saturation front is likely to reach the receiver early-on in the fluid injection experiment, say at low to moderate decane saturation. This is indeed observed experimentally (Figure 10a). It is thought that this heterogeneous saturation front creates different ray paths for ultrasonic waves (Figure 10b), thereby increasing the level of heterogeneity of the FCP. Specifically, the continuously decane saturated regions constitutes a distinguished fast ray path along which the high frequency waves travel. Since the FCP in the saturated regions is thought to be accompanied with larger characteristic lengths, these fast rays are scattered at clusters. The dry and the low saturation regions correspond to slow ray path along which mainly the low-frequency part of the broadband waves propagates. This leads to a deformation of the wave front and bias towards larger velocity by picking the first break as illustrated in Figure 10b. Such deformed wave front accounts for the mechanism of fast path dispersion or velocity shift (Cadoret et al., 1995; Mukerji et al., 1995). This could explain the recorded P-waveforms at intermediate saturation (i.e., So = 58% and So = 64%) in the decane injection experiment, where two types of wave arrivals with different frequencies are recorded in the same wave train (Figure 11).

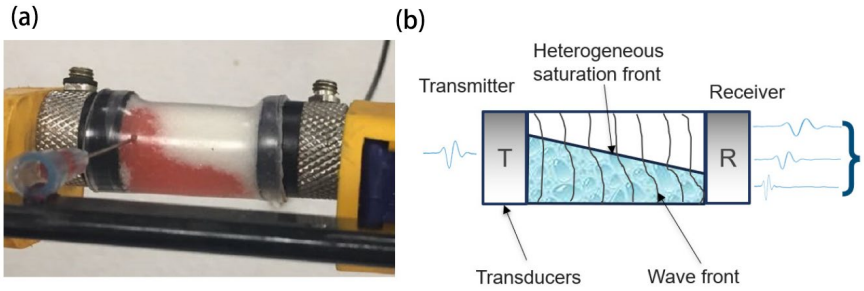

Figure 7. 10 (a) Different ray paths are produced during the injection of liquid into the short sample (L=2.8cm). (b) This schematic shows the path effect on the receiving signals with broadband frequencies where the short wavelength (high-frequency) wave tends to follow the fastest ray path.

7.5.2. Effect of Micro-slip Between Grains

It is worth noting that the velocities of both P- and S-wave drop to values lower than the Gassmann prediction at high saturations (from about 75% to 93%) in the gas-wetting sample but not in the water-wetting sample (Figure 7.6). This drop might be explained by microslip (sliding) between glass beads as suggested by Langlois and Jia (2014) and Makse et al. (2004).

This leads to an increase of the tangential friction (dissipation) since we see a similar pattern of increasing attenuation in both P- and S-wave at the middle to high water saturations in the gas-wetting sample. Such microslip also results in a drop in the velocities where the attenuation increases. The occurrence of microslip due to the grain sliding may be dependent on the wettability and water saturation, but a detailed investigation is required for this open question.

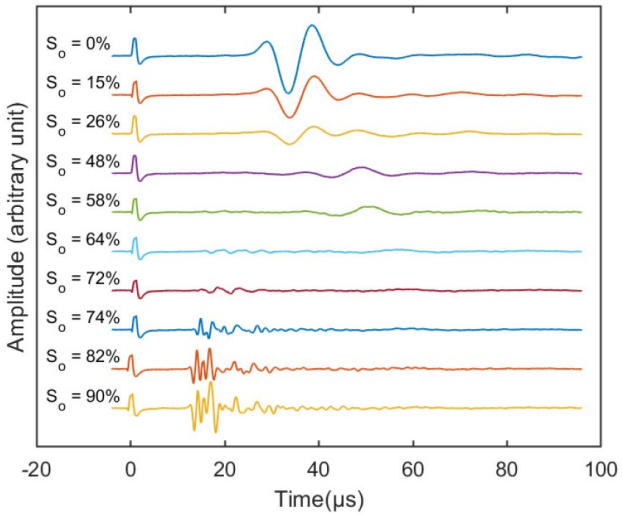

Figure 7.11 Recorded P-waveforms with incremental decane (oil) injection for shorter glassbead packings (L=2.8cm). Two types of signals with different frequencies are recorded in the same wave trains at intermediate saturations (i.e. S_o = 58% and S_o = 64%).

7.5.3. Comparison with Literature

As shown in the experimental results section, we observe a dramatic change in the waveforms during the change of the fluid saturation in porous granular media. It is interesting to note that a similar phenomenon is documented by Sayers and Dahlin (1993) (their Figure 12). The time-lapse waveform changes from high-frequency (short-period) arrivals when the sample is in the state of a cement paste (suspension of cement particles in water) to low-frequency (long-period) waves when sample becomes a cemented solid (saturated porous media). These waveform changes are caused by the structural changes during hydration and, compared to our results, the transition of the acoustic wave form has a reverse sequence. Since in the cement paste the interconnected chains of cement particles develop as a function of time, their observations may relate to our interpretation in terms of the reinforced force chains due to the presence of the intergranular fluid.

7.6. Conclusion

The velocity- and attenuation-saturation relations and P-wave scattering patterns in the water-wetting and gas-wetting granular porous media examined here show distinct characteristics. This indicates that wettability has a significant impact on wave propagation in the granular porous medium. We explain these characteristics in terms of wettability-dependent force chain network alterations. In particular, the effective elastic moduli and the characteristic length of the force chain network are altered during the water injection. The dry granular porous medium, as an extreme example, where all pores are saturated by air, has a short-range characteristic length. It behaves as an effective medium in which a stable pulse waveform is observed. For partial saturation, only if the water wets the grains, the liquid can intrude the small grain contacts. Therefore, the grain contact-filling fluid as wetting phase (i.e., water) results in the development of the longer range force chains and higher effective moduli. This appears to be a plausible explanation of the wave velocities that exceed the prediction of the Gassmann equations and the appearance of shorter pulses comprising a more complex wave train.

Chapter 8. Conclusions and Outlook for Future Research

8.1. Conclusions

This thesis aims to summarize the outcome of the research project of estimation of wettability by the elastic wave. Conventionally, the wettability measurement is a complicated and time-consuming task. While elastic wave has been widely used in seismic exploration and bore hole sonic logging, which is a non-destructive and economic technique. This research project demonstrates the possibility to use the elastic wave to determine the wettability of the saturated porous media by theoretical simulation and experimental study. The wettability as an interface phenomenon significantly influences the hydrodynamics and spatial distribution of the pore-filling fluids, by which the elastic properties (wave velocities and moduli) and the acoustic impedance properties (attenuation) are influenced. The main results and innovations of the research project are summarised below for a better understanding of the impact of wettability on the propagation of the elastic wave in porous media and its application of estimation of wettability from the measurement of elastic waves.

1. Impact of Wettability on the Elastic Wave Propagation in the Porous Media

   - The slip length can be used to characterize the wettability of a fluid saturated porous medium. The wettability dependent VEP model and apparent slip model with slip BC are developed.
   - The wettability effect on the viscosity correction factor, dynamic permeability/tortuosity, velocities, attenuation are analysed.
   - The wettability dependent wave propagation models predict higher phase velocities and attenuation peaks for hydrophobic fully saturated porous media in high-frequency range than the corresponding results of the hydrophilic ones.

2. Combined Effect Pore Size Distribution and Wettability on the Dynamic Permeability and Elastic Wave Propagation in the Porous Media

   - The dynamic permeability of porous medium is controlled by the pore size distribution (PSD) and the wettability, where the sub characteristic frequencies are associated with the characteristic pore sizes.

- The potential applications of the PSD dependent dynamic permeability model may extend to the continuous dynamic permeability from the NMR well logging for the wellbore sections.

- The wettability effect on the wave propagation in the porous media with broadband PSD is studied by implementing the slip boundary condition, which points to similar results as VEP model.

3. Impact of Wettability on the Wave Propagation in the Partially Granular Porous Media

   - The velocity-saturation relation (VSR) and attenuation-saturation relation (ASR) in the water-wetting and gas-wetting granular porous media show distinct characteristics, which can be explained by the wettability dependent force chains.

   - As in the partial saturation conditions, only if the water wets the grains, can the liquid intrude the small grain contacts/gaps; therefore, the gap-filling fluid water results in the development of the long-range force chains and higher effective moduli and velocity than the prediction of Gassmann equations.

4. Potential of the Wettability Determination by Using the Measurement of Elastic Wave

   - The theoretical studies demonstrate that the non-wetting fluid saturated porous material has higher phase velocities than the wetting fluid saturated one for all kinds of P- waves and S- wave in the intermediated frequencies but convergent to the same value in the low and high frequency limits.

   - The attenuation demonstrates a higher peak value and the entire attenuation curve is constrained in a narrower frequency range for the slip BC (non-wetting saturation) compared to that of the no-slip BC (wetting saturation).

   - The theoretical model developed has the potential to be applied in the prediction of wettability by measuring the velocity dispersion, which has been qualitatively validated by the experiments.

8.2. Outlook for Future Research

This thesis has studied the role of wettability in wave propagation in the porous medium, which has been neglected in the previous geophysics and rock physics studies. Although several theoretical models have been developed in this research project, limited experiments

are performed. Thus, more experimental studies are desired for this research topic to verify and supplement the theoretical predictions. In particular, the following works are suggested to continue this research project:

- Theoretical study/models are required to be developed to account for the wave propagation in the porous media with partial saturation of multiple immiscible fluids with respect to the wettability impact.
- The experiments of wave measurement in the partially saturated samples with different wettability are preferred. Since the spatial distribution of the fluid is influenced not only by the wettability but also by the saturation regulating method, i.e. drainage/imbibition, the monitor of fluid distribution is preferably conducted at the same time as the wave measurement.
- Multiple frequency measurements are suggested due to the wettability effect are sensitive to the frequency range. The dispersion of the wave velocities has been identified as a key factor to determine the wettability in porous media. However, the approach will be more experimental measurements are conducted in more samples with various lithology and more saturation combinations of various immiscible fluids.

Appendix A Plane Wave Solution

The original equations of motion for an isotropic fluid-saturated porous medium are developed by Biot (Biot, 1956a). The set of equations are compatible with the dynamic permeability and tortuosity concept (Johnson et al., 1987). The complex phase velocities solved by plane wave analysis (Johnson et al., 1994a) are,

$$V_c^2(fast, slow) = \frac{\Delta \pm \sqrt{\Delta^2 - 4(\rho_{11}\rho_{22} - \rho_{12}^2)(\mathcal{A}\mathcal{R} + 2\mu_d\mathcal{R} - \mathcal{Q}^2)}}{2(\rho_{11}\rho_{22} - \rho_{12}^2)} \quad , \tag{A.1}$$

$$\mathrm{V}_c^2(shear) = \frac{\mu_d \rho_{22}}{\rho_{11}\rho_{22} - \rho_{12}^2} \quad , \tag{A.2}$$

Where, $\Delta = (\mathcal{A} + 2\mathcal{N})\rho_{22} + \mathcal{R}\rho_{11} - 2\mathcal{Q}\rho_{12}$.

The phase velocities and the inverse quality factors (dissipation factors) can be calculated as,

$$\mathrm{V}_j = \left[Re(\frac{1}{V_c})\right]^{-1}, j = p+, p-, s \tag{A.3}$$

$$Q^{-1} = \frac{2Im\left(\frac{1}{V_c}\right)}{Re\left(\frac{1}{V_c}\right)} \tag{A.4}$$

$\mathcal{A}$, $\mathcal{Q}$, and $\mathcal{R}$ are generalized elastic constants which are connected to the measurable quantities as ϕ porosity, K_s the bulk modulus of solid, K_d the bulk modulus of matrix frame, and K_f the bulk modulus of the fluid. μ_d is the shear modulus of the saturated rock as well as the matrix frame.

$$\mathcal{A} = K_d - \frac{2}{3}N + M(\alpha - \emptyset)^2 \tag{A.5}$$

$$\mathcal{Q} = \emptyset(\alpha - \emptyset)M \tag{A.6}$$

$$\mathcal{R} = \emptyset^2 M \tag{A.7}$$

$$M = [\frac{\alpha - \emptyset}{K_s} + \frac{\emptyset}{K_\mathrm{f}}]^{-1} \tag{A.8}$$

$$\alpha = 1 - K_d/K_s \tag{A.9}$$

The density coefficients ρ_{ij} are related to the densities of solid and fluid and the dynamic tortuosity which combines the viscous and inertial force.

$$\rho_{11} + \rho_{12} = (1 - \phi)\rho_s \tag{A.10}$$

$$\rho_{12} + \rho_{22} = \phi\rho_{\mathrm{f}} \tag{A.11}$$

$$\rho_{12} = \left(1 - \tilde{T}(\omega, b)\right)\phi\rho_{\mathrm{f}} \tag{A.12}$$

$\tilde{T}(\omega, b)$ is the dynamic tortuosity of either the VEP model as equation (3.21) or HF Biot model as equation (3.19).

The amplitude ratio of fluid and solid phases for compressional waves and shear wave are,

$$g_j = C_{fp}/C_{mp} = |\mathcal{Q} - \rho_{12}V_c^2|/|\mathcal{R} - \rho_{22}V_c^2|, \mathrm{j} = \mathrm{p}+, \mathrm{p}- \tag{A.13}$$

$$g_s = C_{fs}/C_{ms} = |\rho_{12}|/|\rho_{22}| \tag{A.14}$$

The phase difference between the fluid and solid phases are,

$$\psi_j = arctan\left[\frac{Im\left(\frac{\mathcal{Q}-\rho_{12}V_c^2}{\mathcal{R}-\rho_{22}V_c^2}\right)}{Re\left(\frac{\mathcal{Q}-\rho_{12}V_c^2}{\mathcal{R}-\rho_{22}V_c^2}\right)}\right], \mathrm{j} = \mathrm{p}+, \mathrm{p}- \tag{A.15}$$

$$\psi_s = arctan\left[\frac{Im\left(\frac{\rho_{12}}{\rho_{22}}\right)}{Re\left(\frac{\rho_{12}}{\rho_{22}}\right)}\right] \tag{A.16}$$

Appendix B Gassmann-Wood and Gassmann-Hill Limits for Partially Saturated Sample

The velocity of the P- and S-wave for the sample saturated by a single fluid can be calculated as,

$$V_p = \sqrt{\frac{K+\frac{4}{3}\mu}{\rho}} \quad , \tag{B.1}$$

$$V_s = \sqrt{\frac{\mu}{\rho}} \quad . \tag{B.2}$$

K: bulk modulus of the fully saturated sample

μ: shear modulus of the fully saturated sample

ρ: density of the fully saturated sample

The K and μ can be derived by the Gassmann equations,

$$\frac{K}{K_s-K} = \frac{K_d}{K_s-K_d} + \frac{K_\mathrm{f}}{\phi(K_s-K_\mathrm{f})} \quad , \tag{B.3}$$

$$\mu = \mu_d \ . \tag{B.4}$$

K_s: bulk modulus of solid

K_d: bulk modulus of the drained matrix (dry) frame

K_f: bulk modulus of the fluid

ϕ: porosity

μ_d: shear modulus of the drained matrix (dry) frame

Gassmann-Wood lower bound limit applying the Wood's law to determine the effective fluid bulk modulus K_f which can be further applied to determine the bulk modulus of the partially saturated sample ($K_{GW} = K$) by Eq. (B.3) and the velocity by Eq. (B.1),

$$\frac{1}{K_\mathrm{f}} = \frac{S_w}{K_w} + \frac{1-S_w}{K_g}. \tag{B.5}$$

S_w is the water saturation; K_w and K_g are the bulk moduli of the water and gas, respectively.

Gassmann-Hill upper bound limit uses the Hill's averaged bulk modulus of the partially saturated sample K which can be further used to calculate the velocity by Eq. (B.1),

$$\frac{1}{K+\frac{4}{3}\mu} = \frac{S_w}{K_1+\frac{4}{3}\mu} + \frac{1-S_w}{K_2+\frac{4}{3}\mu}. \tag{B.6}$$

K_1 , K_2 are the bulk moduli of the sample fully saturated by water and gas, respectively.

In either Gassmann-Wood or -Hill limit calculation, the density of the composite partially saturation sample is,

$$\rho = \rho_s(1-\phi) + \left(\rho_w S_w + \rho_g - \rho_g S_w\right)\phi. \tag{B.7}$$

ρ_w , ρ_g are the density of the water and gas, respectively.

The Mavko-Jizba relations use the bulk modulus K_{uf} and shear modulus μ_{uf} of the "unrelaxed frame" to replace the K_d and μ_d in the Gassmann equations (Eq. (B.3) and (B.4)) to calculate the moduli of the fully saturated sample ($K_{MJ} = K$; $\mu_{MJ} = \mu = \mu_{uf}$) and the corresponding velocities by Eq. (B.1) and (B.2).

$$\frac{1}{K_{uf}} \approx \frac{1}{K_h} + \left(\frac{1}{K_f} - \frac{1}{K_s}\right)\phi_s \quad , \tag{B.8}$$

$$\left(\frac{1}{\mu_{uf}} - \frac{1}{\mu_d}\right) = \frac{4}{15}\left(\frac{1}{K_{uf}} - \frac{1}{K_d}\right) \quad . \tag{B.9}$$

K_h: effective bulk modulus of the dry sample at very high pressure; $K_h = \pi K_d$ is used in the simulation.

ϕ_s: soft porosity or the porosity that closes at high pressure; $\phi_s = \phi/50$ is used in the simulation.

Appendix C Attenuation Estimation by Spectral-Ratio Method

The P- and S-wave attenuation (inverse quality factor) in glass bead packings is calculated by the spectral-ratio method (Toksöz et al., 1979). The ratio of amplitudes for the referenced aluminium dummy core and the sample is given as

$$\ln\left(\frac{A_1}{A_2}\right) = (\gamma_2 - \gamma_1)Lf + \ln\left(\frac{G_1}{G_2}\right), \tag{C.1}$$

where A is the Fourier amplitude, γ is the attenuation coefficient, f is the frequency, and G is the geometrical factor. Subscripts 1 and 2 indicate the sample and reference, respectively. $\ln(G_1/G_2)$ is a constant due to the sample and reference have the same shape and size. The sample length L and can be obtained from the direct measurement. The quality factor Q related to the attenuation coefficient can be expressed as:

$$Q = \frac{\pi}{\gamma \mathrm{v}} \ , \tag{C.2}$$

where v is the phase velocity. Owing to Q of referenced sample is very high, the γ_2 could be as 0, which only introduces less than 1% error. Thus, equation (C.1) can be written as

$$\ln\left(\frac{A_1}{A_2}\right) = -\frac{\pi L}{Q_1 v} f + \ln\left(\frac{G_1}{G_2}\right). \tag{C.3}$$

The attenuation of sample (Q_1^{-1}) can be estimated from the slope of the linear fitting of $\ln(A_1/A_2)$ versus the frequency.

Appendix D Copy Right Consent

Article Wettability effect on wave propagation in saturated porous medium. The Journal of the Acoustical Society of America, 147(2), 911-920.

AIP PUBLISHING LICENSE
TERMS AND CONDITIONS

Apr 04, 2021

This Agreement between Mr. Jimmy Li ("You") and AIP Publishing ("AIP Publishing") consists of your license details and the terms and conditions provided by AIP Publishing and Copyright Clearance Center.

License Number	5041790215729
License date	Apr 04, 2021
Licensed Content Publisher	Acoustical Society of America
Licensed Content Publication	The Journal of the Acoustical Society of America
Licensed Content Title	Wettability effect on wave propagation in saturated porous medium
Licensed Content Author	Jimmy X. Li, Reza Rezaee, Tobias M. Müller
Licensed Content Date	Feb 1, 2020
Licensed Content Volume	147
Licensed Content Issue	2
Type of Use	Thesis/Dissertation
Requestor type	Author (original article)
Format	Print and electronic

Article Pore Size Distribution Controls Dynamic Permeability. Geophysical Research Letters, e2020GL090558.

JOHN WILEY AND SONS LICENSE
TERMS AND CONDITIONS

Apr 04, 2021

This Agreement between Mr. Jimmy Li ("You") and John Wiley and Sons ("John Wiley and Sons") consists of your license details and the terms and conditions provided by John Wiley and Sons and Copyright Clearance Center.

License Number	5041910666745
License date	Apr 04, 2021
Licensed Content Publisher	John Wiley and Sons
Licensed Content Publication	Geophysical Research Letters
Licensed Content Title	Pore Size Distribution Controls Dynamic Permeability
Licensed Content Author	Jimmy X. Li, Reza Rezaee, Tobias M. Müller, et al
Licensed Content Date	Mar 4, 2021
Licensed Content Volume	48
Licensed Content Issue	5
Licensed Content Pages	9
Type of use	Dissertation/Thesis

Article Elastic waves in porous media saturated with non-wetting fluid. The APPEA Journal, 60(1), 315-325.

CSIRO PUBLISHING

Licence to Publish

APPEA Limited

The APPEA Journal

Manuscript No. AJ19196.R2

Title of the paper/presentation (the 'Work') Elastic Wave in Porous Media Saturated with non-wetting Fluid.

Author(s) Jimmy Li ; Reza Rezaee; Tobias Müller; Mohammad Sarmadivaleh

The APPEA Journal includes papers submitted to and presented at APPEA Conferences. The purpose of this Licence to Publish is to grant and confirm the grant of exclusive rights to publish the Work in the APPEA Journal.

The APPEA Journal is published by CSIRO Publishing for the Australian Petroleum Production and Exploration Association Limited (APPEA). APPEA Conference papers are made available to delegates to the APPEA Conference and included in the APPEA Journal. The APPEA Journal is a digital, online journal which is sold to subscribers and others.

By submitting this paper, the Author (Authors if a multi-authored paper) represents that they have the right or have obtained authorisation to enter into this Licence and grant the rights granted or contemplated by it.

The Author warrants that:

- Other than as a presentation at an APPEA Conference, the Work (including any abstract) has not been published before.
- The Work is not presently being considered for publication elsewhere.
- The Work does not violate any intellectual property right of any person or entity.
- The Work does not contain any subject matter that contravenes any laws (including defamatory material and misleading and deceptive material.
- The Work meets ethical standards applicable to the research discipline.
- The Work indicates any financial or non-financial interests/relationships that may be interpreted to have influenced the manuscript.
- All Authors have made a significant contribution to the Work and agree to its submission, and
- Permission for any tables or figures or other third party materials included in the Work that have been published elsewhere has been received from the relevant copyright holder and is attributed in the Work.

Terms of the Licence to Publish

1. In consideration for publication of the Work (and without derogating from rights granted in submitting the Work for the Conference), the Author grants to APPEA, through CSIRO Publishing (the 'Publisher'), an exclusive, royalty free, worldwide licence including the right to sub-license, to:
   - Reproduce, publish and communicate the Work, or any part of the Work, to the public in any and all media, whether existing before or after the date of this Licence, for commercial, educational and all other purposes for the full remaining term of the copyright subsisting in the Work in each applicable jurisdiction.
   - Approve fair and reasonable permission requests from third parties to reuse material contained in the Work for the purpose of study, research or subsidiary publication.

   The Author acknowledges that the Publisher is licensed by APPEA to publish and sell the APPEA Journal.
2. In addition to the Author's moral rights in respect of the Work, and subject to third party rights, the Author retains the right to:
   - Use copies of the Work for non-commercial purposes within his/her institution subject to the usual copyright licensing agency arrangements
   - Use the Work for further research and presentations at meetings and conferences
   - Use the illustrations (line art, photographs, figures, plates) and research data in his/her own future works
   - Include the Work in part or in full in a thesis provided it is not published for commercial gain
   - Place his/her pre-publication version of the Work on a pre-print server
   - Place his/her pre-publication version of the Work on a personal website or institutional repository on condition that there is a link to the definitive version on the APPEA Journal site hosted on the Publisher's website.
3. The Author agrees to:
   - Include a link and/or reference to the Work as published by the Publisher on all further uses of the Work or parts of the Work
   - Not reproduce or authorise others to reproduce adaptations of the Work that are substantially identical to the Work for any commercial publication
   - Not permit digital copies of the Work as published by the Publisher to be systematically networked to external users
   - Not use the Work in any way that implies that the Publisher, APPEA, the Journal or the Editors endorse any product or procedure described in the Work.
4. When exercising any of the rights assigned or granted, each party is required to give sufficient acknowledgement of the contribution made by the other party to the published material including a citation to the APPEA Journal.

Works made in the course of employment

5. Where the Work has been made by the Author (or in the case of multiple Authors, by any of them) in the course of employment and their employer owns copyright in the Work, that employer must sign this Licence. The employer has the same rights and obligations and gives the same warranties and licence rights as an Author under this Licence.

Appendix E: Attribution of Authorship

Li, J. X., Rezaee, R., & Müller, T. M. (2020). Wettability effect on wave propagation in saturated porous medium. The Journal of the Acoustical Society of America, 147(2), 911-920.

Authors and full affiliations:
Jimmy X. Li[a], Reza Rezaee[a], and Tobias Müller[b,c]
[a] WASM: Minerals, Energy and Chemical Engineering, Curtin University, 26 Dick Perry Avenue, Kensington, WA 6151, Australia.
[b]Department of Seismology, Centro de Investigación Científica y de Educación Superior de Ensenada, 22860 Ensenada, BC, Mexico.
[c]School of Earth Sciences and Engineering, Hohai University, Nanjing 211100, China

	Conception and design	Acquisition of data and method	Data conditioning and manipulation	Analysis and statistical method	Interpretation and discussion	Final approval
Dr. Reza Rezaee	✔				✔	✔
I acknowledge that these represent my contribution to the above research output. Signature:						
Dr. Tobias Müller					✔	✔
I acknowledge that these represent my contribution to the above research output. Signature:						

Li, J. X., Rezaee, R., Müller, T. M., & Sarmadivaleh, M. (2020). Elastic waves in porous media saturated with non-wetting fluid. The APPEA Journal, 60(1), 315-325.

Authors and full affiliations:
Jimmy X. Li[a], Reza Rezaee[a], Tobias Müller[b,c] , and Mohammad Sarmadivaleh[a]
[a] WASM: Minerals, Energy and Chemical Engineering, Curtin University, 26 Dick Perry Avenue, Kensington, WA 6151, Australia.
[b]Department of Seismology, Centro de Investigación Científica y de Educación Superior de Ensenada, 22860 Ensenada, BC, Mexico.
[c]School of Earth Sciences and Engineering, Hohai University, Nanjing 211100, China

	Conception and design	Acquisition of data and method	Data conditioning and manipulation	Analysis and statistical method	Interpretation and discussion	Final approval
Dr. Reza Rezaee					✔	✔
I acknowledge that these represent my contribution to the above research output. Signature:						
Dr. Tobias Müller					✔	✔
I acknowledge that these represent my contribution to the above research output. Signature:						
Dr. Mohammad Sarmadivaleh					✔	✔
I acknowledge that these represent my contribution to the above research output. Signature:						

Li, J. X., Rezaee, R., Müller, T. M., & Sarmadivaleh, M. (2020). Pore Size Distribution Controls Dynamic Permeability. Geophysical Research Letters, e2020GL090558.

Authors and full affiliations:
Jimmy X. Li[a], Reza Rezaee[a], Tobias Müller[b,c] , and Mohammad Sarmadivaleh[a]
[a] WASM: Minerals, Energy and Chemical Engineering, Curtin University, Perth, Australia

[b]Department of Seismology, Centro de Investigación Científica y de Educación Superior de Ensenada, 22860 Ensenada, BC, Mexico.
[c]School of Earth Sciences and Engineering, Hohai University, Nanjing 211100, China

	Conception and design	Acquisition of data and method	Data conditioning and manipulation	Analysis and statistical method	Interpretation and discussion	Final approval
Dr. Reza Rezaee					✔	✔
I acknowledge that these represent my contribution to the above research output. Signature:						
Dr. Tobias Müller					✔	✔
I acknowledge that these represent my contribution to the above research output. Signature:						
Dr. Mohammad Sarmadivaleh					✔	✔
I acknowledge that these represent my contribution to the above research output. Signature:						

Li, J. X., Rezaee, R., Müller, T. M., Madadi, M., & Sarmadivaleh, M. (2020). Wettability dependent P-wave scattering and velocity saturation relation in granular medium. SEG Technical Program Expanded Abstracts 2020.

Authors and full affiliations:
Jimmy X. Li[a], Reza Rezaee[a], Tobias Müller[b,c] , Mahyar Madadi[d], and Mohammad Sarmadivaleh[a]
[a] WASM: Minerals, Energy and Chemical Engineering, Curtin University, Perth, Australia
[b]Department of Seismology, Centro de Investigación Científica y de Educación Superior de Ensenada, 22860 Ensenada, BC, Mexico.
[c]School of Earth Sciences and Engineering, Hohai University, Nanjing 211100, China

[d]School of Mathematics and Statistics, The University of Melbourne, Parkville, VIC 3010, Australia.

	Conception and design	Acquisition of data and method	Data conditioning and manipulation	Analysis and statistical method	Interpretation and discussion	Final approval
Dr. Reza Rezaee					✔	✔
I acknowledge that these represent my contribution to the above research output. Signature:						
Dr. Tobias Müller					✔	✔
I acknowledge that these represent my contribution to the above research output. Signature:						
Dr. Mahyar Madadi					✔	✔
I acknowledge that these represent my contribution to the above research output. Signature:						
Dr. Mohammad Sarmadivaleh					✔	✔
I acknowledge that these represent my contribution to the above research output. Signature:						

Li, J. X., Rezaee, R., Müller, T. M., Madadi, M., Ma, R., & Sarmadivaleh, M. (2021). Path dispersion of elastic waves in granular matter. Paper presented at the SEG/SPWLA 2020 Workshop: 7th Workshop on Porous Media: Structure, Flow and Dynamics, Virtual, 2–3 December 2020.

Authors and full affiliations:
Jimmy X. Li[a], Reza Rezaee[a], Tobias Müller[b,c] , Mahyar Madadi[d], Rupeng Ma[c] and Mohammad Sarmadivaleh[a]
[a] WASM: Minerals, Energy and Chemical Engineering, Curtin University, Perth, Australia
[b]Department of Seismology, Centro de Investigación Científica y de Educación Superior de Ensenada, 22860 Ensenada, BC, Mexico.
[c]School of Earth Sciences and Engineering, Hohai University, Nanjing 211100, China
[d]School of Mathematics and Statistics, The University of Melbourne, Parkville, VIC 3010, Australia.

	Conception and design	Acquisition of data and method	Data conditioning and manipulation	Analysis and statistical method	Interpretation and discussion	Final approval
Dr. Reza Rezaee					✔	✔
I acknowledge that these represent my contribution to the above research output. Signature:						
Dr. Tobias Müller					✔	✔
I acknowledge that these represent my contribution to the above research output. Signature:						
Dr. Mahyar Madadi					✔	✔
I acknowledge that these represent my contribution to the above research output. Signature:						
Dr. Rupeng Ma					✔	✔
I acknowledge that these represent my contribution to the above research output. Signature:						
Dr. Mohammad Sarmadivaleh					✔	✔
I acknowledge that these represent my contribution to the above research output. Signature:						

Reference

Achdou, Y. and Avellaneda, M., 1992. Influence of pore roughness and pore-size dispersion in estimating the permeability of a porous medium from electrical measurements. Physics of Fluids A: Fluid Dynamics, 4(12): 2651-2673.

Al Hinai, A., Rezaee, R., Esteban, L. and Labani, M., 2014. Comparisons of pore size distribution: a case from the Western Australian gas shale formations. Journal of Unconventional Oil and Gas Resources, 8: 1-13.

Alemu, B.L., Aker, E., Soldal, M., Johnsen, Ø. and Aagaard, P., 2013. Effect of sub-core scale heterogeneities on acoustic and electrical properties of a reservoir rock: a CO2

flooding experiment of brine saturated sandstone in a computed tomography scanner. Geophysical Prospecting, 61(1): 235-250.

Amott, E., 1959. Observations Relating to the Wettability of Porous Rock. Society of Petroleum Engineers.

Anderson, W., 1986a. Wettability Literature Survey- Part 1: Rock/Oil/Brine Interactions and the Effects of Core Handling on Wettability. J. Pet. Technol: 1125-1144.

Anderson, W., 1986b. Wettability Literature Survey- Part 4: Effects of Wettability on Capillary Pressure.

Anderson, W., 1986c. Wettability literature survey-part 2: Wettability measurement. Journal of petroleum technology, 38(11): 1,246-1,262.

Anderson, W., 1986d. Wettability literature survey-part 3: the effects of wettability on the electrical properties of porous media. Journal of Petroleum Technology, 38(12): 1,371-1,378.

Anderson, W., 1986e. Wettability Literature Survey-Part 6: The Effects of Wettability on Waterflooding.

Anderson, W., 1986f. Wettability Literature Survey Part 5: The Effects of Wettability on Relative Permeability.

Anthony, J.L. and Marone, C., 2005. Influence of particle characteristics on granular friction. Journal of Geophysical Research: Solid Earth, 110(B8).

Ba, J., Carcione, J. and Nie, J., 2011. Biot-Rayleigh theory of wave propagation in double-porosity media. Journal of Geophysical Research: Solid Earth, 116(B6).

Bacri, J.C. and Salin, D., 1986. Sound velocity of a sandstone saturated with oil and brine at different concentrations. Geophysical Research Letters, 13(4): 326-328.

Barrat, J.-L., 1999. Influence of wetting properties on hydrodynamic boundary conditions at a fluid/solid interface. Faraday discussions, 112: 119-128.

Benalla, M., Cardoso, L. and Cowin, S.C., 2012. Analytical basis for the determination of the lacunar–canalicular permeability of bone using cyclic loading. Biomechanics and Modeling in Mechanobiology, 11(6): 767-780.

Beranek, L.L., 1947. Acoustical properties of homogeneous, isotropic rigid tiles and flexible blankets. The Journal of the Acoustical Society of America, 19(4): 556-568.

Berg, S., Cense, A., Hofman, J. and Smits, R., 2008. Two-phase flow in porous media with slip boundary condition. Transport in porous media, 74(3): 275-292.

Bernabé, Y., Mok, U., Evans, B. and Herrmann, F., 2004. Permeability and storativity of binary mixtures of high-and low-permeability materials. Journal of Geophysical Research: Solid Earth, 109(B12).

Berryman, J.G., 1980. Long-wavelength propagation in composite elastic media II. Ellipsoidal inclusions. The Journal of the Acoustical Society of America, 68(6): 1820-1831.

Berryman, J.G., 2003. Dynamic permeability in poroelasticity. Stanford Exploration Project, 113: 1-454.

Berryman, J.G. and Thigpen, L., 1985. Effective constants for wave propagation through partially saturated porous media. Applied Physics Letters, 46(8): 722-724.

Biot, M.A., 1941. General theory of three-dimensional consolidation. Journal of applied physics, 12(2): 155-164.

Biot, M.A., 1956a. Theory of propagation of elastic waves in a fluid-saturated porous solid. I. Low-frequency range. The Journal of the acoustical Society of america, 28(2): 168-178.

Biot, M.A., 1956b. Theory of propagation of elastic waves in a fluid-saturated porous solid. II. Higher frequency range. the Journal of the Acoustical Society of America, 28(2): 179-191.

Biot, M.A., 1962. Mechanics of deformation and acoustic propagation in porous media. Journal of applied physics, 33(4): 1482-1498.

Blunt, M.J., 2017. Multiphase flow in permeable media: A pore-scale perspective. Cambridge University Press.

Bonaccurso, E., Kappl, M. and Butt, H.-J., 2002. Hydrodynamic force measurements: boundary slip of water on hydrophilic surfaces and electrokinetic effects. Physical Review Letters, 88(7): 076103.

Brown, R.J. and Fatt, I., 1956. Measurements of fractional wettability of oil fields' rocks by the nuclear magnetic relaxation method, Fall Meeting of the Petroleum Branch of AIME. Society of Petroleum Engineers.

Brunet, T., Jia, X. and Mills, P., 2008. Mechanisms for acoustic absorption in dry and weakly wet granular media. Physical review letters, 101(13): 138001.

Buckingham, M.J., 2000. Wave propagation, stress relaxation, and grain-to-grain shearing in saturated, unconsolidated marine sediments. The Journal of the Acoustical Society of America, 108(6): 2796-2815.

Bultreys, T., Van Hoorebeke, L. and Cnudde, V., 2016. Simulating secondary waterflooding in heterogeneous rocks with variable wettability using an image-based, multiscale pore network model. Water Resources Research, 52(9): 6833-6850.

Cadoret, T., Marion, D. and Zinszner, B., 1995. Influence of frequency and fluid distribution on elastic wave velocities in partially saturated limestones. Journal of Geophysical Research: Solid Earth, 100(B6): 9789-9803.

Cadoret, T., Mavko, G. and Zinszner, B., 1998. Fluid distribution effect on sonic attenuation in partially saturated limestones. Geophysics, 63(1): 154-160.

Cao, B., Yuan, Z. and Guo, C., 2006. Velocity slip of liquid flow in nanochannels [J]. Acta Physica Sinica, 10(55): 5305-5310.

Carcione, J.M., 2007. Wave fields in real media: Wave propagation in anisotropic, anelastic, porous and electromagnetic media, 38. Elsevier.

Carcione, J.M., 2015. Wave Fields in Real Media (Third Edition). In: J.M. Carcione (Editor), Wave Fields in Real Media (Third Edition). Elsevier, Oxford, pp. 299-420.

Carcione, J.M. and Gurevich, B., 2011. Differential form and numerical implementation of Biot's poroelasticity equations with squirt dissipation. Geophysics, 76(6): N55-N64.

Carcione, J.M., Helle, H.B. and Pham, N.H., 2003. White's model for wave propagation in partially saturated rocks: Comparison with poroelastic numerical experiments. Geophysics, 68(4): 1389-1398.

Cardoso, L., Fritton, S.P., Gailani, G., Benalla, M. and Cowin, S.C., 2013. Advances in assessment of bone porosity, permeability and interstitial fluid flow. Journal of Biomechanics, 46(2): 253-265.

Causin, E. and Bona, N., 1994. In-Situ Wettability Determination: Field Data Analysis. Society of Petroleum Engineers.

Chandler, R.N. and Johnson, D.L., 1981. The equivalence of quasistatic flow in fluid-saturated porous media and Biot's slow wave in the limit of zero frequency. Journal of Applied Physics, 52(5): 3391-3395.

Charlaix, E., Kushnick, A. and Stokes, J., 1988. Experimental study of dynamic permeability in porous media. Physical review letters, 61(14): 1595.

Cheng, F., Jinhua, F., Yujiang, S., Gaoren, L. and Zhiqiang, M., 2016. Predicting reservoir wettability via well logs. Journal of Geophysics and Engineering, 13(3): 234.

Cheng, J.-T. and Giordano, N., 2002. Fluid flow through nanometer-scale channels. Physical review E, 65(3): 031206.

Chow, T., 1998. Wetting of rough surfaces. Journal of Physics: Condensed Matter, 10(27): L445.

Cieplak, M., Koplik, J. and Banavar, J.R., 2001. Boundary conditions at a fluid-solid interface. Physical Review Letters, 86(5): 803.

Coates, G.R., Xiao, L. and Prammer, M.G., 1999. NMR logging: principles and applications, 234. Haliburton Energy Services Houston.

Cortis, A., Smeulders, D.M., Guermond, J.L. and Lafarge, D., 2003. Influence of pore roughness on high-frequency permeability. Physics of fluids, 15(6): 1766-1775.

Cottin-Bizonne, C., Barrat, J.-L., Bocquet, L. and Charlaix, E., 2003. Low-friction flows of liquid at nanopatterned interfaces. Nature materials, 2(4): 237.

Cottin-Bizonne, C., Cross, B., Steinberger, A. and Charlaix, E., 2005. Boundary slip on smooth hydrophobic surfaces: Intrinsic effects and possible artifacts. Physical review letters, 94(5): 056102.

Cottin-Bizonne, C. et al., 2002. Nanorheology: An investigation of the boundary condition at hydrophobic and hydrophilic interfaces. The European Physical Journal E, 9(1): 47-53.

Daniels, K.E. and Hayman, N.W., 2008. Force chains in seismogenic faults visualized with photoelastic granular shear experiments. Journal of Geophysical Research: Solid Earth, 113(B11).

Davis, R.H., Serayssol, J.-M. and Hinch, E., 1986. The elastohydrodynamic collision of two spheres. Journal of Fluid Mechanics, 163: 479-497.

de Gennes, P.-G., 2002. On fluid/wall slippage. Langmuir, 18(9): 3413-3414.

Dixit, A., Buckley, J., McDougall, S. and Sorbie, K., 1998. Core wettability: Should I AH Equal I USBM, International Symposium of the SCA, the Hague, the September.

Domenico, S., 1976. Effect of brine-gas mixture on velocity in an unconsolidated sand reservoir. Geophysics, 41(5): 882-894.

Donaldson, E.C., Thomas, R.D. and Lorenz, P.B., 1969. Wettability Determination and Its Effect on Recovery Efficiency.

Dullien, F.A., 2012. Porous media: fluid transport and pore structure. Academic press.

Dutta, N. and Odé, H., 1979. Attenuation and dispersion of compressional waves in fluid-filled porous rocks with partial gas saturation (White model)—Part II: Results. Geophysics, 44(11): 1789-1805.

Dutta, T., Mavko, G. and Mukerji, T., 2010. Improved granular medium model for unconsolidated sands using coordination number, porosity, and pressure relations. Geophysics, 75(2): E91-E99.

Dvorkin, J., Mavko, G. and Nur, A., 1991. The effect of cementation on the elastic properties of granular material. Mechanics of Materials, 12(3): 207-217.

Dvorkin, J. and Nur, A., 1993. Dynamic poroelasticity: A unified model with the squirt and the Biot mechanisms. Geophysics, 58(4): 524-533.

Dvorkin, J., Nur, A. and Yin, H., 1994. Effective properties of cemented granular materials. Mechanics of Materials, 18(4): 351-366.

Eslami, M., Kadkhodaie-Ilkhchi, A., Sharghi, Y. and Golsanami, N., 2013. Construction of synthetic capillary pressure curves from the joint use of NMR log data and conventional well logs. Journal of Petroleum Science and Engineering, 111: 50-58.

Feng, R., Zhang, Y., Rezagholilou, A., Roshan, H. and Sarmadivaleh, M., 2019. Brittleness Index: From Conventional to Hydraulic Fracturing Energy Model. Rock Mechanics and Rock Engineering: 1-15.

Furumura, T., Kennett, B. and Furumura, M., 1998. Seismic wavefield calculation for laterally heterogeneous whole earth models using the pseudospectral method. Geophysical Journal International, 135(3): 845-860.

Garrouch, A.A. and Alikhan, A.A., 1997. An Improved Method For Quantifying In-Situ Intermediate Wettability Using Well Logs. Society of Petrophysicists and Well-Log Analysts.

Garrouch, A.A. and Sharma, M.M., 1995. Dielectric properties of partially saturated rocks. Energy & fuels, 9(3): 413-419.

Gassmann, F., 1951. Elasticity of porous media. Vierteljahrsschrder Naturforschenden Gesselschaft, 96: 1-23.

Ghanbarian, B., Sahimi, M. and Daigle, H., 2016. Modeling relative permeability of water in soil: Application of effective-medium approximation and percolation theory. Water Resources Research, 52(7): 5025-5040.

Ghedan, S.G. and Canbaz, C.H., 2014. Theory and Experimental Setup of the New Rise In Core Reservoir Wettability Measurement Technique. International Petroleum Technology Conference.

Gist, G.A., 1994. Fluid effects on velocity and attenuation in sandstones. The Journal of the Acoustical Society of America, 96(2): 1158-1173.

Graham, J.W., 1958. Reverse-Wetting Logging. Society of Petroleum Engineers.

Granick, S., Zhu, Y. and Lee, H., 2003. Slippery questions about complex fluids flowing past solids. Nature materials, 2(4): 221.

Gregory, A., 1976. Fluid saturation effects on dynamic elastic properties of sedimentary rocks. Geophysics, 41(5): 895-921.

Griffiths, S., Rescaglio, A. and Melo, F., 2010. Ultrasound propagation in wet and airless non-consolidated granular materials. Ultrasonics, 50(2): 139-144.

Guan, H., Brougham, D., Sorbie, K.S. and Packer, K.J., 2002. Wettability effects in a sandstone reservoir and outcrop cores from NMR relaxation time distributions. Journal of Petroleum Science and Engineering, 34(1–4): 35-54.

Guo, J. and Han, X., 2016. Rock physics modelling of acoustic velocities for heavy oil sand. Journal of Petroleum Science and Engineering, 145: 436-443.

Gurevich, B., 2002. Effect of fluid viscosity on elastic wave attenuation in porous rocks. GEOPHYSICS, 67(1): 264-270.

Gurevich, B., Makarynska, D., de Paula, O.B. and Pervukhina, M., 2010. A simple model for squirt-flow dispersion and attenuation in fluid-saturated granular rocks. Geophysics, 75(6): N109-N120.

Güven, I., Luding, S. and Steeb, H., 2017. Incoherent Waves in Fluid-Saturated Sintered Granular Systems: Scattering Phenomena. Journal of Vibration and Acoustics, 140(1).

Han, T., Liu, B. and Sun, J., 2018. Validating the theoretical model for squirt-flow attenuation in fluid saturated porous rocks based on the dual porosity concept. Geophysical Journal International, 214(3): 1800-1807.

Hasanov, A.K., Dugan, B. and Batzle, M.L., 2020. Numerical Simulation of Oscillating Pore Pressure Experiments and Inversion for Permeability. Water Resources Research, 56(6): e2019WR025681.

Hasanov, A.K., Dugan, B., Batzle, M.L. and Prasad, M., 2019. Hydraulic and poroelastic rock properties from oscillating pore pressure experiments. Journal of Geophysical Research: Solid Earth, 124(5): 4473-4491.

Hill, R., 1963. Elastic properties of reinforced solids: some theoretical principles. Journal of the Mechanics and Physics of Solids, 11(5): 357-372.

Hosseini, S.A. and Tafreshi, H.V., 2010. Modeling permeability of 3-D nanofiber media in slip flow regime. Chemical Engineering Science, 65(6): 2249-2254.

Howard, J.J., 1998. Quantitative estimates of porous media wettability from proton NMR measurements. Magnetic Resonance Imaging, 16(5–6): 529-533.

Howell, D., Behringer, R. and Veje, C., 1999. Stress fluctuations in a 2D granular Couette experiment: a continuous transition. Physical Review Letters, 82(26): 5241.

Hu, H.S. and Wang, K.X., 2001. Dynamic Permeability in Porous Medium Acoustics. Chinese Journal of Geophysics, 44(1): 135-142.

Hu, R., Wan, J., Kim, Y. and Tokunaga, T.K., 2017. Wettability impact on supercritical CO2 capillary trapping: Pore‐scale visualization and quantification. Water Resources Research, 53(8): 6377-6394.

Huang, D.M., Sendner, C., Horinek, D., Netz, R.R. and Bocquet, L., 2008. Water slippage versus contact angle: A quasiuniversal relationship. Physical review letters, 101(22): 226101.

Huh, C., 2006. Improved oil recovery by seismic vibration: a preliminary assessment of possible mechanisms, International Oil Conference and Exhibition in Mexico. Society of Petroleum Engineers.

Ichimura, T., Hori, M. and Kuwamoto, H., 2007. Earthquake motion simulation with multiscale finite-element analysis on hybrid grid. Bulletin of the Seismological Society of America, 97(4): 1133-1143.

Javadpour, F., McClure, M. and Naraghi, M., 2015. Slip-corrected liquid permeability and its effect on hydraulic fracturing and fluid loss in shale. Fuel, 160: 549-559.

Jeong, C. and Kallivokas, L., 2017. An inverse-source problem for maximization of pore-fluid oscillation within poroelastic formations. Inverse Problems in Science and Engineering, 25(6): 832-863.

Jeong, C., Kallivokas, L.F., Kucukcoban, S., Deng, W. and Fathi, A., 2015. Maximization of wave motion within a hydrocarbon reservoir for wave-based enhanced oil recovery. Journal of Petroleum Science and Engineering, 129: 205-220.

Jia, X., Caroli, C. and Velicky, B., 1999. Ultrasound propagation in externally stressed granular media. Physical Review Letters, 82(9): 1863.

Job, S., Santibanez, F., Tapia, F. and Melo, F., 2008. Nonlinear waves in dry and wet Hertzian granular chains. Ultrasonics, 48(6-7): 506-514.

Johnson, D.L., 2001. Theory of frequency dependent acoustics in patchy-saturated porous media. The Journal of the Acoustical Society of America, 110(2): 682-694.

Johnson, D.L., Hemmick, D.L. and Kojima, H., 1994a. Probing porous media with first and second sound. I. Dynamic permeability. Journal of Applied Physics, 76(1): 104-114.

Johnson, D.L., Koplik, J. and Dashen, R., 1987. Theory of dynamic permeability and tortuosity in fluid-saturated porous media. Journal of fluid mechanics, 176: 379-402.

Johnson, D.L., Plona, T.J. and Kojima, H., 1994b. Probing porous media with first and second sound. II. Acoustic properties of water‐saturated porous media. Journal of Applied Physics, 76(1): 115-125.

Johnson, P.A. and Jia, X., 2005. Nonlinear dynamics, granular media and dynamic earthquake triggering. Nature, 437(7060): 871-874.

Johnston, D.H., Toksöz, M. and Timur, A., 1979. Attenuation of seismic waves in dry and saturated rocks: II. Mechanisms. Geophysics, 44(4): 691-711.

Jones, T.D., 1986. Pore fluids and frequency-dependent wave propagation in rocks. Geophysics, 51(10): 1939-1953.

Joseph, P. and Tabeling, P., 2005. Direct measurement of the apparent slip length. Physical Review E, 71(3): 035303.

Kelder, O. and Smeulders, D.M., 1997. Observation of the Biot slow wave in water-saturated Nivelsteiner sandstone. Geophysics, 62(6): 1794-1796.

Khishvand, M., Alizadeh, A., Kohshour, I.O., Piri, M. and Prasad, R., 2017. In situ characterization of wettability alteration and displacement mechanisms governing recovery enhancement due to low‐salinity waterflooding. Water Resources Research, 53(5): 4427-4443.

Komatitsch, D. and Tromp, J., 1999. Introduction to the spectral element method for three-dimensional seismic wave propagation. Geophysical journal international, 139(3): 806-822.

Kouznetsov, O., Simkin, E., Chilingar, G. and Katz, S., 1998. Improved oil recovery by application of vibro-energy to waterflooded sandstones. Journal of Petroleum Science and Engineering, 19(3-4): 191-200.

Ladd, C.R. and Reber, J.E., 2020. The Effect of a Liquid Phase on Force Distribution During Deformation in a Granular System. Journal of Geophysical Research: Solid Earth, 125(8): e2020JB019771.

Landau, L.D. and Lifshitz, E.M., 1987. Fluid mechanics.

Langlois, V. and Jia, X., 2014. Acoustic probing of elastic behavior and damage in weakly cemented granular media. Physical Review E, 89(2): 023206.

Lauga, E., Brenner, M. and Stone, H., 2007. Microfluidics: the no-slip boundary condition. Springer handbook of experimental fluid mechanics: 1219-1240.

Lauga, E. and Stone, H.A., 2003. Effective slip in pressure-driven Stokes flow. Journal of Fluid Mechanics, 489: 55-77.

Lebedev, M. and Lopes, S.A.C., 2013. Fluid injection in reservoir rocks with X-ray CT scanning and active ultrasonic monitoring.

Lebedev, M. et al., 2009. Direct laboratory observation of patchy saturation and its effects on ultrasonic velocities. The Leading Edge, 28(1): 24-27.

Leger, L., 2002. Friction mechanisms and interfacial slip at fluid–solid interfaces. Journal of Physics: Condensed Matter, 15(1): S19.

Li, J.X., Rezaee, R. and Müller, T.M., 2020a. Wettability effect on wave propagation in saturated porous medium. The Journal of the Acoustical Society of America, 147(2): 911-920.

Li, J.X., Rezaee, R., Müller, T.M. and Sarmadivaleh, M., 2020b. Elastic waves in porous media saturated with non-wetting fluid. The APPEA Journal, 60(1): 315-325.

Li, J.X., Rezaee, R., Müller, T.M. and Sarmadivaleh, M., 2020c. Pore Size Distribution Controls Dynamic Permeability. Geophysical Research Letters: e2020GL090558.

Li, X., Zhong, L. and Pyrak-Nolte, L.J., 2001. Physics of partially saturated porous media: Residual saturation and seismic-wave propagation. Annual Review of Earth and Planetary Sciences, 29(1): 419-460.

Lighthill, M.J. and Lighthill, J., 2001. Waves in fluids. Cambridge university press.

Lin, L., 2011. In-situ measurement of permeability of a porous interface using the ultrasonic slow wave. The Journal of the Acoustical Society of America, 125.

Lin, Y.B., Tan, Y.C., Yeh, T.C.J., Liu, C.W. and Chen, C.H., 2004. A viscoelastic model for groundwater level changes in the Cho-Shui River alluvial fan after the Chi-Chi earthquake in Taiwan. Water resources research, 40(4).

Liu, C.-h. and Nagel, S.R., 1992. Sound in sand. Physical review letters, 68(15): 2301.

Liu, H.-H., 2014. Non-Darcian flow in low-permeability media: key issues related to geological disposal of high-level nuclear waste in shale formations. Hydrogeology journal, 22(7): 1525-1534.

Liu, J., Müller, T.M., Qi, Q., Lebedev, M. and Sun, W., 2016. Velocity-saturation relation in partially saturated rocks: Modelling the effect of injection rate changes. Geophysical Prospecting, 64(4): 1054-1066.

Liu, X., Cai, X., Guo, Q. and Yang, J., 2018. Study of acoustic wave propagation in micro- and nanochannels. Wave Motion, 76: 51-60.

Lo, W.C., Sposito, G. and Majer, E., 2005. Wave propagation through elastic porous media containing two immiscible fluids. Water Resources Research, 41(2).

Lo, W.C. et al., 2017. The dynamic response of the water retention curve in unsaturated soils during drainage to acoustic excitations. Water Resources Research, 53(1): 712-725.

Looyestijn, W.J. and Hofman, J., 2006. Wettability-Index Determination by Nuclear Magnetic Resonance.

Lopes, S., Lebedev, M., Müller, T.M., Clennell, M.B. and Gurevich, B., 2014. Forced imbibition into a limestone: Measuring P-wave velocity and water saturation dependence on injection rate. Geophysical Prospecting, 62(5): 1126-1142.

Lu, Y. et al., 2019. Analytical modelling of wettability alteration-induced micro-fractures during hydraulic fracturing in tight oil reservoirs. Fuel, 249: 434-440.

Makse, H.A., Gland, N., Johnson, D.L. and Schwartz, L., 2004. Granular packings: Nonlinear elasticity, sound propagation, and collective relaxation dynamics. Physical Review E, 70(6): 061302.

Markov, M., 2007. Effect of interfacial slip on the kinematic and dynamic parameters of elastic waves in a fluid-saturated porous medium. Acoustical Physics, 53(2): 213-216.

Markov, M. and Markov, A., 2018. Propagation of Elastic Waves in a Gas-Filled Poroelastic Medium: The Influence of the Boundary Conditions. Transport in Porous Media: 1-12.

Mavko, G. and Jizba, D., 1991. Estimating grain-scale fluid effects on velocity dispersion in rocks. Geophysics, 56(12): 1940-1949.

Mavko, G. and Jizba, D., 1994. The relation between seismic P-and S-wave velocity dispersion in saturated rocks. Geophysics, 59(1): 87-92.

Mavko, G. and Mukerji, T., 1998. Bounds on low-frequency seismic velocities in partially saturated rocks. Geophysics, 63(3): 918-924.

Mavko, G., Mukerji, T. and Dvorkin, J., 2009. The rock physics handbook: Tools for seismic analysis of porous media. Cambridge university press.

Mavko, G. and Nolen-Hoeksema, R., 1994. Estimating seismic velocities at ultrasonic frequencies in partially saturated rocks. Geophysics, 59(2): 252-258.

Mavko, G. and Nur, A., 1975. Melt squirt in the asthenosphere. Journal of Geophysical Research, 80(11): 1444-1448.

Mavko, G.M. and Nur, A., 1979. Wave attenuation in partially saturated rocks. Geophysics, 44(2): 161-178.

Melosh, H., 1996. Dynamical weakening of faults by acoustic fluidization. Nature, 379(6566): 601-606.

Moebius, F., Canone, D. and Or, D., 2012. Characteristics of acoustic emissions induced by fluid front displacement in porous media. Water Resources Research, 48(11).

Moerig, R., Waite, W., Boyd, O., Getting, I. and Spetzler, H., 1996. Seismic attenuation in artificial glass cracks: Physical and physicochemical effects of fluids. Geophysical research letters, 23(16): 2053-2056.

Molz, F.J., Morin, R.H., Hess, A.E., Melville, J.G. and Güven, O., 1989. The impeller meter for measuring aquifer permeability variations: evaluation and comparison with other tests. Water Resources Research, 25(7): 1677-1683.

Mukerji, T., Mavko, G., Mujica, D. and Lucet, N., 1995. Scale-dependent seismic velocity in heterogeneous media. GEOPHYSICS, 60(4): 1222-1233.

Müller, T. and Sahay, P., 2011a. Porous medium acoustics of wave-induced vorticity diffusion. Applied Physics Letters, 98(8): 084101.

Müller, T.M. and Gurevich, B., 2004. One-dimensional random patchy saturation model for velocity and attenuation in porous rocksRadom Patchy Saturation Model. Geophysics, 69(5): 1166-1172.

Müller, T.M. and Gurevich, B., 2005. Wave-induced fluid flow in random porous media: Attenuation and dispersion of elastic waves. The Journal of the Acoustical Society of America, 117(5): 2732-2741.

Müller, T.M., Gurevich, B. and Lebedev, M., 2010. Seismic wave attenuation and dispersion resulting from wave-induced flow in porous rocks—A review. Geophysics, 75(5): 75A147-75A164.

Müller, T.M. and Sahay, P.N., 2010. Acoustic signatures of wave-induced vorticity diffusion in porous media, SEG Technical Program Expanded Abstracts 2010. Society of Exploration Geophysicists, pp. 2622-2627.

Müller, T.M. and Sahay, P.N., 2011b. Fast compressional wave attenuation and dispersion due to conversion scattering into slow shear waves in randomly heterogeneous porous media. The Journal of the Acoustical Society of America, 129(5): 2785-2796.

Müller, T.M. and Sahay, P.N., 2011c. Stochastic theory of dynamic permeability in poroelastic media. Physical Review E, 84(2): 026329.

Murphy III, W.F., 1984. Acoustic measures of partial gas saturation in tight sandstones. Journal of Geophysical Research: Solid Earth, 89(B13): 11549-11559.

Murphy III, W.F., Winkler, K.W. and Kleinberg, R.L., 1984. Frame modulus reduction in sedimentary rocks: The effect of adsorption on grain contacts. Geophysical Research Letters, 11(9): 805-808.

Murphy III, W.F., Winkler, K.W. and Kleinberg, R.L., 1986. Acoustic relaxation in sedimentary rocks: Dependence on grain contacts and fluid saturation. Geophysics, 51(3): 757-766.

Nagy, P.B. and Blaho, G., 1994. Experimental measurements of surface stiffness on water-saturated porous solids. The Journal of the Acoustical Society of America, 95(2): 828-835.

Navier, C., 1823. Mémoire sur les lois du mouvement des fluides. Mémoires de l'Académie Royale des Sciences de l'Institut de France, 6(1823): 389-440.

Neto, C., Evans, D.R., Bonaccurso, E., Butt, H.-J. and Craig, V.S., 2005. Boundary slip in Newtonian liquids: a review of experimental studies. Reports on progress in physics, 68(12): 2859.

Neuzil, C.E., 1986. Groundwater flow in low-permeability environments. Water Resources Research, 22(8): 1163-1195.

Nie, J.-X. et al., 2012. BISQ model based on a Kelvin-Voigt viscoelastic frame in a partially saturated porous medium. Applied Geophysics, 9(2): 213-222.

Nie, J., Yang, D. and Yang, H., 2008. A generalized viscoelastic Biot/squirt model for clay-bearing sandstones in a wide range of permeabilities. Applied Geophysics, 5(4): 249.

Nolet, G., 2012. Seismic tomography: with applications in global seismology and exploration geophysics, 5. Springer Science & Business Media.

O'Connell, R.J. and Budiansky, B., 1974. Seismic velocities in dry and saturated cracked solids. Journal of geophysical Research, 79(35): 5412-5426.

O'Connell, R.J. and Budiansky, B., 1977. Viscoelastic properties of fluid-saturated cracked solids. Journal of Geophysical Research, 82(36): 5719-5735.

Ortiz-Young, D., Chiu, H.-C., Kim, S., Voïtchovsky, K. and Riedo, E., 2013. The interplay between apparent viscosity and wettability in nanoconfined water. Nature communications, 4: 2482.

Owens, E.T. and Daniels, K.E., 2011. Sound propagation and force chains in granular materials. EPL (Europhysics Letters), 94(5): 54005.

Owens, W.W. and Archer, D.L., 1971. The Effect of Rock Wettability on Oil-Water Relative Permeability Relationships.

Pazdniakou, A. and Adler, P., 2013. Dynamic permeability of porous media by the lattice Boltzmann method. Advances in water resources, 62: 292-302.

Pirson, S.J. and Fraser, C.D., 1960. Quantitative Interpretation of Electric Logs in Oil-Wet Rocks Proposed Procedure and Example Applications. Society of Petroleum Engineers.

Pit, R., Hervet, H. and Leger, L., 2000. Direct experimental evidence of slip in hexadecane: solid interfaces. Physical review letters, 85(5): 980.

Plona, T.J., 1980. Observation of a second bulk compressional wave in a porous medium at ultrasonic frequencies. Applied physics letters, 36(4): 259-261.

Poletto, F. and Miranda, F., 2004. Seismic while drilling: Fundamentals of drill-bit seismic for exploration, 35. Elsevier.

Pride, S.R., Berryman, J.G. and Harris, J.M., 2004. Seismic attenuation due to wave-induced flow. Journal of Geophysical Research: Solid Earth, 109(B1).

Pride, S.R., Morgan, F.D. and Gangi, A.F., 1993. Drag forces of porous-medium acoustics. Physical review B, 47(9): 4964.

Priezjev, N.V., Darhuber, A.A. and Troian, S.M., 2005. Slip behavior in liquid films on surfaces of patterned wettability: Comparison between continuum and molecular dynamics simulations. Physical Review E, 71(4): 041608.

Qi, Q., 2015. Effect of capillarity on the acoustics of partially saturated porous rocks, Curtin University.

Qi, Q. et al., 2014. Quantifying the effect of capillarity on attenuation and dispersion in patchy-saturated rocksCapillarity in patchy-saturated rocks. Geophysics, 79(5): WB35-WB50.

Ramakrishnan, T.S. and Cappiello, A., 1991. A new technique to measure static and dynamic properties of a partially saturated porous medium. Chemical Engineering Science, 46(4): 1157-1163.

Ramos-Alvarado, B., Kumar, S. and Peterson, G., 2016. Hydrodynamic slip length as a surface property. Physical Review E, 93(2): 023101.

Raza, S., Treiber, L. and Archer, D., 1968. Wettability of reservoir rocks and its evaluation. Prod. Mon.;(United States), 32(4).

Reynes, J., Woignier, T. and Phalippou, J., 2001. Permeability measurement in composite aerogels: application to nuclear waste storage. Journal of non-crystalline solids, 285(1-3): 323-327.

Rolo, L.I., Caco, A.I., Queimada, A.J., Marrucho, I.M. and Coutinho, J.A., 2002. Surface tension of heptane, decane, hexadecane, eicosane, and some of their binary mixtures. Journal of Chemical & Engineering Data, 47(6): 1442-1445.

Romanowicz, B., 2017. Geophysics: The buoyancy of Earth's deep mantle. Nature, 551(7680): 308.

Ruiz, F. and Azizov, I., 2011. Tight shale elastic properties using the soft-porosity and single aspect ratio models, SEG Technical Program Expanded Abstracts 2011. Society of Exploration Geophysicists, pp. 2241-2245.

Sahay, P.N., 2008. On the Biot slow S-wave. Geophysics, 73(4): N19-N33.

Sahay, P.N., Spanos, T.T. and De La Cruz, V., 2001. Seismic wave propagation in inhomogeneous and anisotropic porous media. Geophysical Journal International, 145(1): 209-222.

Santos, J.E., Douglas Jr, J., Corberó, J. and Lovera, O.M., 1990. A model for wave propagation in a porous medium saturated by a two-phase fluid. The Journal of the Acoustical Society of America, 87(4): 1439-1448.

Sayers, C. and Dahlin, A., 1993. Propagation of ultrasound through hydrating cement pastes at early times. Advanced Cement Based Materials, 1(1): 12-21.

Sayers, C.M., 2021. Mechanical properties of grain contacts in unconsolidated sands. Geophysics, 86(2): MR95-MR103.

Scott, D.R., 1996. Seismicity and stress rotation in a granular model of the brittle crust. Nature, 381(6583): 592-595.

Shakouri, A., Farzay, O., Masihi, M., Ghazanfari, M.H. and Al-Ajmi, A.M., 2019. An experimental investigation of dynamic elastic moduli and acoustic velocities in heterogeneous carbonate oil reservoirs. SN Applied Sciences, 1(9): 1023.

Sharma, M.M. and Wunderlich, R.W., 1987. The alteration of rock properties due to interactions with drilling-fluid components. Journal of Petroleum Science and Engineering, 1(2): 127-143.

Sheng, P. and Zhou, M.-Y., 1988. Dynamic permeability in porous media. Physical review letters, 61(14): 1591.

Smeulders, D., Eggels, R. and Van Dongen, M., 1992. Dynamic permeability: reformulation of theory and new experimental and numerical data. Journal of Fluid Mechanics, 245: 211-227.

Smith, T.M., Sondergeld, C.H. and Rai, C.S., 2003. Gassmann fluid substitutions: A tutorial. Geophysics, 68(2): 430-440.

Spikes, H. and Granick, S., 2003. Equation for slip of simple liquids at smooth solid surfaces. Langmuir, 19(12): 5065-5071.

Spinler, E., 1996. Methodology For Determining The Distribution Or Wettability From Laboratory And Well Log Measurements For A Micro-crystalline/Micro-fossiliferous Carbonate Field.

Spinler, E., 1997. Determination of In-Situ Wettability from Laboratory and Well Log Measurements for a Carbonate Field. Society of Petroleum Engineers.

Stoll, R.D., 1977. Acoustic waves in ocean sediments. Geophysics, 42(4): 715-725.

Sun, W., Ba, J., Müller, T.M., Carcione, J.M. and Cao, H., 2015. Comparison of P-wave attenuation models of wave-induced flow. Geophysical Prospecting, 63(2): 378-390.

Sun, W., Xiong, F., Ba, J. and Carcione, J.M., 2018. Effects of ellipsoidal heterogeneities on wave propagation in partially-saturated double-porosity rocks. Geophysics, 83(3): 1-39.

Thompson, P.A. and Robbins, M.O., 1990. Shear flow near solids: Epitaxial order and flow boundary conditions. Physical review A, 41(12): 6830.

Thompson, P.A. and Troian, S.M., 1997. A general boundary condition for liquid flow at solid surfaces. Nature, 389(6649): 360.

Toms, J., Müller, T.M., Ciz, R. and Gurevich, B., 2006. Comparative review of theoretical models for elastic wave attenuation and dispersion in partially saturated rocks. Soil Dynamics and Earthquake Engineering, 26(6): 548-565.

Toms, J., Müller, T.M. and Gurevich, B., 2007. Seismic attenuation in porous rocks with random patchy saturation. Geophysical Prospecting, 55(5): 671-678.

Tserkovnyak, Y. and Johnson, D.L., 2003. Capillary forces in the acoustics of patchy-saturated porous media. The Journal of the Acoustical Society of America, 114(5): 2596-2606.

Tsiklauri, D., 2002. Phenomenological model of propagation of the elastic waves in a fluid-saturated porous solid with nonzero boundary slip velocity. The Journal of the Acoustical Society of America, 112(3): 843-849.

Umnova, O., Tsiklauri, D. and Venegas, R., 2009. Effect of boundary slip on the acoustical properties of microfibrous materials. The Journal of the Acoustical Society of America, 126(4): 1850-1861.

Vinogradova, O.I., 1995. Drainage of a thin liquid film confined between hydrophobic surfaces. Langmuir, 11(6): 2213-2220.

Vinogradova, O.I., 1998. Implications of hydrophobic slippage for the dynamic measurements of hydrophobic forces. Langmuir, 14(10): 2827-2837.

Vinogradova, O.I. and Belyaev, A.V., 2011. Wetting, roughness and flow boundary conditions. Journal of Physics: Condensed Matter, 23(18): 184104.

Vinogradova, O.I. and Yakubov, G.E., 2003. Dynamic effects on force measurements. 2. Lubrication and the atomic force microscope. Langmuir, 19(4): 1227-1234.

Wang, S.-J. and Hsu, K.-C., 2009. The application of the first-order second-moment method to analyze poroelastic problems in heterogeneous porous media. Journal of Hydrology, 369(1-2): 209-221.

Wang, Z. and Nur, A.M., 1988. Velocity dispersion and the “local flow” mechanism in rocks, SEG Technical Program Expanded Abstracts 1988. Society of Exploration Geophysicists, pp. 548-550.

Wang, Z., Schmitt, D.R. and Wang, R., 2015. Does wettability influence seismic wave propagation in liquid-saturated porous rocks? Geophysical Journal International, 203(3): 2182-2188.

Wenzlau, F. and Müller, T.M., 2009. Finite-difference modeling of wave propagation and diffusion in poroelastic media. Geophysics, 74(4): T55-T66.

White, J., 1975. Computed seismic speeds and attenuation in rocks with partial gas saturation. Geophysics, 40(2): 224-232.

Widiatmoko, E., Abdullah, M. and Khairurrijal, 2010. A Method to Measure Pore Size Distribution of Porous Materials Using Scanning Electron Microscopy Images, Aip conference proceedings. American Institute of Physics, pp. 23-26.

Winkler, K.W., 1985. Dispersion analysis of velocity and attenuation in Berea sandstone. Journal of Geophysical Research: Solid Earth, 90(B8): 6793-6800.

Winkler, K.W., 1986. Estimates of velocity dispersion between seismic and ultrasonic frequencies. Geophysics, 51(1): 183-189.

Wulff, A.M. and Burkhardt, H., 1997. Mechanisms affecting ultrasonic wave propagation in fluid‐containing sandstones under high hydrostatic pressure. Journal of Geophysical Research: Solid Earth, 102(B2): 3043-3050.

Wyllie, M.R.J., Gregory, A.R. and Gardner, L.W., 1956. Elastic wave velocities in heterogeneous and porous media. Geophysics, 21(1): 41-70.

Xiao, L., Mao, Z.-q., Zou, C.-c., Jin, Y. and Zhu, J.-c., 2016. A new methodology of constructing pseudo capillary pressure (Pc) curves from nuclear magnetic resonance (NMR) logs. Journal of Petroleum Science and Engineering, 147: 154-167.

Xu, P. and Yu, B., 2008. Developing a new form of permeability and Kozeny–Carman constant for homogeneous porous media by means of fractal geometry. Advances in water resources, 31(1): 74-81.

Xue, J. et al., 2018. Chitosan‐functionalized graphene oxide for enhanced permeability and antifouling of ultrafiltration membranes. Chemical Engineering & Technology, 41(2): 270-277.

Zhang, X. and Müller, T.M., 2019. Stoneley wave attenuation and dispersion and the dynamic permeability correction. Geophysics, 84(3): 1-47.

Zhou, M.-Y. and Sheng, P., 1989. First-principles calculations of dynamic permeability in porous media. Physical Review B, 39(16): 12027.

Zinszner, B. and Pellerin, F.-M., 2007. A geoscientist's guide to petrophysics. Editions Technip.

Zuo, L., Humbert, M. and Esling, C., 1992. Elastic properties of polycrystals in the Voigt-Reuss-Hill approximation. Journal of applied crystallography, 25(6): 751-755.